Czech Technical University in Prague
Faculty of Nuclear Sciences and Physical Engineering
Department of Physical Electronics

# Nonlinear laser absorption under high-energy-density conditions

Doctoral thesis

*Sviatoslav Shekhanov*

Ph.D. programme: Applications of Natural Sciences
Branch of study: Physical Engineering
Supervisors: prof. Ing. Jiří Limpouch, prof. Vladimir Tikhonchuk

Prague, March 2023

**Bibliographic entry**

---

| | |
|---|---|
| *Title:* | **Nonlinear laser absorption under high-energy-density conditions** |
| *Author:* | Sviatoslav Shekhanov<br>Czech Technical University in Prague (CTU),<br>Faculty of Nuclear Sciences and Physical Engineering,<br>Department of Physical Electronics<br>Extreme Light Infrastructure ERIC |
| *Degree programme:* | Applications of Natural Sciences |
| *Field of study:* | Physical Engineering |
| *Supervisors:* | prof. Ing. Jiří Limpouch, CSc., CTU<br>prof. Vladimir Tikhonchuk, CELIA |
| *Number of pages:* | 141 |
| *Key words:* | Non-linear absorption, parametric instabilities, stimulated Raman scattering, stimulated Brillouin scattering, low-density porous targets, inertial confinement fusion |

**Bibliografický záznam**

---

| | |
|---|---|
| *Název práce:* | **Nelineární absorpce laserového záření za podmínek vysoké hustoty energie** |
| *Autor:* | Sviatoslav Shekhanov<br>České vysoké učení technické v Praze (ČVUT),<br>Fakulta jaderná a fyzikálně inženýrská,<br>Katedra fyzikální elektroniky<br>Extreme Light Infrastructure ERIC |
| *Studijní program:* | Aplikace přírodních věd |
| *Studijní obor:* | Fyzikální inženýrství |
| *Školitelé:* | prof. Ing. Jiří Limpouch, CSc., CTU<br>prof. Vladimir Tikhonchuk, CELIA |
| *Počet stran:* | 141 |
| *Klíčová slova:* | Nelineární absorpce, parametrické nestability, stimulovaný Ramanův rozptyl, stimulovaný Brillouinův rozptyl, porézní terče s nízkou hustotou, inerciální fúze |

**Declaration**

---

I declare that I wrote this thesis independently with the use of cited bibliography.

Prague, 15 March 2023

# Abstract

This thesis presents theoretical and numerical studies of high intensity laser interaction with plasmas in the context of shock ignition approach to inertial confinement fusion for energy production. Two key subjects are considered: i) the control of nonlinear laser absorption in plasma, mitigating laser backscattering due to the competition between stimulated Brillouin (SBS) and Raman (SRS) scattering, and ii) the interaction of laser radiation with low-density porous materials and their transformation into a hot homogeneous plasma.

The studies of nonlinear laser-plasma interaction demonstrate the necessity of mitigating SBS to achieve efficient laser absorption under shock ignition conditions. Several methods of SBS suppression are evaluated, including the use of multiple ion species, plasma expansion, and laser bandwidth. Theoretical analysis of trapped modes in plasma cavities is confirmed in numerical simulations, showing efficient absorption of laser energy exceeding 30% and ion acceleration in the expanding cavities. Theoretical and numerical analysis of laser interaction with porous materials sheds new light on the physics of high-intensity laser interaction with structured low-density materials and provides valuable input for constructing a sub-grid model describing foam heating and homogenization.

The results obtained in this work open further perspectives in laser-plasma interaction studies in application to the shock ignition and to the laser-driven inertial fusion in general. The investigation of SBS mitigation methods in two-dimensional geometry is essential for developing a comprehensive understanding of the laser-plasma interaction dynamics. Further investigation of foam targets is necessary to fully understand the nonlinear interaction between high-intensity lasers and structured materials.

# Abstrakt

Tato disertace prezentuje teoretické a numerické studie interakce vysoce intenzivního laserového záření s plazmatem v kontextu inerciální fúze pro výrobu energie zapálené rázovou vlnou. Jsou zde studována dvě klíčová témata: i) nastavení úrovně nelineární absorpce laserového záření v plazmatu a omezení zpětného rozptylu laserového záření v důsledku vzájemné interakce stimulovaného Brillouinova (SBS) a Ramanova (SRS) rozptylu a ii) interakce laserového záření s porézními materiály o nízké střední hustotě a jejich transformace v horké homogenní plazma.

Studie nelineární interakce laserového záření ukazují na nutnost omezení SBS k dosažení účinné absorpce laserového záření za podmínek odpovídajících zapálení inerciální fúze rázovou vlnou. Je posuzováno několik metod potlačení SBS včetně využití více druhů iontů, expanze plazmatu a širokospektrálního laserového záření. Teoretická analýza módů zachycených v plazmových kavitách, potvrzená v numerických simulacích, ukazuje účinnou absorpci laserového záření přesahující 30% a na urychlování iontů v expandujících kavitách. Teoretická a numerická analýza interakce laserového záření s porézními materiály přináší nový pohled na fyziku interakce se strukturovanými materiály o nízké hustotě a poskytuje cenné informace pro konstrukci modelu se zanořenou detailní podsítí popisujícího ohřev a homogenizaci pěny.

Výsledky získané v této práci otvírají další perspektivy pro studie interakce laserového záření s plazmatem zaměřené na rázové zapálení inerciální fúze a na laserovou inerciální fúzi obecně. Výzkum metod pro omezení SBS v dvourozměrné geometrii je zásadní pro úplné porozumění dynamiky interakce laserového záření s plazmatem. Další studium pěnových terčů je nezbytně pro porozumění nelineární interakce vysoce intenzivního laserového záření se strukturovanými materiály.

# Acknowledgements

I would like to take this opportunity to express my heartfelt appreciation to the individuals who have helped and supported me throughout my research journey. Their guidance, encouragement, and unwavering support have been instrumental in the successful completion of this thesis. I am deeply grateful for their contributions and would like to acknowledge their efforts through this section. I also apologize to anyone who may have been inadvertently left out of this list, as their contributions were no less important or appreciated.

I would also like to extend a special thank you to my family, who have always been there for me and provided me with their unwavering love and support.

I am deeply grateful to my supervisor, Vladimir Tikhonchuk, for his patience, guidance, and mentorship throughout my research project. His expertise and knowledge have been invaluable, and I have learned so much from him. I am also thankful for the opportunity to live and work in Bordeaux and Prague under his supervision. His support and encouragement have been instrumental in my personal and professional growth, and I am grateful for his commitment to my success.

Next, I would like to express my gratitude to all the supervisors and bosses who were involved in my PhD project, including Stefan Weber for his leadership in our group, Jiří Limpouch for providing guidance on scientific and administrative matters at CTU, and Sergei Bulanov for offering me the opportunity to study ultra-high intense laser research.

I would like to express my gratitude to ELI-Beamlines and the Faculty of Nuclear Sciences and Physical Engineering at the Czech Technical University in Prague, along with their representatives, for generously accommodating me during my PhD project.

I would like to express my gratitude to my colleagues from ELI-Beamlines, specifically Jan Nikl, Petr Valenta, Martin Matys, Ondřej Klimo and Martin Jirka, for their invaluable assistance with PIC simulations and support during the initial stages of my PhD project.

Finally, I would like to thank Nora for being chaotically good and somehow stimulating my research interests.

# Contents

# Chapter 0

# Introduction

This thesis focuses on the theoretical and numerical examination of laser-target interaction in relation to inertial confinement fusion. The research concentrates on two crucial areas of study. The first aspect involves investigating the occurrence of parametric instabilities in the long corona during laser-plasma interactions. Additionally, this thesis explores the effects of hot electrons on ICF system performance, which are also phenomena that occur during laser-plasma interactions. The second area of study pertains to the use of low-density foams as outer layers of ICF targets. These foams have demonstrated advantageous properties, including their ability to smooth laser beams and serve as efficient sources of x-rays, energetic electrons, and ions. However, the understanding of the interaction between intense laser radiation and structured materials, like foams, is not complete. This research aims to address some of the unresolved problems and challenges that require further exploration.

## 0.1 General context

With the advent of a new generation of powerful lasers, the research in high-energy density physics has attracted a widespread interest. One of the applications that has made a strong contribution to the development of high-energy density physics is inertial confinement fusion (ICF).

ICF is a promising approach for achieving controlled thermonuclear fusion with the potential to provide a virtually limitless source of clean and abundant energy. In ICF, a small pellet of fuel is compressed and heated to extremely high temperatures and pressures, leading to the fusion of atomic nuclei and the release of energy.

The fusion process occurs when the nuclei of two light atoms, such as hydrogen, come close enough together that the strong nuclear force can overcome the Coulomb repulsion, which is the force that pushes the nuclei apart due to their positive charge. This requires

the fuel to be heated to extremely high temperatures (tens of millions of degrees) and compressed to extremely high densities (millions of times denser than solid matter).

Controlling thermonuclear fusion requires meeting a specific condition to sustain a fusion reaction. This is known as the Lawson criterion [1], which states that the fusion rate must be higher than the energy loss rate in order for a fusion reaction to be sustained. Meeting this criterion requires the fuel to be confined for a sufficient amount of time at the necessary temperature and density.

The ICF power plant will operate in the pulsation mode [2], which can be assimilated to ordinary combustion engines. The ICF reactor operation consists of periodic cycles that proceed in four major steps:

i) Preparation: in this step, the fusion fuel is carefully prepared and loaded into a small, spherical capsule, which can be placed inside a cylindrical case "hohlraum" made of a high-density material, such as gold, lead or uranium. The hohlraum with a capsule or the capsule alone are then placed inside the ICF reactor.

ii) Compression: in this step, the capsule or the hohlraum containing the capsule is irradiated by the laser beams or ion beams, which vaporize the outer layer of the capsule and compress the fuel by ablation pressure. This process can be achieved through either direct drive, where the laser beams or ion beams directly irradiate the capsule, or indirect drive, where the beams first strike the hohlraum, producing X-rays that then drive the implosion of the capsule. The fuel is imploded, compressed, and heated to the conditions found in the core of a star, where hydrogen atoms fuse together to form helium.

iii) Ignition: in this step, the compressed fuel reaches a critical temperature and density needed to excite a self-sustaining chain of fusion reactions. This produces a large amount of energy, which is released in the form of high-energy charged particles, neutrons and radiation.

iv) Heat extraction: in this step, the energy released in the fusion reactions is transformed into a heat in the walls of the reactor chamber. This heat is directed out of the ICF reactor to generate electricity or power other applications.

One of the key challenges in ICF is the need to generate and maintain extremely high temperatures and densities in the fuel, in order to achieve the conditions necessary for fusion reactions to occur. This requires precise control of the energy delivery to the capsule, as well as a thorough understanding of the complex physical processes involved in the capsule implosion and heating.

The laser intensity needed for the capsule implosion is so high that the target material is transformed in a high temperature, dense plasma. Laser energy absorption in such a plasma is a strongly nonlinear process, which involves collisional dissipation and

excitation of secondary plasma waves through the parametric instabilities. Such nonlinear processes as Stimulated Raman Scattering (SRS) and Stimulated Brillouin Scattering (SBS) are primary instabilities that can significantly affect the performance of ICF capsule. These instabilities occur in the outer part of capsule where the laser light interacts with the plasma outflow. They can lead to reflection of a significant part of laser energy, thus reducing the energy available for the implosion. Additionally, SRS and Two Plasmon Decay (TPD) instability [3]–[5] lead to the generation of copious energetic electrons that penetrate in a central part of the target, preheat it and reduce the fuel compression. Moreover, laser filamentation instability (FI) [6]–[8] and cross beam energy transfer (CBET) [9]–[11] may induce inhomogeneities in the laser energy deposition at the target surface and destroy the symmetry of capsule implosion.

SRS is a nonlinear scattering process that occurs when laser light interacts with a plasma and transfers energy to plasma Langmuir waves [12]. This process can lead to reflection of a significant fraction of the incident laser energy in plasma, thus reducing the energy available for the target implosion and heating. SBS is a nonlinear scattering process that occurs when laser light interacts with the plasma and transfers energy to plasma ion acoustic waves [12]. Like SRS, SBS can lead to the reflection of a significant fraction of the laser energy from the plasma.

TPD, CBET and FI are nonlinear laser-plasma interaction processes that can occur in the context of ICF. TPD is a decay of a high-frequency electromagnetic laser wave into two lower-frequency Langmuir waves, while the filamentation instability is characterized by the formation of filamentary structures in the distribution of laser radiation in plasma. Both TPD and SRS can lead to a conversion of a significant fraction of laser energy into hot electrons. CBET and FI lead to the formation of nonuniformities in the distribution of laser radiation in plasma, which can negatively affect the symmetry of ablation pressure and target implosion, and thus reduce the fusion yield. Therefore, understanding and mitigating the negative effects associated with these instabilities is critical for the successful implementation of ICF.

Improved characterization of laser plasma interaction processes is accomplished through the use of advanced diagnostic techniques, such as Thomson scattering and interferometry, which can provide insight into the physical processes involved in these instabilities. It can also be achieved through the development of advanced simulation tools, such as particle-in-cell (PIC) codes, which can help to predict the evolution of these instabilities under different conditions.

Recent investigations in the domain of laser plasma interaction have been focused on improving the performance of ICF experiments through the improvement of the quality of laser beams and mitigation of nonlinear processes. However, the extreme conditions

required for laser-driven fusion present significant challenges, such as the need to achieve a high laser absorption efficiency, control the generation of hot electrons and the symmetry of laser energy deposition.

Despite these challenges, the potential benefits of high energy density physics and ICF are enormous. In addition to providing a clean and virtually limitless source of energy, laser plasma interactions could also play a crucial role in advancing our understanding of fundamental physics and the behavior of matter at extreme conditions. In this introduction, we review the recent developments in the field of ICF, including the direct and indirect drive approaches, shock ignition, and the role of laser-plasma interactions and foams in ICF research. We then discuss the current state of theory and experiments related to the excitation of parametric instabilities and generation of hot electrons, with the focus on unresolved problems. Finally, we explore the use of foams in ICF, including their potential benefits and challenges, and outline areas for future research and development.

## 0.2 Direct and indirect drive in ICF

Nuclear fusion research has already more than 80-year history. In 1938, Carl Friedrich von Weizsäcker and Hans Bethe have proposed a first model for the nuclear fusion reactions occurring inside stars as a source of their energy release. According to their analysis, the fusion of light nuclei may release a significant amount of energy even larger than splitting of heavy nuclei [13], [14].

The actual idea of using the fusion reactions for the energy production was born in the late 1940s, when physicists have measured the cross section of deuterium-tritium (DT) reaction and aimed at recreating the mechanism of nuclear fusion on Earth, however in an uncontrolled manner. On October 31, 1952, the US detonated their first nuclear bomb based on the fusion reaction releasing over ten megatons of TNT equivalent [15]. In this scenario, the fission reaction was used as an energy source for compression and ignition of the DT fuel. The energy yield in this explosion was 800 times the larger the Hiroshima fission bomb.

It is not possible to use such explosions as a source of clean and safe energy. One needs to achieve ignition with less powerful explosions and adapt the fusion energy release to the electrical energy production. To do that in a controllable way, first of all the mass of DT fuel should be small and it should be compressed to the very high densities. Laser drivers that compress energy in space and time are required to produce such extreme conditions in the laboratory.

In direct drive ICF, laser beams are focused directly onto the fuel pellet, delivering the energy needed for fuel implosion and heating. The energy of the laser beam is absorbed

by the outer layers of the capsule, causing it to expand and to compress the inner dense shell by the force of reaction. This approach has the advantage of being more efficient, as the energy is delivered directly to the capsule, but it is also more challenging to implement due to the high level of homogeneity of energy deposition required.

In the direct drive (DD) approach [2], [11], [16], [17], the laser energy deposited at the outer surface of the target because laser radiation cannot penetrate deeply in plasma: it is reflected from the critical density $n_{\rm cr}$, which is inversely proportional to the square of the laser wavelength $\lambda$ (in microns):

$$n_{\rm cr} = 1.115 \times 10^{21} \lambda_{\mu\rm m}^{-2}\,{\rm cm}^{-3}.$$

This density for the laser wavelength in optical range is about hundred times smaller than the solid density. So, the energy to the ablation surface is transported by electron heat conductivity. This additional step in the energy transfer affects the efficiency target implosion. Ablation pressure plays a critical role in the ICF performance, as it is used to compress the fuel to the necessary density and temperature for the fusion reaction to occur.

Ablation pressure can be calculated using the following formula [2], [18]:

$$p_{\rm abl} \simeq 57(\eta_{\rm abs} I_{15}/\lambda_{\mu\rm m})^{2/3}\,{\rm Mbar},$$

where $p_{\rm abl}$ is the ablation pressure in megabars, $\eta_{\rm abs}$ is the laser absorption coefficient, $I_{15}$ is the laser intensity in units of $10^{15}$ W/cm$^2$, and $\lambda_{\mu\rm m}$ is the laser wavelength in microns. The laser energy has to be absorbed uniformly over the surface of the target so that the ablated material expands spherically and produces a symmetric implosion. Laser absorption coefficient and wavelength are important factors in producing the ablation pressure, as they determine the amount of energy that is absorbed in the target and the depth where the energy is deposited.

Understanding and controlling the ablation pressure is crucial for optimizing the performance of a direct drive ICF target. It is an active area of research and development, with ongoing efforts to improve the accuracy of laser propagation calculations and the design of target structure that can mitigate the inhomogeneity of laser energy deposition.

To achieve the necessary conditions for fusion, the fuel must be compressed to a density about thousand times higher than the solid density. This can be achieved on the high-energy, multi-beam laser facilities, such as the Laser Mégajoule (LMJ) in France [19]–[21] and the National Ignition Facility (NIF) in the United States [22]–[24]. However, these facilities are designed for indirect drive ICF scheme and cannot provide a required implosion symmetry for the direct drive.

In indirect drive ICF, the energy is first absorbed by a surrounding cylindrical case called "hohlraum," and then transferred to the pellet through thermal radiation. This approach has the advantage of providing a more symmetric ablation pressure, but it is also less efficient, as large fraction of the laser energy is lost in the conversion process and enhanced radiation losses.

The hohlraum is typically a thin, hollow cylindrical container made of a high-density material such as gold, lead or uranium. It is designed to absorb energy of the laser pulse and convert it into thermal radiation, which is then transferred to the pellet. The hohlraum is irradiated with many laser beams, which penetrate inside through two holes at the ends of the cylinder, heat the inner surface and generate a strong near-thermal radiation.

The fuel capsule is a shell made of a fusible material such as deuterium-tritium (DT) ice and covered by an outer shell of light material, such a berillium or carbon, serving as ablator. It is irradiated from the hohlraum walls, causing ablation of the outer layer and compression of the inner layer containing fuel.

The efficiency of the indirect drive approach depends on the ability of the hohlraum to absorb and convert the laser energy into thermal radiation, as well as the ability of the fuel pellet to absorb the thermal radiation and reach the necessary conditions for fusion. By using a high-$Z$ material, such as gold, for the hohlraum cavity, it is possible to achieve a high efficiency in the conversion of laser energy into X-rays, with more than $60 - 70\%$ of the laser energy being converted. The radiation temperature of the hohlraum depends on the laser energy and the volume of the hohlraum. According to Stefan-Boltzmann's law, the radiation temperature can be estimated using the equation $I_X = \sigma_{SB} T_X^4$, where $I_X$ is the intensity of the thermal radiation, $\sigma_{SB}$ is the Stefan-Boltzmann constant, and $T_X$ is the radiation temperature. A radiation temperature of $300 - 400$ eV is needed for the fuel implosion. It corresponds to an intensity of approximately $10^{15}$ W/cm$^2$.

Despite the lower efficiency of indirect drive, it has several advantages over direct drive. It allows for the use of lower quality laser beams, which are easier to produce and more readily available. It is also more robust, as irradiation in the hohlraum is less sensitive to laser mis-pointing, thus reducing the risk of hydrodynamic instabilities during the shell implosion.

However, indirect drive also has its challenges. The accuracy of the temperature and density calculations depends on a number of factors, such as the accuracy of the hohlraum radiation model and the reflectivity of the fuel pellet. In addition, the transfer of energy from the hohlraum to the fuel pellet is limited in its efficiency. Estimates suggest that the energy coupling into the capsule cannot be more than 0.2, indicating that a significant portion of the energy can be lost in the process. So, the direct drive approach is preferred

for energy production with fusion reactions.

One promising approach for achieving controlled thermonuclear fusion for energy production is the shock ignition scheme [19], [23], [25], [26], which is a two-stage process. The first laser pulse enables a more stable shell compression at a lower implosion velocity. Fuel ignition is achieved with the second high-intensity laser spike that launches a strong shock wave, which converges to the center and heats the fuel at the moment of stagnation. This approach has the advantage of being more flexible to achieve the necessary fuel densities and temperatures in a two-step process, rather than relying on temporal profiling of a single laser pulse as in the traditional ICF approach.

The important aspects of the shock ignition scenario are the amplitude and timing of the shock wave, which must be carefully controlled in order to achieve the fuel ignition conditions. The shock wave must be generated at the right time and with the right amplitude in order to effectively compress and heat the fuel [25]. However, it is important to note that in this scenario, the additional shock is primarily used for heating rather than compressing the fuel. In addition, the shock wave must be carefully matched to the fuel density in order to ensure that it is absorbed in the center and does not reflected off it.

The shock ignition scenario has been studied both theoretically and experimentally. It has been demonstrated experimentally that it is possible to achieve the shock pressures in excess of 300 Mbar needed for ignition and increase the neutron yield [27]. Numerical simulations demonstrated an improved shell stability during the implosion due to a smaller implosion velocity and acceleration.

Despite the promising features of the shock ignition scenario, there are still several challenges that need to be addressed in order to make it a viable approach for fusion energy production. These include the need for precise control of the shock wave timing and intensity, as well as the need for a better understanding the complex physical processes involved in the laser absorption and the role of hot electrons in the energy transport. It is important to note that in shock ignition, the interaction of the laser peak intensity significantly above the threshold of parametric instabilities with long corona cannot be avoided. Further research and development is needed to address these challenges and to optimize the performance of shock ignition scheme.

## 0.3 Use of foams in high energy density physics

The use of foams in the high energy density physics and ICF has gathered significant interest in recent years due to their potential to improve the performance of ICF targets and secondary radiation sources. Foams can be used in a variety of ways, as a material for

laser beam smoothing and target design, as a source of bright x-rays, energetic electrons, and ions.

Foams can be used in both direct and indirect drive ICF approaches to improve the target performance. In direct drive ICF, foams are used for reducing the laser imprint and improving the shell stability with respect to hydrodynamic instabilities. In the indirect drive, foams are used for lining the inner surface of hohlraum in order to prevent premature wall expansion and distortion of the implosion symmetry.

Laser beams irradiating the target can be significantly distorted due to the aberrations in the laser optics elements and amplifiers and due to the plasma instabilities. Laser beam smoothing aims at removing the laser imprint at the ablation surface, improving the uniformity of energy delivery and implosion symmetry. In laser beam smoothing with foam, the foam material is used as a medium for laser absorption. This approach enhances lateral transport and mitigates inhomogeneities in laser energy deposition. This allows to reduce the pressure modulations at the ablation surface, which provide a seed for the Rayleigh-Taylor hydrodynamic instability during the shell acceleration. Foams have shown their efficiency in smoothing laser beams and reducing the laser imprint in a number of experiments [28]–[32]. Another advantage of using foam is that it can absorb radiation with high incidence angles, allowing for wider laser spots on the target and reducing the number of required laser beams.

Low density foams irradiated by intense laser pulses can also serve as sources of bright x-rays, energetic electrons, and ions. The x-rays produced by foam [33] can be used for diagnostic purposes, such as imaging of the implosion process of a fuel pellet. The energetic electrons and ions produced in laser-irradiated foams [34]–[37] can be used for diagnostic purposes providing high resolution images of the imploding shell and compressed core. However, there are many unresolved questions and challenges that need to be addressed in order to fully realize the potential of foams in ICF. Among them are the time of homogenization of the foam structure [38] and its contribution to the laser imprint, the velocity of propagation of the laser-driven ionization wave in foam [39]–[41], the energy partition between different particle species and the radiation effects.

The advantage of foams compared to homogeneous materials consists in their flexibility and possibility of controlling their density and geometrical shape. Several techniques have been designed to optimize the properties of foams, such as density, pore size, shape and structure of solid elements. However, theoretical understanding and numerical modeling of laser interaction with foams is insufficient. Modeling of foams with a homogeneous material of equivalent density underestimates the laser energy deposition and ionization time. Further research is needed to fully understand the mechanisms of structural transitions in the foam, the role foam microstructure in the laser energy absorption and energy

transport. This will help to improve the efficiency of foam applications in high energy density physics.

## 0.4 Statement of the problem

The goal of this research is to investigate the effects of laser plasma interaction in application to ICF. Two aspects are considered. The first one is the competition between different parametric instabilities, namely SBS and SRS, in the context of shock ignition. To this end, we have performed one- and two-dimensional kinetic simulations with the goal to define conditions optimizing the laser energy deposition and controlling the hot electron production. The second aspect is theoretical and numerical modeling of laser interaction with a foam target, the foam transformation in a plasma and its homogenization.

In the first part of this study, we examine how one can control the level of nonlinear laser absorption and scattering in a hot, weakly collisional plasma by manipulating plasma parameters such as ion acoustic wave damping, divergence of the plasma expansion velocity, and laser bandwidth. In the second part of this study, we investigate the microscopic processes of laser absorption and scattering from structural elements of a sub-wavelength size and foam transformation in a plasma through a combination of expansion and ablation. A theoretical analysis is completed with two-dimensional numerical simulations.

Overall, this research aims at improving our understanding of the role of laser-matter interaction processes under the ICF conditions needed for the design of a new generation of more efficient fusion targets.

## 0.5 Organization of the manuscript

The present work consists of four Chapters, which focus on the study of nonlinear laser absorption in an underdense plasma and in a low density foam under the ICF conditions.

- In **Chapter 1**, we provide a short review of known results related to parametric instabilities in ICF and their role in the context of shock ignition. We begin by discussing collisional absorption in inhomogeneous plasmas and its implications for ICF. Next, we delve into SBS, including its temporal gain, theory and experiments, and the role of ion acoustic waves in two species plasmas. We also explore the convective SBS, spatial gain, the role of two ion species, and flow divergence, and provide examples of practically interesting parameters for ICF. We then turn our attention to SRS, covering its temporal gain, theory and experiments, and the spatial gain and absolute instability. We also consider the role of collisional absorption,

hot electrons, and cavitation. Finally, we discuss TPD, including its general characteristics and competition with SRS in relation to laser absorption and hot electron production.

- **Chapter 2** is focused on numerical simulations of SBS and SRS and on analysis of the results obtained. We begin by discussing the methodology of numerical simulations of plasma dynamics using particle-in-cell (PIC) code Smilei, a massively parallel fully relativistic electromagnetic simulation tool. This approach involves coupling hydrodynamic and PIC simulations for interpretation of experiments and setting the input parameters. Next, we explore methods for controlling SBS, including the role of ion damping, laser bandwidth, collisions, and flow velocity divergence in particle energy evolution. We then consider laser backscattering and transmission, including the intensity and spectra of the scattered light. We also analyze the hot electron flux, including the two-temperature parametrization and temporal dependence. We discuss ion heating and acceleration, including the processes that contribute to these phenomena and their impact on SBS and SRS. Finally, we compare the results of one- and two-dimensional simulations, exploring the advantages and limitations of each approach. In conclusion, this chapter provides a comprehensive analysis of numerical simulations of SBS and SRS.

- **Chapter 3** delves into the interaction of laser radiation with a single elementary cell or pore in a foam. The pore contains a solid cylinder with initial radius $a_0$ and density $\rho_s$. To model the laser absorption and scattering from a cylinder with a radius comparable to the wavelength, the Mie theory can be used. However, this standard approach considers homogeneous scattering objects, while the radial inhomogeneity of the cylinder plays a crucial role in our study as it enables resonance absorption near the critical density. Therefore, in this study, we examine a scenario that can be mathematically analyzed with two simplified physical assumptions. Firstly, we explore the case of an infinitely long straight cylinder exposed to a plane wave incident at an oblique angle. Secondly, we consider a cylindrical object with radial density distribution that is axially symmetric. Despite the anisotropic nature of laser energy deposition and resulting cylinder expansion, this example offers valuable insights into the physics of laser interaction with a foam. Through mathematical analysis, we investigate the absorption and scattering of laser radiation from the cylindrical object, leading to the development of a model that explains the resulting cylinder expansion. Additionally, we study the characteristics of laser radiation absorption in a single sub-wavelength cylinder and explore the factors affecting it. Our findings reveal the significance of the radial inhomogeneity of the

cylinder in enabling resonance absorption near the critical density, which plays a crucial role in laser absorption in a foam.

- **Chapter** 4 is focused on the use of PIC simulations for studying the kinetics of plasmas in underdense foam targets. The chapter confirms and evaluates the characteristics of laser interaction with sub-wavelength cylinders predicted by the analytic theory, using the code Smilei. The simulations investigate the laser absorption efficiency in solid elements, which strongly depends on their structure, shape and orientation with respect to the laser polarization. We find that laser polarization perpendicular to the cylinder axis leads to enhanced laser absorption due to plasma resonance, while for the laser polarization parallel to the cylinder axis absorption occurs due to electron collisions. The evolution of the cylinder density over time is described by a bell-shaped exponential function characterised by three parameters: central density, radius and steepness. Two distinct phases of cylinder evolution are observed: the radius of the cylinder decreases in the first phase, while in the second phase, the cylinder expands and initially solid material transforms in a plasma. The simulation is stopped when the cylinder maximum density drops below the critical density and the ablated plasma fills the pore. We find that the ion temperature at the end of homogenization process obtained in the simulation is significantly larger than the electron temperature, which is consistent with available experimental data. The small size of the solid element in comparison to the pore size leads to small laser absorption in a single pore. Hence, laser heating and foam homogenization involve many pores, resulting in a homogenization layer thickness that is inversely proportional to the pore size. These findings provide an input for the development of a multi-scale model for foam heating by laser radiation.

The main results obtained in this work are summarized in Chapter 5.

# Chapter 1

# Laser plasma interaction and parametric instabilities

This chapter provides an overview of the parametric instabilities that can occur in the context of ICF, including Stimulated Brillouin Scattering (SBS) and Stimulated Raman Scattering (SRS). We first discuss the basics of laser propagation in an inhomogeneous plasma, including the role of collisional absorption. We then focus on SBS, discussing its temporal and spatial gain and how factors such as flow velocity and laser bandwidth can affect its performance. In addition, we consider the potential impact of multiple ion species on SBS. Next, we discuss SRS, examining its temporal and spatial characteristics and the role of cavitation and hot electrons. We briefly mention two plasmon decay, noting that it is generally less important than SRS in the context of shock ignition ICF. This chapter is concluded with the discussion of processes of generation of energetic electrons and their role in laser energy absorption in plasma.

## 1.1 Laser propagation in plasmas and collisional absorption

Laser propagation in an inhomogeneous plasma is a complex phenomenon that has a significant impact on the performance of inertial confinement fusion (ICF) experiments. The evolution of the laser light as it travels through plasma is determined by the interaction between the laser field and the plasma electrons, which can be described using the Maxwell equations complemented in the linear approximation by the plasma response characterized by the dielectric permittivity.

Dielectric permittivity, $\epsilon(\omega, \mathbf{r})$ describes the plasma response – a relation between the electric field induced in plasma and the external electric field. It enters the macroscopic Maxwell's equations, which govern the behavior of electromagnetic fields in space and

time. In the frequency domain representation, the electric and magnetic fields are proportional to $\exp(-i\omega t)$, and the Maxwell's equations in an inhomogeneous and isotropic media can be written as:

$$\begin{aligned} \nabla \cdot \mathbf{E} &= -\frac{1}{\epsilon}\nabla\epsilon \cdot \mathbf{E}, \\ \nabla \cdot \mathbf{H} &= 0, \\ \nabla \times \mathbf{E} &= i\frac{\omega}{c}\mathbf{H}, \\ \nabla \times \mathbf{H} &= -i\frac{\omega}{c}\epsilon\,\mathbf{E}, \end{aligned} \tag{1.1}$$

where $\mathbf{E}$ and $\mathbf{H}$ are the electric and magnetic field, and $c$ is the speed of light.

The wave equations for electric and magnetic field separately can be derived from the (1.1) by taking the curl of the electric and magnetic fields:

$$\begin{aligned} \triangle\mathbf{E} + \nabla(\nabla \ln\epsilon \cdot \mathbf{E}) + \left(\frac{\omega}{c}\right)^2 \epsilon(\omega, \mathbf{r})\mathbf{E} = 0, \\ \triangle\mathbf{H} + \nabla\epsilon(\omega, \mathbf{r}) \times \nabla \times \mathbf{H} + \left(\frac{\omega}{c}\right)^2 \epsilon(\omega, \mathbf{r})\mathbf{H} = 0. \end{aligned} \tag{1.2}$$

In the case of light wave propagation in a homogeneous and uniform plasma, the gradient of the dielectric permittivity $\nabla\epsilon$ is equal to zero and the divergence of the electric field $\nabla\cdot\mathbf{E}$ is equal to zero. This means that electric and magnetic field satisfy identical equations:

$$\begin{aligned} \Delta\mathbf{E} + \left(\frac{\omega}{c}\right)^2 \epsilon(\omega)\mathbf{E} = 0, \\ \Delta\mathbf{H} + \left(\frac{\omega}{c}\right)^2 \epsilon(\omega)\mathbf{H} = 0. \end{aligned} \tag{1.3}$$

The propagation of light waves in such plasmas can be described by the Helmholtz equation (1.4), which is a scalar equation that applies to each component of the electric and magnetic fields separately. This equation, named after Hermann von Helmholtz, was originally derived from the Maxwell equations and predicts the propagation of electromagnetic waves in a free space where $\epsilon = 1$. These waves were first observed by Heinrich Hertz, a student of Helmholtz, several years after the publication of Helmholtz's theoretical paper. The homogeneous Helmholtz equation is given by:

$$\left[\triangle + \left(\frac{\omega}{c}\right)^2 \epsilon(\omega)\right] u(\omega, \mathbf{r}) = 0 \tag{1.4}$$

where $u(\omega, \mathbf{r})$ is the scalar wave amplitude, written in the frequency domain, that represents any component of the electric or magnetic field. In the most simple case of isotropic

collisionless media, the dielectric constant can be written:

$$\epsilon(\omega) = 1 - \frac{\omega_{\rm pe}^2}{\omega(\omega + i\nu_{\rm ei})}, \tag{1.5}$$

where $\omega_{pe}$ is the plasma frequency and $\nu_{ei}$ is the electron-ion collision frequency. The dielectric permittivity $\epsilon(\omega)$ can be decomposed into a real and an imaginary part as $\epsilon = \epsilon' + i\epsilon''$. In the case where the electron-ion collision frequency $\nu_{\rm ei}$ is much smaller than the laser frequency $\omega$, that is, $\omega \gg \nu_{\rm ei}$, we have:

$$\begin{aligned} \epsilon' &\simeq 1 - \left(\frac{\omega_{\rm pe}}{\omega}\right)^2, \\ \epsilon'' &\simeq \frac{\nu_{\rm ei}}{\omega}\left(\frac{\omega_{\rm pe}}{\omega}\right)^2. \end{aligned} \tag{1.6}$$

The frequency-dependent nature of the dielectric permittivity is a direct result of the dispersive property of plasmas.

The dispersion relation for electromagnetic waves can be obtained by assuming that $u$ has the form of $u_0 \exp(-i\mathbf{k}\cdot\mathbf{r})$. Then the Helmholtz equation reduces to a dispersion equation given by:

$$-k^2 + \left(\frac{\omega}{c}\right)^2 \epsilon(\omega) = 0. \tag{1.7}$$

It provides a relation between the wavevector $\mathbf{k}$ and the angular frequency $\omega$ of the electromagnetic wave. Neglecting collisions, that is, setting the imaginary part of the permittivity to zero, $\epsilon'' = 0$, the dispersion relation (1.7) for electromagnetic waves is given by:

$$k^2c^2 = \omega^2 - \omega_{\rm pe}^2, \tag{1.8}$$

This equation shows that wave propagation can only occur when $\omega > \omega_{\rm pe}$, in which case the wavevector $k$ is real. If $\omega < \omega_{\rm pe}$, the plasma electrons are shielding the light wave field. In a vacuum, $\omega_{\rm pe} = 0$, the free-space wavevector of the electromagnetic wave is $k_0 = \omega/c$. Since the plasma frequency depends on electron density $n_e$ as $\omega_{\rm pe} = \sqrt{4\pi e^2 n_e/m_e}$, where $m_e$ and $e$ are the electron mass and charge, the condition $\omega = \omega_{\rm pe}$ defines the critical density beyond which a light wave does not propagate:

$$n_{\rm cr} = \frac{\epsilon_0 \omega^2 m_e}{e^2}. \tag{1.9}$$

Critical density defines the plasma region that can be accessed by a laser. Plasma densities higher than the critical density, where the dielectric permittivity is negative, cannot be reached by the laser.

**Laser collisional absorption in inhomogeneous plasma**

Exact solutions to the Helmholtz equation in inhomogeneous media can be found only in certain special cases. We consider here a general approach for obtaining approximate solutions to Eq. (1.2) using a small parameter $\lambda/L_n \ll 1$. This small parameter represents a ratio of the laser wavelength $\lambda = 2\pi/k$ to the local plasma scale length $L_n$, which is defined as $L_n = n_e/|\nabla n_e|$. Let us assume that the wave propagates in the $z$-direction parallel to the gradient of electron density and the electric field is of the form $\mathbf{E} = \{E_x(z), E_y(z), 0\}$. The $z$-component of electric field is zero for the transverse wave. It is sufficient to solve Eq. (1.4) for one field component:

$$\frac{d^2 E_{x,y}}{dz^2} + \left(\frac{\omega}{c}\right)^2 \epsilon(\omega, z) E_{x,y} = 0. \tag{1.10}$$

The electric field is expressed as a product of a slowly varying amplitude $A(z)$ and a rapidly varying phase $\psi(z)$,

$$E = A(z) \exp[ik_0 \psi(z)]. \tag{1.11}$$

This approach is known as the eikonal or WKB (Wentzel-Kramers-Brillouin) approximation. Substituting this expression into Eq. (1.10) and separating the real and imaginary parts, we obtain the following system of equations:

$$2\frac{dA}{dz}\frac{d\psi}{dz} + A\frac{d^2\psi}{dz^2} = 0, \qquad \frac{d\psi}{dz} = \sqrt{\epsilon}, \tag{1.12}$$

which yields:

$$E_{x,y}(z) = \frac{E_0}{\epsilon^{1/4}} \exp\left[ik_0 \int_0^z dz' \sqrt{\epsilon(\omega, z')}\right], \tag{1.13}$$

where the $E_0$ is the free space electric field. This result illustrates that the amplitude of the electric field increases as $E_0\epsilon^{-1/4}$ as the wave propagates towards the critical density and $\epsilon$ decreases. The validity of WKB approximation can be determined by comparing the relative magnitude of the second derivative term of the field amplitude, $d^2A/dz^2$, which is neglected in Eq. (1.12), with the retained first order terms in the Helmholtz equation. This ratio is represented mathematically as:

$$\frac{\omega}{c}\left(\frac{\epsilon}{2}\right)^{3/2} \gg \left|\frac{d\epsilon}{dz}\right|. \tag{1.14}$$

We now examine the collisional damping of a light wave propagating in an inhomogeneous plasma. This process of collisional absorption is also called the inverse Bremsstrahlung. Electron collisions with ions disrupt the regular motion of electrons in a laser field, leading to the transfer of a portion of the electron quiver energy to a chaotic thermal energy. The

dielectric permittivity (1.5), which accounts for these collisions, affects the wave vector $k_z = k_0\psi(z)$ as described by the complex expression in the second equation in (1.12). When considering normal incidence and assuming the collision frequency to be small, $\nu_{\mathrm{ei}} \ll \omega$, the imaginary part of the $z$-component of the wave vector can be expressed as:

$$\operatorname{Im} k_z = \frac{\nu_{\mathrm{ei}}}{2c}\left(\frac{\omega_{\mathrm{pe}}}{\omega}\right)^2\left(1-\frac{\omega_{\mathrm{pe}}^2}{\omega^2}\right)^{-1/2}. \tag{1.15}$$

The intensity of an electromagnetic wave in plasma decreases exponentially, following the imaginary part of the eikonal, $I \propto |E^2| \propto \exp(-2\operatorname{Im}\psi)$. The collisional absorption is defined by the integral of expression (1.15) over the wave trajectory. Since the electron collision frequency is proportional to the plasma density, it can be expressed as $\nu_{\mathrm{ei}} = \nu_{\mathrm{ei}}^*(\omega_{\mathrm{pe}}/\omega)^2$, where $\nu_{\mathrm{ei}}^*$ is the electron-ion collision frequency evaluated at the critical density. Then the intensity of the laser field in plasma can be expressed as:

$$I(z) = I_0 \exp\left[-\frac{\nu_{\mathrm{ei}}^*}{c}\int_0^z dz'\left(\frac{\omega_{\mathrm{pe}}}{\omega}\right)^4\left(1-\frac{\omega_{\mathrm{pe}}^2}{\omega^2}\right)^{-1/2}\right], \tag{1.16}$$

where $I_0 = (c/8\pi)\,|E_0^2|$ is the incident laser intensity. To find the total collisional absorption coefficient, one must integrate (1.16) from the plasma entrance at $z = 0$ to the turning point at $z = z_0$, and then multiply the result by 2 to account for the absorption of both the incident and reflected waves.

$$f_{\mathrm{coll.abs}} = 1 - \exp\left[-2\frac{\nu_{\mathrm{ei}}^*}{c}\int_0^{z_0} dz'\left(\frac{\omega_{\mathrm{pe}}}{\omega}\right)^4\left(1-\frac{\omega_{\mathrm{pe}}^2}{\omega^2}\right)^{-1/2}\right]. \tag{1.17}$$

The integrand in the exponential of this expression is proportional to the square of the electron density, as the square of the plasma frequency is proportional to the density. As a result, the dominant part of collisional absorption occurs in the vicinity of the reflection point, with approximately 95% of the absorption occurring within the interval between the density at the reflection point and half of that value. Some examples for the practically interesting parameters for the ICF are presented in Sec. 1.4.2.

## 1.2 Model of the finite bandwidth laser

Theoretical studies have shown that spreading laser power over a wide frequency range can significantly decrease the growth rates of parametric instabilities. Thomson and Karush analyzed the suppression of parametric instabilities driven by a broadband laser with a discrete spectrum [42]. This model was later extended to continuous spectrum by Pesme et al. [43]. It was found that the growth rates of parametric instabilities decrease as the

bandwidth of the laser increases in the linear stage. In recent years, numerical simulation tools have been used to study the interaction of broadband lasers with plasmas. Zhao et al. numerically investigated several parametric instabilities driven by broadband lasers [44] and proposed a new laser model, the decoupled broadband laser, which is more efficient in suppressing these instabilities [45]. Follett et al. found that the increase of laser bandwidth significantly increases the thresholds of absolute SRS and TPD [5], [46]. Zhou et al. focused on the dynamics of non-linear stage of SRS [47] and found that a higher frequency shift tolerance can enhance SRS on this stage.

There are several methods for modeling laser bandwidth, such as the Kubo-Anderson process (KAP) and the use of a mosaic of beamlets [48]. The Kubo-Anderson process (KAP) is a widely used method for modeling broadband lasers in early studies on the suppression of laser-plasma instabilities due to its analytical tractability. The KAP describes a laser as having a constant amplitude and frequency, but with random phase jumps that occur at Poisson-distributed intervals with a mean jump time $\tau_c$:

$$\tau_c \equiv \int_{-\infty}^{+\infty} d\tau \, |g(\tau)|^2, \tag{1.18}$$

where

$$g(\tau) \equiv \frac{\langle E_0^*(t) E_0(t+\tau) \rangle}{\langle |E_0(t)|^2 \rangle}, \tag{1.19}$$

is the correlation function and angular brackets $\langle ... \rangle$ define the time average. The amplitude of these phase jumps is uniformly distributed over the range $(0, 2\pi)$. The time-enveloped KAP laser, represented by $g(\tau) = \exp(-|\tau|/\tau_c)$, describes the probability that no phase jump occurs within the time interval $[t, t+\tau]$.

The Wiener-Khinchin theorem can be applied to a laser with a KAP bandwidth to obtain its power spectrum:

$$I(\omega) = \frac{I_0}{2\pi} \int_{-\infty}^{+\infty} d\tau \, g(\tau) \exp(i\omega\tau) = \frac{I_0}{\pi} \frac{1/\tau_c}{\omega^2 + (1/\tau_c)^2}, \tag{1.20}$$

which demonstrates that the power spectrum of a laser with a KAP bandwidth corresponds to a Lorentzian spectrum. Full width at half maximum (FWHM) of the KAP spectrum is related to the correlation time as $\Delta\omega = 2/\tau_c$.

In this study, we adopt a numerical approach where the broadband laser is represented as a phase modulated driver:

$$E_0 = a_0 \sin[\omega_0 t + \phi(t)], \tag{1.21}$$

where $a_0$ is normalized laser amplitude, $\omega_0$ is the laser frequency and $\phi$ were randomly

selected from a uniform distribution over $(0, 2\pi)$ within a given time interval $\tau_c$.

## 1.3 Stimulated Brillouin scattering

This section describes the process SBS in plasma: the temporal and spatial gains, the role of multiple ion species on the ion wave dispersion and damping, and the effects of the plasma flow divergence on convective SBS. We also provide examples of practically interesting parameters.

### 1.3.1 Temporal gain: theory and experiments

In 1922, Léon Brillouin proposed the idea of a combination scattering [49], which occurs as a result of an interaction between an electromagnetic wave and an acoustic wave (phonon) in a solid. Kroll [50] gave a treatment of SBS in the context of a high-intensity electromagnetic wave interacting with a solid, where the nonlinear coupling happens through the elasto-optic effect. He also acknowledged a similarity between SBS and optical parametric amplification. Comprehensive treatments of SBS in plasmas have been given by Liu et al. [51] and Forslund et al. [52]. Forslund et al. [53], [54] also described early numerical simulations of SBS in plasma, as well as Kruer et al. [55]. Galeev et al. [56] provided a treatment of side scattering and found a maximum gain for scattering at 90 degrees. Experimental evidence for the large angle SBS scattering was reported by Neuville et al. [57].

Stimulated Brillouin scattering is a three-wave parametric instability corresponding to a decomposition of the pump electromagnetic wave with a frequency $\omega_0$ and wave vector $\mathbf{k}_0$ into a scattered electromagnetic wave, $\omega_s$, $\mathbf{k}_s$, and an ion acoustic wave with a frequency $\omega_{\mathrm{IAW}} \ll \omega_0$ and wave vector $\mathbf{k}_{\mathrm{IAW}}$. The three-wave matching conditions for the SBS parametric instability read:

$$(\omega_0, \mathbf{k}_0) = (\omega_s, \mathbf{k}_s) + (\omega_{\mathrm{IAW}}, \mathbf{k}_{\mathrm{IAW}}), \tag{1.22}$$

The characteristic temporal growth rate $\gamma$ for SBS can be expressed as [12]:

$$(\gamma + \gamma_{\mathrm{IAW}})(\gamma + \gamma_s) = \gamma_0^2, \tag{1.23}$$

where $\gamma_{\mathrm{IAW}}$ and $\gamma_s$ are the amplitude damping rates of the ion-acoustic and scattered light waves, respectively, and $\gamma_0$ is the growth rate in the absence of damping. From this equation, we can see that the condition $\gamma_0 = \sqrt{\gamma_{\mathrm{IAW}}\gamma_s}$ represents the threshold for the SBS instability. In the case of backward scattering, $\mathbf{k}_s \approx -\mathbf{k}_0$, the characteristic temporal

growth rate of SBS reads [12], [51]:

$$\gamma_0 = \frac{1}{4}\omega_{\rm pi} v_{\rm os}\sqrt{\frac{k_{\rm IAW}}{\omega_0 v_{\rm IAW}}}, \tag{1.24}$$

where $\mathbf{k}_{\rm IAW} \approx 2\mathbf{k}_0$, $k_0 = (\omega_0/c)\,(1-n_e/n_{\rm cr})^{1/2}$, $\omega_{\rm pi}$ is the ion plasma frequency, $v_{\rm IAW}$ is the ion acoustic wave phase velocity, and $v_{\rm os}$ is the amplitude of the electron quiver velocity in the laser field.

The temporal gain is reduced if the pump wave has the finite spectral bandwidth $\Delta\omega_0 \gtrsim \gamma_0$ [42], [43], [58], [59]. The growth rate can be estimated with an approximate expression [43], [58]:

$$\gamma_{\Delta\omega_0} = \frac{\gamma_0^2}{\sqrt{\gamma_0^2 + \xi^2\Delta\omega_0^2}}, \tag{1.25}$$

where the numerical coefficient $\xi$ in the right hand side depends on the pump wave power spectrum. The temporal gain is also affected by the ion acoustic wave damping $\gamma_{\rm IAW}$, which is of particular importance in a multi-ion species plasma considered in Sec. 1.3.2.

### 1.3.2 Ion acoustic waves in two species plasmas

Considering fully ionized, neutral non-magnetized plasma, the frequencies and damping rates of ion acoustic waves are given by a zeros of the dielectric function, i.e. $\epsilon(\omega, k) = 0$ [60]–[62]. The longitudinal component of the dielectric function is given by:

$$\epsilon(\omega, k) = 1 + \chi_e + \chi_i = 0, \tag{1.26}$$

where $\chi_j$ denotes the susceptibility of electrons (e) or ions (i). It could be expressed as:

$$\chi_j = (k\lambda_{Dj})^{-2}\,[1 + \xi_j\,\mathcal{Z}(\xi_j)], \tag{1.27}$$

where $\xi_j = \omega/(\sqrt{2}\,k\,v_{Tj})$ is a complex variable, $\omega$ and $k$ are the frequency and wave number of given mode, $v_{Tj} = \sqrt{T_j/m_j}$, $T_j$ and $m_j$ are the temperature and mass of particle, respectively, $\lambda_{Dj} = \sqrt{T_j/4\pi n_j Z_j^2 e^2}$ is the Debye length, $n_j$ and $Z_j$ are the density and charge of specie $j$, respectively, and $\mathcal{Z}$ is the Fried-Conte $\mathcal{Z}$-function [63]:

$$\mathcal{Z}(\xi) = \frac{1}{\sqrt{\pi}}\int_{-\infty}^{+\infty} dv\,\frac{e^{-v^2}}{v-\xi} = i\,\sqrt{\pi}\,\mathrm{e}^{-\xi^2}\,[1 - \mathrm{erf}(-i\,\xi)], \tag{1.28}$$

where $\mathrm{erf}(-\mathrm{i}\,\xi)$ is an error function defined by:

$$\mathrm{erf}(\xi) = \frac{2}{\sqrt{\pi}}\int_0^{\xi} \mathrm{d}\eta\,\mathrm{e}^{-\eta^2}.$$

Plastics are often used as ablators in ICF target designs. Made of light ions, these materials are ablated at high velocities, creating high ablation pressure. For these reasons, hydrocarbon (CH) plasmas are often used for studies of laser-plasma interactions [62], [64]–[67]. Additionally, low-$Z$ materials are often used to create foams [32], [37], [39]–[41].

In hydrodynamic simulations, the plasma is modeled with two-temperature, single-fluid equations. Consequently, a CH plasma is described with one ion species with an effective charge, $Z_{\text{eff}} = (Z_C + Z_H)/2 = 3.5$, and mass $m_i = A_{\text{eff}} m_p$, where $A_{\text{eff}} = (A_C + A_H)/2 = 6.5$ and $m_p$ is the proton mass. A similar approach is often used in kinetic simulations, as it allows for reducing the required computational resources. This approximation, however, may significantly underestimate the damping of ion acoustic waves and, consequently, the characteristics of SBS, as demonstrated in Sec. 1.3.3.

Dispersion equation for ion acoustic waves (1.26) in a single ion species plasma can be written as:

$$1 + (k\lambda_{\text{De}})^2 + i\sqrt{\frac{\pi}{2}\frac{m_e}{m_p}} + \frac{Z_{\text{eff}} T_e}{T_i}\left[1 + x\sqrt{\frac{A_{\text{eff}} T_e}{2T_i}}\,\mathcal{Z}\left(x\sqrt{\frac{A_{\text{eff}} T_e}{2T_i}}\right)\right] = 0, \tag{1.29}$$

where the second and third terms represent the electron contribution to the dielectric function, $x = \omega/(k\, c_{s,H})$ is the ratio of the phase speed to the hydrogen sound speed $c_{s,H} = \sqrt{T_e/m_p}$. The phase velocity, $v_{\text{IAW}} = \omega'/k$, and the damping rate of ion waves, $\gamma_{\text{IAW}} = -\omega''/\omega'$, are shown in Figure 1.1. Using the single ion approximation, we see that the phase velocity is approximately constant and the damping rate is very low. The damping rate increases linearly with the ion temperature. This can be attributed to the large ratio of the wave phase velocity to the thermal velocity of ions. For example, at $T_i/T_e = 0.3$, we have $v_{Ti}/v_{\text{IAW}} \simeq 0.2$.

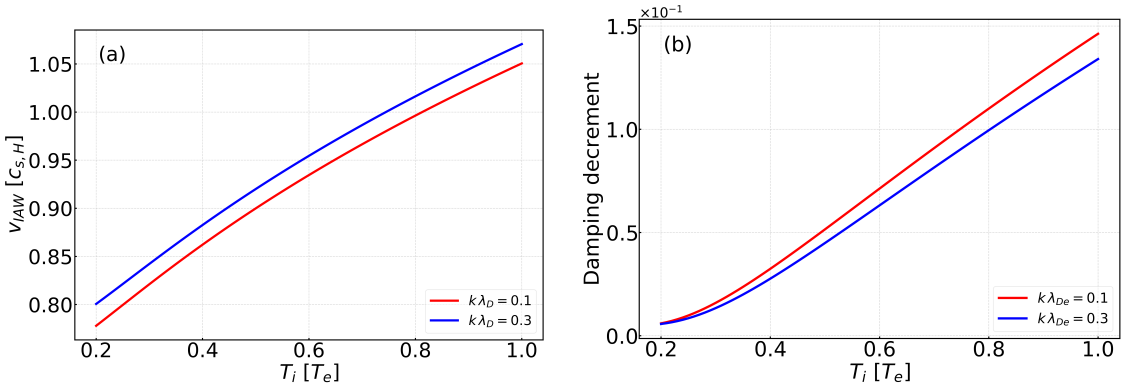


Figure 1.1: Dependence of the phase velocity, $v_{\text{IAW}} = \omega'/k$, (a) and the damping rate, $\gamma_{\text{IAW}} = -\omega''/\omega'$, (b) on the temperature ratio $T_i/T_e$ for two wavelengths, $k\lambda_{De} = 0.1$ (red) and 0.3 (blue), in a plasma with a single species. The average charge and mass of this species are $Z_{\text{eff}} = 3.5$ and $A_{\text{eff}} = 6.5$, respectively.

Approximation of an effective ion does not account for detailed ion kinetics and may

produce a significant error in evaluation of the ion acoustic damping rate and consequently the level of SBS. Ion waves in multi-species plasmas were considered in references [68], [69]. In the case of a two-component CH plasma containing fully ionized carbon ($Z_C = 6$) and hydrogen ions, equation (1.26) reads:

$$1 + (k\lambda_{De})^2 + i\sqrt{\frac{\pi}{2}\frac{m_e}{m_p}} + \frac{c_H T_e}{T_i}\left[1 + \frac{x}{\sqrt{2T_i/T_e}}\mathcal{Z}\left(\frac{x}{\sqrt{2T_i/T_e}}\right)\right] + \\ + \frac{6(1-c_H)}{T_i/T_e}\left[1 + x\sqrt{\frac{6}{T_i/T_e}}\mathcal{Z}\left(x\sqrt{\frac{6}{T_i/T_e}}\right)\right] = 0, \tag{1.30}$$

where $c_H$ and $1 - c_H$ are the hydrogen and carbon concentrations; both ion species have the same temperature $T_i$.

There are two acoustic waves in this two-ion system, fast and slow, their phase velocity and damping rate are shown in Figure 1.2. The phase velocities differ approximately two times and they increase with the ion temperature. Damping rates of both modes are higher than in the average species case because of a stronger interaction with hydrogen ions. Damping of the slow mode is almost independent on the ion temperature, while damping of increases significantly. It is larger than the slow mode damping for $T_i/T_e > 0.35$.

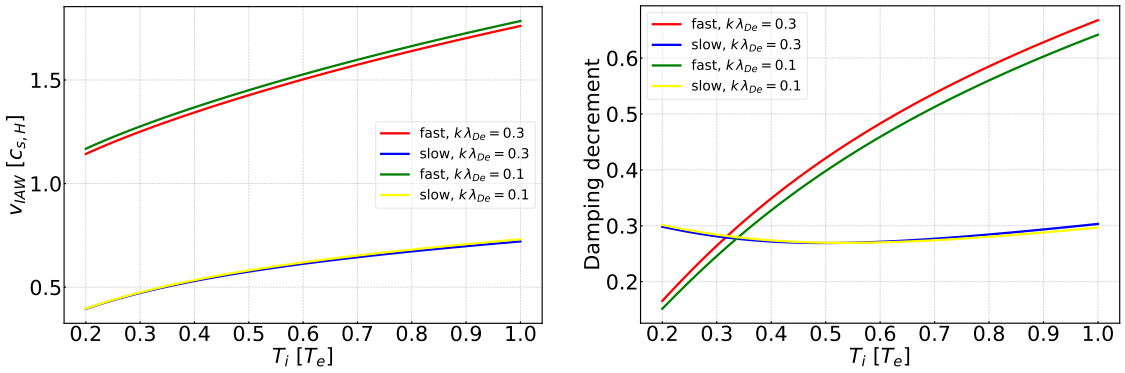


Figure 1.2: Dependence of the phase velocity, $v_{\mathrm{IAW}} = \omega'/k$, (a) and the damping rate, $\gamma_{\mathrm{IAW}} = -\omega''/\omega'$, (b) on the temperature ratio $T_i/T_e$ for two wavelengths, $k\lambda_{De} = 0.1$ (red) and 0.3 (blue), in a fully ionized CH plasma. The case of two species, hydrogen and carbon, with charges and masses $Z_{\mathrm{H}} = 1$, $A_{\mathrm{H}} = 1$, $Z_{\mathrm{C}} = 6$, $A_{\mathrm{C}} = 12$, respectively, is considered.

Moreover, in CH plasmas, there is a stronger damping of IAWs compared to single ion plasmas because of the presence of light H ions. The threshold of the parametric decay is proportional to the IAW damping rate. In the case of a high IAW damping (with H), the threshold is higher and the SBS-produced signal is lower. The fast mode, which has a smaller damping increment, can accelerate thermal ions more efficiently since its phase velocity is closer to the ion thermal velocity [67]. Consequently, the EPW amplitude can grow to higher levels, producing a stronger SRS signal and a larger number of hot

electrons, as was also confirmed experimentally [64]. These particular features will be considered in more detail in Sec. 1.3.3.

The ion-ion collisions can also contribute to the ion acoustic wave damping. Their contribution is determined by the collisionality, which is a ratio of the ion mean free path to the wavelength, denoted as $k\lambda_{\text{ii}}$. When $k\lambda_{\text{ii}}$ is small, ion collisions dominate and contribute to the wave damping through the ion viscosity [69]. Collisions between electrons and ions may also play a role, but their effect is typically small. On the other hand, when $k\lambda_{\text{ii}}$ is larger than 1, as is the case of SBS in ICF plasma, collisions are not important and Landau damping dominates.

### 1.3.3 Convective SBS: spatial gain

In an inhomogeneous plasmas, resonance conditions can be fulfilled only in one resonance point $x_{\text{res}}$, where the wavenumber detuning is zero, $\kappa(x_{\text{res}}) \equiv k_0 - k_s - k_{\text{IAW}} = 0$. The resonance conditions thus define for a specific frequency the matching wavenumber of the unstable mode and the resonance position in plasma. The wave vector mismatch $\kappa(x)$ defines the width of the resonance zone. It is influenced by the inhomogeneity of the density, characterized by the local scale length $L_n = n_e\,(dx/dn_e)$, and the inhomogeneity of expansion velocity, characterized by the local scale length $L_u = c_s\,(dx/du)$. This means that SBS is primarily sensitive to variations in ion density and ion velocity. Temperature gradients are typically much smaller, because of a high electron thermal conductivity in an underdense plasma, and can be neglected.

The plasma parameters, such as density and velocity or temperature profiles, which are shown in Figure 1.3, can be calculated using hydro codes. These profiles typically include specific points of special interest, such as the critical $n_{\text{cr}}$ and quarter critical $n_{\text{cr}}/4$ densities. A detailed description of coupling kinetic and hydrodynamic simulations in application to experiments is described in Sec. 2.1.2.

SBS is a convective instability, the amplitude of scattered wave in an inhomogeneous plasma is amplified spatially along its propagation direction near the resonant point corresponding to the perfect wave matching. The spatial growth rate for SBS reads [12], [51], [71]:

$$G_{\text{SBS}} = \frac{1}{4}\frac{k_{\text{IAW}}^2\, v_{\text{os}}^2}{v_s\,\omega_s}\int dx\,\text{Im}\frac{\chi_e\,(1+\chi_i)}{1+\chi_e+\chi_i}, \tag{1.31}$$

where the integral is taken over the resonance region, $v_s$ is the group velocity of scattered wave and $\chi_{e,i}$ is the electron/ion susceptibility (1.27) corresponding to the ion acoustic wave. The position of the resonance is defined by the frequency of the scattered wave, which for the case of backscattering reads as $\omega_0 - \omega_s = \omega_{\text{IAW}}(x_{\text{res}}) = 2k_0[c_s(x_{\text{res}}) + u(x_{\text{res}})]$. The phase velocity and damping decrement, $v_{\text{IAW}} = \omega_{\text{IAW}}/k$ and damping coefficient

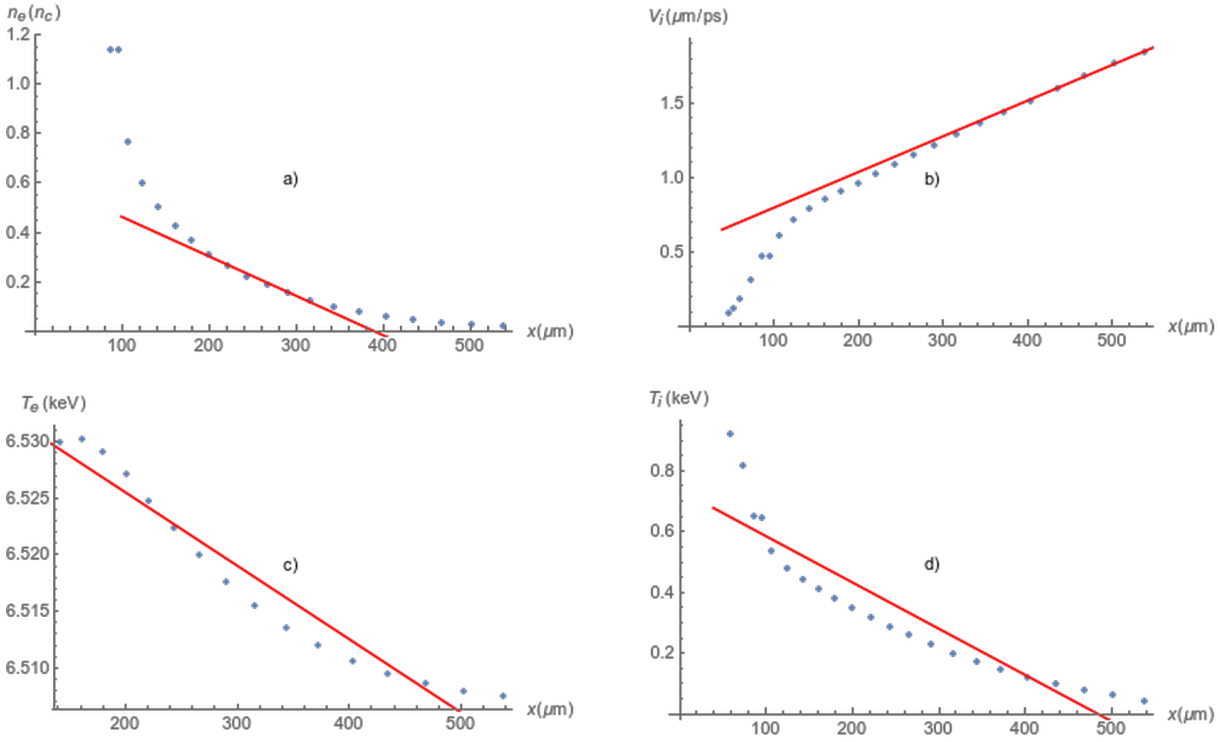


Figure 1.3: Typical profiles of density (a), ion velocity (b), electron (c) and ion (d) temperature obtained from the hydro code (dots) and their fits (red lines). Hydro simulations were conducted with the code CHIC [70] for the laser pulse of intensity $2.1 \times 10^{16}$ W/cm$^2$ and wavelength 0.35 $\mu$m interacting with a solid target made of copper.

$\gamma_{\rm IAW}$, are calculated in Sec. 1.3.2. The width of resonance region is proportional to the ion acoustic wave damping, $\Delta x_{\rm res} \simeq \gamma_{\rm IAW}/(d\omega_{\rm IAW}/dx)$. Near the resonance, Eq. (1.31) can be written as

$$G_{\rm SBS} = \frac{1}{8}\left(\frac{v_{\rm os}}{v_{\rm Te}}\right)^2 \omega_{\rm IAW}\frac{\omega_0}{c}\int dx\,{\rm Im}\frac{n_e(x)/n_{\rm cr}}{\Delta\omega(x) - i\gamma_{\rm IAW}}, \tag{1.32}$$

where $\Delta\omega(x) = \omega_0 - \omega_s = \omega_{\rm IAW}(x)$. In two limiting cases, the integral in Eq. (1.32) can be calculated analytically. If the resonance width is significantly smaller than the size of the plasma, $\Delta x_{\rm res} \ll L_n$ (we refer to it as a "weak" regime) one can take integral over the resonance and expression for the gain $G_{\rm SBS}$ has the form

$$G_{\rm SBS\,weak} = \frac{\pi}{4}\left(\frac{v_{\rm os}}{v_{\rm Te}}\right)^2 k_0 L_n. \tag{1.33}$$

In a general case where both the velocity and density gradients contribute, the gain exponent $G_{\rm SBS}$ has the form

$$G_{\rm SBS\,weak} = \frac{\pi}{4}\left(\frac{v_{\rm os}}{v_{\rm Te}}\right)^2 k_0 L_n \left(1 + 2\frac{\omega_0^2}{\omega_{\rm pe}^2}\frac{L_n}{L_u}\right)^{-1}. \tag{1.34}$$

According to this equation, the density scale length, $L_n$, is the dominant factor if it is smaller than $0.5 L_u \, n_e/n_{\rm cr}$ [12].

Conversely, if the resonance width is comparable to the size of the plasma, $\Delta x_{\rm res} \gtrsim L_n$ (we refer to it as a "strong" regime) we obtain a different expression for $G_{\rm SBS}$

$$G_{\rm SBS\,strong} = \frac{1}{8}\left(\frac{v_{\rm os}}{v_{Te}}\right)^2 \frac{\omega_{\rm IAW}}{\gamma_{\rm IAW}} \frac{\omega_0}{c} \int \frac{n_e}{n_{\rm cr}} dx, \tag{1.35}$$

Note that in Eq. (1.33) the convective gain of SBS is independent on the damping rate. This case corresponds to a local SBS amplification of each scattered frequency. In the "strong" the resonances are overlapped and all scattered waves are amplified in the whole plasma.

In the case of two ion species, there are two ion acoustic modes: the slow and fast mode as it shown in Figure 1.4b by red and blue lines. Both modes are much stronger damped due to the resonant interaction with light ions – protons. SBS amplification of each mode takes place over a large zone near the corresponding resonant point, and the gain is strongly suppressed (see Section 1.3.4). While formula (1.33) could be useful for calculating approximate values of $G_{\rm SBS}$ in the case of $\Delta x_{\rm res} \ll L_n$, the actual $\Delta x_{\rm res}$ may be comparable to the size of the plasma. In this situation, numerical integration of Eq. (1.31) is required, as it is shown in Figure 1.4b.

### 1.3.4 Example of parameters relevant to shock ignition

By substituting (1.24) into (1.23) and considering both the damping of the scattered $\gamma_s$ and ion acoustic waves $\gamma_{\rm IAW}$ (calculated in Section 1.3.2), we obtain the complete expression for the temporal growth rate $\gamma$. As demonstrated in Figure 1.4a, the SBS temporal growth rate is depicted as a function of plasma density for a set of parameters that are relevant in practical applications. This graph illustrates the dependence of the electron density, which increases linearly with the coordinate $x$ according to the relation $n_e/n_{\rm cr} = 0.05 + 0.23\, x/l_n$. The use of linear density profiles in the study of parametric instabilities such as SRS, SBS, and TPD is a common choice. The reason for this is that the instabilities that occur in ICF are resonant and local in nature. They are generated and amplified by the laser-plasma interaction, and the resulting instability growth is largely determined by the local plasma conditions, such as density and temperature. As a result, a linear approximation of the density profile (shown in Figure 1.3a) is often sufficient to capture the essential physics of the instability. It should be noted that when the ion temperature ($T_i$) is significantly smaller than the electron temperature ($T_e$), it corresponds to a reduced damping rate of IAW as it shown in Figure 1.2b, which in turn facilitates the excitation of SBS.

Here, the laser wavelength is $\lambda_0 = 0.351\,\mu$m and $l_n = 300\,\lambda_0$ is the length of the linear density profile (while corresponding density scale length is $L_n(x) = (n_e/n_{\rm cr})(l_n/0.23)$). The red, green and blue lines show the SBS growth rates in a plasma with fully ionized carbon and hydrogen ions of equal concentration, $n_C = n_H = \frac{1}{7}n_e$. The green line shows the case where two ion species are replaced by one species with an average mass $A_{\rm eff} = 6.5$ and charge $Z_{\rm eff} = 3.5$. There is a significant difference from the case where two ion species are considered separately. In the case of a single ion species, the damping of ion acoustic wave is rather small, $\gamma_{\rm IAW}/\omega_{\rm IAW} = 0.013$, and the SBS gain is quite large. In the case of two ion species, there are two ion acoustic modes: the slow and fast mode. Both modes are much stronger damped due to the resonant interaction with light ions – protons: $\gamma_{\rm IAW}/\omega_{\rm IAW} = 0.24$ for the fast mode and 0.28 for the slow mode. Consequently, SBS amplification takes place over a large zone near the resonant point, and the gain is strongly suppressed (blue and red lines).

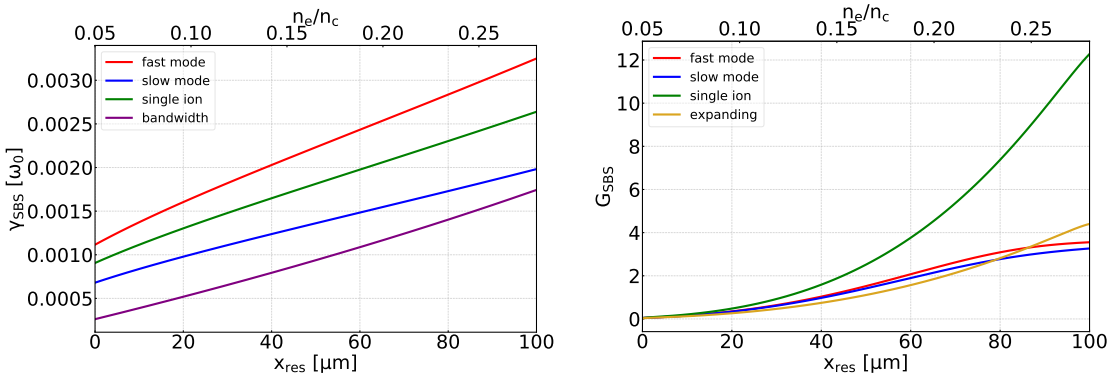


Figure 1.4: Dependence of the growth rate (a) of SBS on the resonance position and spatial gain (b) on the coordinate for the case of a plasma with inhomogeneous density profile with the length of the linear density profile $l_n = 300\,\lambda_0$ and length of the linear velocity profile $l_u = 300\,\lambda_0$. Here, the laser intensity is $6 \times 10^{15}$ W/cm$^2$, laser wavelength is 0.351 $\mu$m, electron temperature is 3.4 keV and ion temperature is 1 keV.

The purple line represents the growth rate for a phase-modulated laser pulse with a Lorentzian power spectrum with a correlation time $\tau_c = 2/\Delta\omega_0 \sim 0.5$ ps in the case of a single average ion species. The laser bandwidth $\Delta\omega_0 \simeq 4$ ps$^{-1}$ is comparable with the growth rate $\gamma_{\rm SBS} \sim 5 - 10$ ps$^{-1}$ for the monochromatic pump shown in Figure 1.4a (green line) and, according to equation (1.25), the growth rate is suppressed.

Ion acoustic wave damping has a smaller effect on the spatial SBS gain as shown in Figure 1.4b. There is practically no difference between the spatial gains for slow and fast modes, but the gain for a plasma with a single average ion species is higher. The golden line in Figure 1.4b represents the spatial gain for an inhomogeneous plasma with the ion flow velocity $u$ depending on coordinate. Here we consider a single ion model and a linear flow velocity profile, $u(x) = u_s\,(x/l_u - 1)$ where $l_u = 300\,\lambda_0$ is the length

of the linear velocity profile and $u_s = 0.75\,\mu$m/ps is approximately twice the ion sound velocity $c_s \simeq 0.47\,\mu$m/ps. In this case, the frequency of ion acoustic wave is Doppler-shifted, $\omega_{\mathrm{IAW}} = k_{\mathrm{IAW}}(c_s + u)$, and the resonance condition, $\kappa(x) = k_0 - k_s - k_{\mathrm{IAW}} \approx 0$, is fulfilled in a narrow zone depending on the density, $L_n$, and velocity, $L_u$, scale lengths. Consequently, amplification of SBS-driven waves is suppressed if the plasma expansion is considered. This can be seen by comparing the golden line in Figure 1.4b with the green line corresponding to zero flow velocity. This is the regime in which $L_n$ dominates and the characteristic velocity scale length $L_u$ is considered to be infinite.

These examples demonstrate the feasibility of controlling SBS through laser bandwidth and ion species ratio.

## 1.4 Stimulated Raman scattering

This section delves into the intricacies of the SRS process and its key features. We begin by examining the role of collisions in the development of SRS. We also explore the distinctions between convective and absolute instabilities and the impact of bandwidth on the process. The section is supplemented with recent research in the field, including the connection between SRS and the generation of hot electrons through electron plasma waves, as well as the link to Landau damping and wave breaking. Additionally, we examine the competition between SRS and SBS, and discuss the observational features that can be used to differentiate between the two.

### 1.4.1 Temporal gain: theory and experiments

In the early years of quantum mechanics, it was discovered that a molecule could scatter a photon inelastically, leading to a transition of the molecule to a higher-frequency vibrational state and a decrease in the photon's frequency by the same amount. This phenomenon, now known as Raman scattering, was first predicted by Smekal [72] in 1923 and later observed in liquids by Raman [73] and in crystals by Landsberg and Mandelstam [74] in 1928. The probability of this transition increases with the number of downshifted photons present, which leads to the formation of a coherent wave through stimulated emission. This effect, known as stimulated Raman scattering (SRS), was proposed as a potential foundation for a laser by Hellwarth [75] in 1963.

Stimulated Raman scattering is the parametric instability corresponding to a decomposition of the pump wave $\omega_0$ into a scattered electromagnetic wave $\omega_s$ and an electron plasma (Langmuir) wave $\omega_{\mathrm{EPW}}$. As the frequencies of plasma and scattered waves are comparable, SRS can be excited only in a plasma with electron density smaller than the quarter of critical density. Additionally, the plasma wave should not be suppressed by

Landau damping [76], which necessitates $k_{\mathrm{EPW}}\lambda_{\mathrm{De}} \leq 0.25$, where $\lambda_{\mathrm{De}} = v_{\mathrm{Te}}/\omega_{\mathrm{pe}}$ is the Debye length. The Landau damping becomes more restrictive as the density decreases and temperature increases, with backscattering being suppressed first as $k_{\mathrm{EPW}}$ is largest in this case. Although collisional damping can also suppress SRS, it is usually not the main suppression mechanism in direct-drive coronas. In direct-drive laser plasmas, density inhomogeneity is usually the main factor that determines SRS thresholds (Sec. 1.4.2).

Theoretical studies of the amplification growth rates and thresholds for SRS in homogeneous plasmas were conducted in the 1960s [77]–[79], but it only in the 1970s when lasers became powerful enough to allow experimental observation of SRS. In the 1970s, a significant effort was made to understand SRS in inhomogeneous plasmas through a combination of theoretical analysis and computer simulations. In inhomogeneous plasmas, the distinction between absolute and convective instabilities becomes crucial. The SRS gain for a specific pair of daughter waves is limited to a specific spatial area where the matching conditions for the decay are met. As soon as the waves move out of this region, they stop growing, leading to a finite amplification as the waves travel through the resonance area.

The three wave-matching conditions for the SRS parametric instability read:

$$(\omega_0, \mathbf{k}_0) = (\omega_s, \mathbf{k}_s) + (\omega_{\mathrm{EPW}}, \mathbf{k}_{\mathrm{EPW}}), \tag{1.36}$$

where the plasma wave $(\omega_{\mathrm{EPW}}, \mathbf{k}_{\mathrm{EPW}})$ satisfies the Bohm-Gross dispersion relation $\omega^2_{\mathrm{EPW}} = \omega^2_{\mathrm{pe}} + 3v^2_{\mathrm{Te}}k^2_{\mathrm{EPW}}$. The characteristic temporal growth rate $\gamma$ can be expressed as [55]:

$$(\gamma + \gamma_{\mathrm{EPW}})(\gamma + \gamma_s) = \gamma_0^2, \tag{1.37}$$

where $\gamma_{\mathrm{EPW}}$ and $\gamma_s$ are the amplitude damping rates of the electron-plasma and scattered light waves, respectively, and $\gamma_0$ is the growth rate in the absence of damping.

SRS is an electronic instability characterized by a high growth rate [12], [51]:

$$\gamma_0 = \frac{k_{\mathrm{EPW}}v_{\mathrm{os}}}{4}\sqrt{\frac{\omega_{\mathrm{pe}}}{\omega_0 - \omega_{\mathrm{pe}}}}, \tag{1.38}$$

where $\mathbf{k}_{\mathrm{EPW}} = \mathbf{k}_0 - \mathbf{k}_s$ is the plasma wave vector. In difference from SBS, as the frequencies of the scattered and plasma waves are comparable, SRS corresponds to a significant nonlinear laser energy deposition in plasma. Temporal growth rate $\gamma_{\mathrm{SRS}}$ is shown in Figure 1.5a. The SRS growth rate attends its maximum in a $\sim 10\,\mu$m wide region corresponding to the plasma densities $n_e/n_{\mathrm{cr}} \gtrsim 0.15$ slightly below the quarter critical density. In the lower density part of plasma, SRS is suppressed due to a strong Landau damping because the characteristic parameter $k_{\mathrm{EPW}}\lambda_{De}$ increases.

The effect of laser bandwidth in SRS in the analytical model [42] is given by $\gamma_{\mathrm{SRS}} \sim \gamma_0^2/\Delta\omega_0$ when the bandwidth $\Delta\omega_0$ is significantly larger than the linear growth rate $\gamma_0$ in the absence of bandwidth. This suggests that in order to suppress SRS a bandwidth of $\Delta\omega_0 \gtrsim \gamma_0$ is needed. For the parameters shown in Figure 1.5a, this corresponds to the bandwidth of $\Delta\omega_0/\omega_0 \sim 10^{-2}$. This criterion was confirmed with a more detailed analysis in Refs. [5], [46].

The suppression of instability by using a broadband laser was experimentally confirmed by Obenschain et al. [80]. However, the technology limitations at the time of the experiment limited the bandwidth to $\Delta\omega_0/\omega_0 = 3 \times 10^{-3}$. In 1991, Guzdar et al. conducted a study on the impact of laser bandwidth on instabilities in inhomogeneous plasmas [81]. They found that, when the homogeneous growth rate $\gamma_0$ is much smaller than the bandwidth $\Delta\omega$, the bandwidth has no effect on the convective amplification because average amplification factor is independent of bandwidth contrary to [58]. This conclusion was established both analytically and numerically. In 2001, Dodd and Umstadter [82] discovered that a linear frequency chirp with a bandwidth of 12% could eliminate Raman forward scattering in a plasma density of 1% of the critical density. In 2018, Palastro et al. [83] demonstrated that while laser bandwidth is ineffective in reducing linear resonance absorption, it is effective in suppressing nonlinear enhancement. Folett et al. conducted studies in [5], [46] to determine the thresholds of the absolute SRS and TPD instabilities using a 3D LPSE code. They calculated the scaling of these thresholds with the density scale length, temperature, and wavelength and found that while the thresholds were similar to existing analytical models, there is a quantitative difference. They also discovered that multi-beam TPD and SRS backscatter are easier to mitigate with laser bandwidth compared to single-beam instabilities.

### 1.4.2 Spatial gain and absolute SRS instability

SRS in an inhomogeneous plasma could be either convective or absolute instability. In difference from SBS, which is sensitive to the plasma density and velocity inhomogeneities, convective SRS gain depends only on the density gradient [84]–[86]. Spatial gain of SRS in the backward direction is

$$G_{\mathrm{SRS}} = \frac{\pi}{8}\frac{v_{\mathrm{os}}^2}{c^2}\frac{k_{\mathrm{EPW}}^2 L_n}{k_s}. \tag{1.39}$$

It is shown in Figure 1.5b as a function of plasma density. Convective SRS modes can develop in a wide range below the quarter critical density. When considering SRS in inhomogeneous plasmas, it is crucial to understand the difference between absolute and convective growth. In these types of plasmas, the SRS gain for a specific pair of daughter waves is only present in a specific spatial region where the conditions for decay are met.

Once the waves move out of this region, they stop growing, resulting in a finite amplification as the waves travel through the resonance region. However, there are situations where energy is transferred to the growing waves faster than they can move out of the resonant region, leading to growth that is only limited by nonlinear effects.

There is also an absolute SRS instability [46], [51], [87], which develops near the turning point of the scattered wave. Near the quarter critical density this absolute instability corresponds to scattering in the backward direction. It has a rather low threshold

$$v_{os}/c \simeq (k_0 L_n)^{-2/3}, \tag{1.40}$$

and it often dominates the interaction.

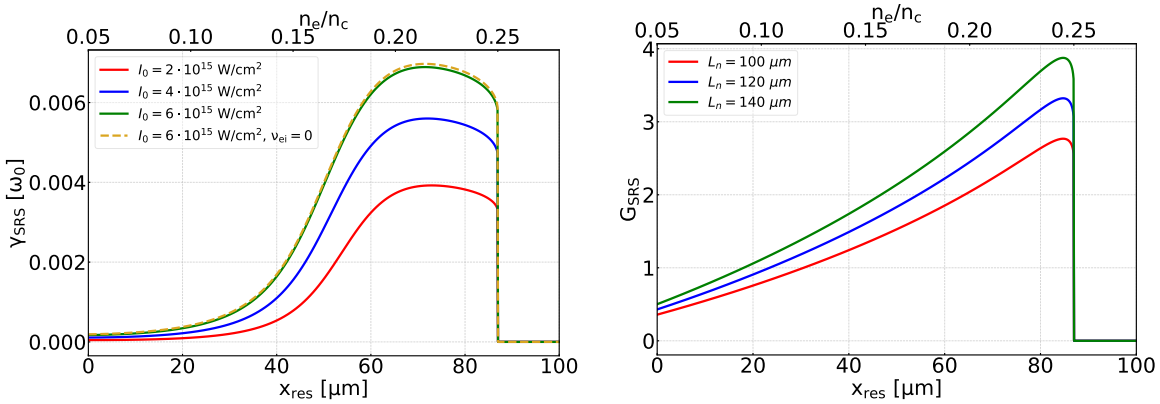


Figure 1.5: Dependence of the SRS temporal growth rate (a) and spatial gain (b) on the coordinate of the resonance point for the case of a plasma with in-homogeneous density profile. The density scale length $L_n = 300\,\lambda_0$ in case (a) and varies from 300 to $450\,\lambda_0$ in case (b). The laser intensity is $(2-6)\times 10^{15}$ W/cm$^2$ in case (a) and $6\times 10^{15}$ W/cm$^2$ in case (b). Here the laser wavelength is $0.351\,\mu$m, electron temperature is 3.4 keV and ion temperature is 1 keV.

The SRS instability could significantly contribute to the laser absorption via generation of supra-thermal electrons with energies about ten times higher than the thermal energy. They could lead to fuel preheat in the inertial confinement fusion, so their energy distribution has to be controlled.

Collisional damping may be an important issue for the SRS-driven plasma waves. The scattered light group velocity, $v_s \simeq c\,(1-\omega_{pe}^2/\omega_s^2)^{1/2}$, could be small near the corresponding critical surface, and electron-ion collisions may contribute to the plasma wave damping [88], [89]. The minimal scattered wave group velocity near the turning point is defined by the limit of applicability of the WKB approximation, that is, $k_s \gtrsim (L_n\,\lambda_{De}^2)^{-1/3}$. The WKB theory of SRS was revisited near these turning points in Refs. [51], [87]. Absorption of the scattered wave propagating from the quarter critical zone to the plasma edge reads:

$$f_{s,\text{coll.abs}} = 1 - \exp\Big[-\frac{16}{15}\frac{\nu^*_{\text{ei}}}{c}L_n\Big], \tag{1.41}$$

where $\nu^*_{\text{ei}}$ is the electron-ion collision frequency evaluated at the quarter critical density.

## 1.5 Plasma cavitation and trapping of the scattered wave

Numerical simulations described in Section 2 demonstrate that the absolute SRS instability can result in significant absorption of laser energy in plasma. This is due to the formation of density cavities near the quarter critical density, where some of the scattered wave energy is trapped and absorbed by electrons. Ponderomotive pressure causes the cavity to expand and transfer energy to ions. We estimate the efficiency of wave energy absorption in these cavities.

### 1.5.1 Electromagnetic waves in a semi-infinite plasma

We start from the analysis of the surface waves in a half-infinite space $x > 0$. The characteristics of surface waves are fundamentally determined by the properties of the plasma surface, particularly the boundary conditions required to supplement the field equations. In the case of a plasma with a well-defined surface, where the size of the region of density variation near the surface is much smaller than other plasma length scales such as the laser wavelength, Debye length and the particle's mean free path, the properties of the surface play a crucial role in determining the behavior of surface waves.

We consider a surface wave incident on an isotropic, collisionless plasma with a sharp boundary. As the unperturbed distribution function, we consider a non-relativistic Maxwell distribution function of particles of species $\alpha = e, i$:

$$f_{0,\alpha} = \frac{n_{0,\alpha}}{(2\pi m_\alpha T_\alpha)^{3/2}} \exp\left(-\frac{m_\alpha v^2}{2T_\alpha}\right). \tag{1.42}$$

Here, $n_{0,\alpha} = \text{const}$ if $x > 0$ (plasma), see Figure 1.6, and $n_{0,\alpha} = 0$ if $x < 0$ (vacuum).

We are interested in finding solutions of the kinetic equation for the distribution function $\delta f_\alpha$ perturbed by the incident electromagnetic wave:

$$\frac{\partial \delta f_\alpha}{\partial t} + (\mathbf{v}\cdot\nabla)\delta f_\alpha + \frac{e_\alpha}{m_\alpha}\mathbf{E}\frac{\partial f_{0,\alpha}}{\partial \mathbf{v}} = 0. \tag{1.43}$$

The wave has components $E_x$, $E_y$ and $B_z$ and is incident in the $x, y$ plane. Assuming the fields depend periodically on $y$ and time as $\exp(-i\omega t + ik_y y)$, we seek the solution in the

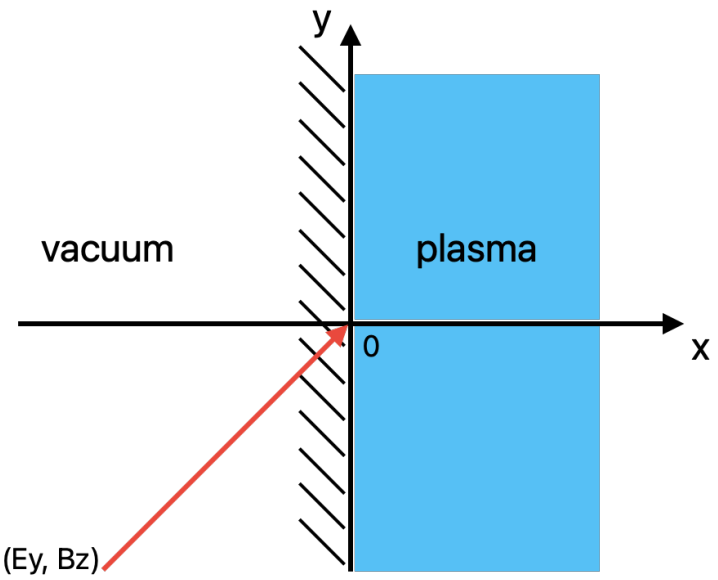


Figure 1.6: Schematic diagram of an electromagnetic wave incident on a semi-infinite plasma.

form of $\delta f_\alpha = \delta f_\alpha(x)\exp(-i\omega t + ik_y y)$. Equation for $\delta f_\alpha(x)$ reads:

$$-i\omega\delta f_\alpha + ik_y v_y \delta f_\alpha + v_x \frac{\partial \delta f_\alpha}{\partial x} + \frac{e_\alpha}{m_\alpha}\mathbf{E}\frac{\partial f_{0,\alpha}}{\partial \mathbf{v}} = 0. \tag{1.44}$$

To solve Eq. (1.44) we impose a reflective boundary condition for $\delta f_\alpha(x)$ at $x = 0$

$$\delta f_\alpha(0, v_x > 0) = \delta f_\alpha(0, v_x < 0), \tag{1.45}$$

and introduce the distribution functions $\delta f_\alpha^\pm$ for the incident and reflected particles:

$$\delta f_\alpha^\pm(x, v_x) = \begin{cases} \delta f_\alpha(x, v_x > 0), \\ \delta f_\alpha(x, v_x < 0). \end{cases} \tag{1.46}$$

The boundary condition for incoming particles is: $\delta f_\alpha^-(x \to +\infty) \to 0$. Solving then Eq. (1.44) for $\delta f_\alpha^-$ for $x > 0$ we find:

$$\delta f_\alpha^-(x, v_x) = \frac{e_\alpha}{m_\alpha v_x}\frac{\partial f_{0,\alpha}}{\partial \mathbf{v}} \int_x^{+\infty} dx'\, \mathbf{E}(x') \exp\left[i\frac{(x - x')}{v_x}(\omega - k_y v_y)\right]. \tag{1.47}$$

To find $\delta f_\alpha^+$ for $x > 0$ we use the condition $\delta f_\alpha^+(0, v_x) = \delta f_\alpha^-(0, -v_x)$ at $x = 0$:

$$\delta f_\alpha^+ = -\frac{e_\alpha}{m_\alpha v_x}\frac{\partial f_{0,\alpha}}{\partial \mathbf{v}}\left\{\int_0^x dx'\,\mathbf{E}(x')\exp\left[i\frac{(x-x')}{v_x}(\omega - k_y v_y)\right] + \right.$$
$$\left. + \int_0^{+\infty} dx'\,\mathbf{E}(x')\exp\left[i\frac{(x+x')}{v_x}(\omega - k_y v_y)\right]\right\}. \tag{1.48}$$

From now we consider the case of normal incidence, $E_x = 0$ and $k_y = 0$ and introduce a current density along the plasma surface induced by the electric field $E_y$:

$$j_y(x) = \int_0^{+\infty} dx'\,[K(|x-x'|) + K(x+x')]\,E_y(x'), \tag{1.49}$$

where

$$K(x) = -\sum_\alpha \frac{e_\alpha^2}{m_\alpha}\int_{v_x>0} d\mathbf{p}\frac{v_y}{v_x}\frac{\partial f_{0,\alpha}}{\partial v_y}\exp\left(i\omega\frac{|x|}{v_x}\right). \tag{1.50}$$

By using the Maxwell equations (1.1) we obtain a relation between the electric and magnetic field:

$$\frac{\partial E_y}{\partial x} - i\frac{\omega}{c}B_z = 0, \qquad \frac{\partial B_z}{\partial x} - i\frac{\omega}{c}E_y + \frac{4\pi}{c}j_y = 0. \tag{1.51}$$

The boundary conditions for the electric and magnetic fields $E_y$ and $B_z$ at the vacuum-plasma interface are determined by integrating Eqs. (1.51) along an infinitely narrow transition layer at $x = 0$. This implies a continuity of these fields:

$$E_y(0-) = E_y(0+), \qquad B_z(0-) = -B_z(0+). \tag{1.52}$$

Combining Eqs. (1.51) for fields with Eq. (1.49) we obtain an integral-differential equation for $E_y(x)$. To solve this complicated equation, we employ the following mathematical technique: the plasma is extended to the region $x < 0$ and the fields are extended across the boundary $x = 0$ as follows:

$$E_y(x) = E_y(-x), \qquad B_z(x) = -B_z(-x). \tag{1.53}$$

Note, that in contrary to Eq. (1.52), the magnetic field in Eq. (1.53) is discontinuous. This corresponds to a surface current $J_y(0)$ flowing along the discontinuity.

Using condition (1.53), relation (1.49) between the current $j_y(x)$ and electric field $E_y(x)$ can be extended in the entire region $-\infty \le x \le +\infty$ and written as a convolution integral:

$$j_y(x) = \int_{-\infty}^{+\infty} dx'\,\hat{\sigma}(x-x')\,E_y(x'), \tag{1.54}$$

where kernel

$$\hat{\sigma}(x) = -\sum_{\alpha} \frac{e_\alpha^2}{m_\alpha} \int d\mathbf{v}\, \frac{v_y}{v_x} \frac{\partial f_{0,\alpha}}{\partial v_y} \exp\left( i\omega \frac{|x|}{v_x} \right) \tag{1.55}$$

is the electric conductivity in coordinate representation. Its Fourier transform,

$$\sigma(\omega, k_x) = \int_{-\infty}^{+\infty} dx\, \hat{\sigma}(x)\, \mathrm{e}^{-ik_x x} = -i \sum_{\alpha} \frac{e_\alpha^2}{m_\alpha} \int d\mathbf{v}\, \frac{v_y}{\omega - k_x v_x} \frac{\partial f_{0,\alpha}}{\partial v_y}, \tag{1.56}$$

is the conductivity of an isotropic plasma.

Therefore, for a semi-infinite plasma with a specular reflection of particles from its surface, the constitutive equation

$$j_y(k_x) = \sigma(\omega, k_x)\, E_y(k_x) \tag{1.57}$$

relating the Fourier components of current density and electric field has the same form as for a spatially unlimited isotropic plasma. This is because the motion of particles in such a plasma is similar to that in an unbounded plasma, and thus the perturbation resulting from an electromagnetic field is independent of the presence of a surface. This simplification, however, is achieved by introducing discontinuity (1.53) for $B_z$ at $x = 0$. By substituting Eq. (1.54) into Eq. (1.51) and integrating over $x = 0$, this discontinuity can be verified.

However, using Eq. (1.49) with $j_y(x) = 0$ for $x < 0$ and integrating Eq. (1.51) over the transition layer near the plasma surface we obtain the continuity condition for the tangential field components $E_y$ and $B_z$ at $x = 0$ in the boundary conditions (1.52). This is expected since Eqs. (1.51) and (1.54) are only valid for $x > 0$ within the plasma region, and the continuation conditions (1.53) are used a mathematical tool for solving the integro-differential equation for the electric field $E_y$.

This equation with kernel in a form of a convolution integral is solved by applying a Fourier transform:

$$\begin{aligned} A(x) &= \int_{-\infty}^{+\infty} dk_x\, A(k_x) e^{ik_x x}, \\ A(k_x) &= \frac{1}{2\pi} \int_{-\infty}^{+\infty} dx\, A(x) e^{-ik_x x}, \end{aligned} \tag{1.58}$$

that takes into account a discontinuity of $B_z$ at $x = 0$. By performing a Fourier transform on system (1.51) and taking into account the continuity of the function $E_y(x)$ and the

discontinuity of the function $B_z(x)$ at $x = 0$, we arrive to the following set of equations:

$$\begin{aligned} k_x E_y(k_x) - \frac{\omega}{c} B_z(k_x) &= 0, \\ k_x B_z(k_x) + \frac{i}{\pi} B_z(x=0) - \frac{\omega}{c} \epsilon_t E_y(k_x) &= 0, \end{aligned} \tag{1.59}$$

where the conductivity is expressed through the transverse dielectric permittivity, $\sigma = -(i\omega/4\pi)(\epsilon_t - 1)$. According to this set of equations, the fields in plasma can be expressed via the value of magnetic field at the boundary:

$$E_y(k_x) = \frac{i\omega c}{\pi} B_z(x=0) \frac{1}{\epsilon_t \omega^2 - c^2 k_x^2}. \tag{1.60}$$

By performing the inverse Fourier transform of this expression we obtain spatial distribution of the electric field in plasma:

$$E_y(x) = \frac{i\omega c}{\pi} B_z(x=0) \int_{-\infty}^{+\infty} \frac{dk_x \, \mathrm{e}^{ik_x x}}{\epsilon_t \omega^2 - c^2 k_x^2}. \tag{1.61}$$

In particular, setting $x = 0$, we obtain a ratio of the electric and magnetic field at the boundary, which is called surface impedance:

$$\zeta(\omega) \equiv \frac{E_y(x=0)}{B_z(x=0)} = \frac{i\omega c}{\pi} \int_{-\infty}^{+\infty} \frac{dk}{\epsilon_t(\omega, k)\, \omega^2 - c^2 k^2}. \tag{1.62}$$

This relation is used in Section 1.5.2 for defining the cavity modes.

Expression for the impedance can be simplified in two limits by using an integral representation for the dielectric permittivity in a Maxwellian plasma

$$\epsilon_t(\omega, k) = 1 + \frac{\omega_{\mathrm{pe}}^2}{\omega^2} \, \xi \, \mathcal{Z}(\xi), \tag{1.63}$$

where $\xi = \omega/\sqrt{2}|k|v_{\mathrm{Te}}$ and $\mathcal{Z}$ is Fried Conte function (1.28) [63]. In the limit of a low frequency and low plasma temperature $\omega \ll \omega_{p,t}$ and $kv_{\mathrm{Te}} \ll \omega$, the dielectric permittivity is $\epsilon_t \approx 1 - \omega_{\mathrm{pe}}^2/\omega(\omega + i\nu_{\mathrm{ei}})$ and $\zeta \approx (\omega/\omega_{\mathrm{pe}})(-i + \nu_{\mathrm{ei}}/2\omega)$. Then, according to Eq. (1.61), electric field in plasma decays exponentially:

$$E_y \propto B_z(x_0) \, \exp(-\omega_{\mathrm{pe}} x/c),$$

where $c/\omega_{\mathrm{pe}} = \lambda_s$ is the collisionless skin depth.

In the opposite limit of a hot plasma and strong spatial dispersion, $kv_{\mathrm{Te}} \gg \omega$, the

dielectric permittivity reads:

$$\epsilon_t(\omega, k) = 1 + i\sqrt{\frac{\pi}{2}}\frac{\omega_{\mathrm{pe}}^2}{\omega|k|v_{\mathrm{Te}}}. \tag{1.64}$$

By introducing a dimensionless variable $\kappa = kc/\omega$ and parameter $\alpha = \sqrt{\pi/2}(\omega_{\mathrm{pe}}/\omega)^2(c/v_{\mathrm{Te}})$, the surface impedance (1.62) can be written as

$$\zeta(\omega) = -\frac{2i}{\pi}\int_0^\infty \frac{\kappa\, d\kappa}{\kappa^3 - \kappa - \alpha}. \tag{1.65}$$

It can be calculated analytically in the limit of $\alpha \gg 1$:

$$\zeta(\omega) = \frac{2}{3}\left(\frac{1}{\sqrt{3}} - i\right)\alpha^{-1/3}. \tag{1.66}$$

In this limit, electric field decays inside the plasma non-exponentially according to a power law [90], [91].

### 1.5.2 Trapped electromagnetic modes in a cavity

In this section, we investigate electromagnetic waves at normal incidence that are trapped in a cavity, which is defined as a homogeneous low density layer enclosed by sharp and dense plasma walls, as shown in Figure 1.7. The cavity is characterized by a width $\Delta x_w$, top density $n_{e,t}$, and bottom density $n_{e,b}$. The trapped modes $(E_y, B_z)$ are defined as stationary localized solutions [92] that have an oscillatory behavior inside and evanescent outside. According to Eqs. (1.51), expressions for the electric and magnetic field inside the cavity are:

$$E_y(x) = E_0\cos(kx), \qquad B_z(x) = i\frac{ck}{\omega}E_0\sin(kx), \tag{1.67}$$

where $E_0$ is a constant, $k = (\omega/c)\sqrt{\epsilon_b}$ is the wave number and $\epsilon_b = 1 - \omega_{p,b}^2/\omega^2$ is the dielectric permittivity inside the cavity. Evanescent field outside the cavity is defined by Eq. (1.61). The electric and magnetic fields at the boundaries are related by the impedance (1.62). By satisfying these boundary conditions one finds an equation for a specific set of frequencies $\omega_w$, called *eigenfrequencies* or proper modes of the cavity. The number of these frequencies depends on the depth of the well. The well has to be deep enough to enable at least one mode.

To obtain the dispersion relation defining eigenfrequencies, $\omega_w$, the impedance bound-

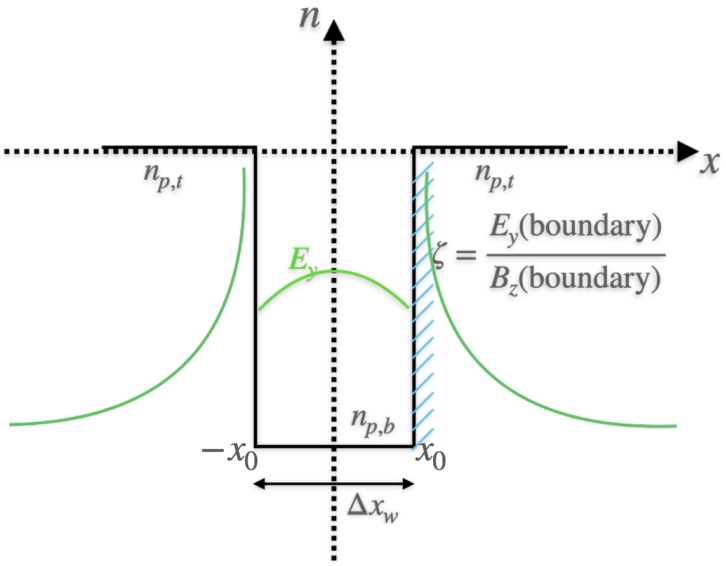


Figure 1.7: Schematic diagram of a square plasma well. Here, $n_{p,t(b)}$ is a top (bottom) plasma density, $\Delta x_w$ is a width of the well, $\zeta$ is a surface impedance and $E_y$ is a solution inside the well.

ary condition (1.62) is applied at the cavity edge at $x = x_0$:

$$\zeta(\omega) = \frac{E_y(x_0)}{B_z(x_0)} = -i\frac{\omega}{ck}\cot(kx_0). \tag{1.68}$$

Because of the field symmetry (1.67), the same boundary condition at the other cavity edge, $x = -x_0$. Then, setting $x_0 = \Delta x_w/2$, the dispersion equation reads:

$$i\zeta(\omega_w) = R(\omega_w) = (1 - \omega_{p,b}^2/\omega_w^2)^{-1/2}\cot\left[(\Delta x_w/2c)\sqrt{\omega_w^2 - \omega_{p,b}^2}\right], \tag{1.69}$$

where $\omega_{p,b}$ is the plasma frequency corresponding to the bottom well density $n_{e,b}$. The eigenmode that we are interested in corresponds to $\omega \simeq \omega_{p,t}$ because the scattered SRS light forms a cavity near the quarter critical density. Maximum absorption is achieved when the frequencies are close to each other.

The eigenfrequencies are calculated numerically for a representative set of parameters, $\Delta x_w/\lambda_0 = 7.7$ and $\omega_{p,t}/\omega_0 = 0.49$, $\omega_{b,t}/\omega_0 = 0.255$ and for electron temperatures $3 - 5$ keV. The real and imaginary parts of impedance (1.62) are shown in Figure 1.8 in function of frequency. The top plasma frequency corresponds to the quarter critical plasma density region where SRS occurs. In the temperature range of a few keV, the imaginary part of impedance dominates. Correspondingly, the trapped modes are weakly damped. The choice of parameters, $v_{\text{Te}}/c = 0.1$ and $k \simeq \pi/\Delta x_w = 0.06\omega_0/c$, in principle corresponds to a very cold case $kv_{\text{Te}}/\omega \sim 0.003$. In this case, the cold expression for $\zeta$ is valid: $\zeta = (\omega/\omega_{p,t})(-i + \nu_{ei}/2\omega)$.

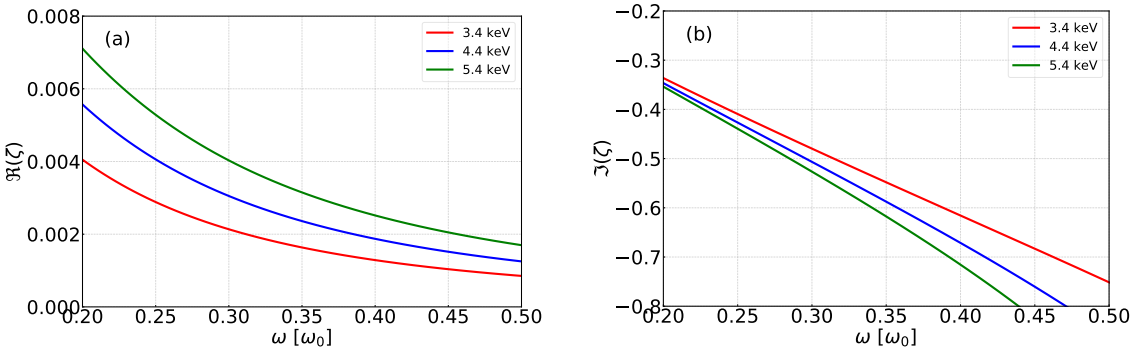


Figure 1.8: Real (a) and imaginary (b) parts of the surface impedance for a representative set of parameters: $\Delta x_w/\lambda_0 = 7.7$, $\omega_{p,t}/\omega_0 = 0.49$ and $\omega_{b,t}/\omega_0 = 0.255$ for electron temperatures $T_e = 3.4$ keV (red line), 4.4 keV (blue line) and 5.4 keV (green line).

Equation (1.69) has multiple solutions with frequencies bounded between the bottom and top plasma frequencies. The lowest frequency mode $\omega_w \gtrsim \omega_{p,b}$ is of main interest. As the real part of impedance is much smaller than the imaginary part, the real part of the lowest proper frequency $\omega_w/\omega_0 = 0.258$ can be found from equation (1.69) with only imaginary part of $\zeta$ retained,

$$-\mathrm{Im}\,\zeta(\omega_w) = R(\omega_w).$$

By using the fact that $\mathrm{Im}\,\omega_w \ll \mathrm{Re}\,\omega_w$ one can use the perturbation theory to solve the dispersion equation (1.69). Thus,

$$\zeta(\omega_w) = \mathrm{Re}\,\zeta(\omega_w) + i\mathrm{Im}\,\zeta(\omega_w) \simeq R(\mathrm{Re}\,\omega_w) + i\mathrm{Im}\,\omega_w\,\partial_\omega R(\omega_w). \tag{1.70}$$

Then, by taking the imaginary part of Eq. (1.70) one can find expression for the imaginary part of the eigenfrequency, $\mathrm{Im}\,\omega_w = \mathrm{Re}\,\zeta(\omega_w)/\partial_\omega R(\omega_w)$.

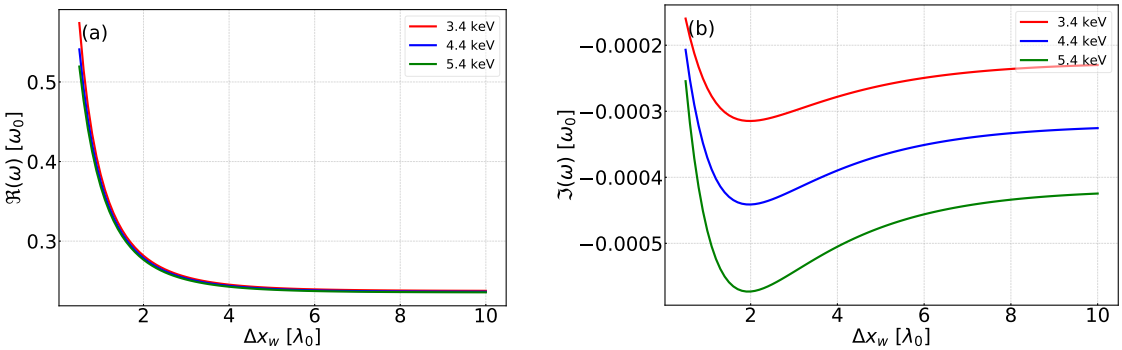


Figure 1.9: Dependence of the real (a) and imaginary (b) parts of the frequency of the trapped electromagnetic wave on the cavity width $\Delta x_w$ for electron temperature $T_e = 3.4$ keV (red line), 4.4 keV (blue line) and 5.4 keV (green line).

Dependence of the real and imaginary parts of the first proper mode $\omega_w$ on the width of the density well $\Delta x_w$ is shown in Figure 1.9. As shown in panel a, for a very narrow

well, $\Delta x_w \lesssim \lambda_0$, the mode frequency is close to the top plasma frequency $\omega_{w1} \simeq 0.5\,\omega_0$. The mode frequency is decreasing down to the bottom plasma frequency $\sim 0.2\,\omega_0$ when the well width is increasing.

Mode damping is shown in Figure 1.9b. It corresponds to the collisionless absorption in a stationary cavity due to the interaction of the wave with plasma electrons in the skin layers at both sides of the well. The damping coefficient is of the order of $-\mathrm{Im}\,\omega_w/\omega_0 \simeq (3-5)\times 10^{-4}$, and it increases with the temperature, while the real part of $\omega_w$ remains approximately unchanged.

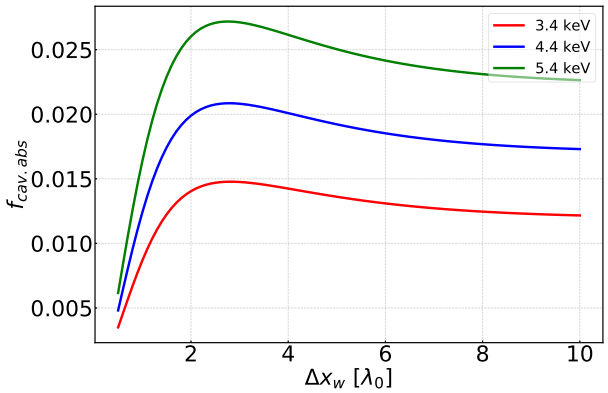


Figure 1.10: The absorption coefficient $f_{\mathrm{cav.abs}}$ dependence on the cavity width $\Delta x_w$ for electron temperature $T_e = 3.4$ keV (red line), 4.4 keV (blue line) and 5.4 keV (green line).

An increase of the well width can be qualitatively assimilated to the process of cavity formation. In the simulation presented in Section 2, after the short transient period of $3-4$ ps. A decrease of the mode frequency with time corresponds to the wave energy absorption. It is transferred to the work of cavity formation.

The absorption coefficient, averaged by a laser period, is defined as:

$$f_{\mathrm{cav.abs}} = -4\pi\,\mathrm{Im}\,\omega_w/\mathrm{Re}\,\omega_w. \tag{1.71}$$

This is shown in Figure 1.10. It is approximately constant in the range of $(6-10)\,\Delta x_w$, which corresponds to the later stage of the cavity evolution. The coefficient has a temperature dependence and tends to increase. The value of $f_{\mathrm{cav.abs}}$ is of the order of 0.1% for $\Delta x_w/\lambda_0 = 7.7$ and electron temperature of 3.4 keV.

SRS provides a flexible way for controlling the nonlinear laser absorption. The collisional and collisionless processes compete each other since the damping rate of the trapped electromagnetic wave is compatible with the collision absorption.

## 1.6 Two-plasmon decay

The TPD (two-plasmon-decay) instability was first identified by Goldman [93], who studied the Green's function for the longitudinal electric field in a laser irradiated plasma. Jackson [94] also identified it by adopting an approach based on the Vlasov equation. Galeev et al. [95] and Rosenbluth [96] argued that the collisional damping of the plasma waves produced in the decay would transfer energy to thermal electrons and provide an anomalous absorption mechanism. It was also acknowledged that the resulting electrostatic turbulence or wave breaking would lead to energetic electrons, resulting in the possibility of target preheat, which could decrease the fuel compressibility and target gain. Experimental evidence shows [97] that TPD can produce hot electrons.

From a theoretical perspective, it can be demonstrated that a linear inhomogeneity in plasma density can lead to convective instability, a result obtained by Rosenbluth [96] in 1972. This introduced a threshold known as the convective threshold, which can be higher than the collisional threshold found previously for a homogeneous plasma.

The TPD instability is a decay of a coherent electromagnetic wave into two electron plasma waves, plasmons or Langmuir waves, with a frequency of $\omega_{\mathrm{EPW}} \simeq \omega_0/2$, which are in close proximity to the local electron plasma frequency $\omega_{\mathrm{pe}}$.

The three wave-matching conditions for the TPD parametric instability read:

$$(\omega_0, \mathbf{k}_0) = (\omega_{\mathrm{EPW1}}, \mathbf{k}_{\mathrm{EPW1}}) + (\omega_{\mathrm{EPW2}}, \mathbf{k}_{\mathrm{EPW2}}). \tag{1.72}$$

The TPD instability occurs at plasma densities slightly below quarter critical, since the plasma wave $(\omega_{\mathrm{EPW},\alpha}, \mathbf{k}_{\mathrm{EPW},\alpha})$ satisfies the Bohm-Gross dispersion relation (for $\alpha = 1, 2$), $\omega^2_{\mathrm{EPW},\alpha} = \omega^2_{\mathrm{pe}} + 3v^2_{\mathrm{Te}}k^2_{\mathrm{EPW},\alpha}$.

The TPD process is similar to SRS in its physics, but with an important difference in the direction of wave propagation. Unlike SRS, where the daughter waves can propagate in the same direction, momentum conservation and coupling conditions in TPD result in the optimal excitation of plasma wave vectors lying in the plane of the pump wave polarization. The TPD instability has been studied in depth in Ref. [98] and it is characterized as a 2D process with a different k-space domain compared to SRS. The SRS plasma wave propagates in the forward direction, while the TPD waves propagate obliquely.

The growth rate of TPD instability

$$\gamma_0 = \frac{k_0 v_{\mathrm{os}}}{4} - \gamma_{\mathrm{EPW}}, \tag{1.73}$$

where $k_0 = \omega_0/c\sqrt{1 - n_e/n_{\mathrm{cr}}}$ is the laser wave vector and $\gamma_{\mathrm{EPW}}$ is the damping rate of EPW. The growth rate of TPD is comparable to that of SRS (1.38). However, the

frequencies of the TPD waves are slightly different from half of the plasma frequency. This difference is due to the momentum transfer from the plasma wave to the plasmons, where the plasma wave propagating in the direction of the pump wave has a larger wave vector and thus carries more momentum.

The threshold of the absolute TPD instability is given by

$$\frac{v_{\rm os}}{v_{\rm Te}} \simeq \left(\frac{12}{k_0 L_n}\right)^{1/2}, \tag{1.74}$$

where $L_n$ is the local density scale length at $n_{\rm cr}/4$. In inhomogeneous plasmas, the threshold for TPD is typically lower than that of SRS at $n_{\rm cr}/4$ until the plasma is quite hot.

The density range where TPD develops coincides with the plasma domain where SRS and SBS can be excited. Their mutual interaction under conditions of large scales and high temperatures is not well understood. SRS-SBS competition has been already studied with one-dimensional (1D) particle-in-cell (PIC) simulations [88]. The prime mechanism of strong suppression of SBS and efficient laser energy absorption was identified as plasma cavitation under the ponderomotive pressure of SRS-excited plasma waves. Our 1D simulations confirm the presence of a cavitation [67] process and remind us of collisionless absorption in a cavity as a method for controlling SBS-SRS competition, as discussed in previous Sec. (1.4.2).

However, the 1D geometry does not allow for the consideration of TPD. Various works have already taken into account the 2D geometry, which includes the TPD for SI conditions. These studies can be found in references such as [99].

## 1.7 Hot electron generation

The direct drive scheme of laser fusion is susceptible to the hot electron preheat. These hot electrons are produced in a long scale length near quarter-critical density plasma. The parametric instabilities, such as SRS and TPD, create electrostatic plasma waves capable of accelerating electrons. As discussed in Section 1.4, SRS can occur near and below the quarter-critical density and generate electron plasma waves propagating in the forward direction. TPD, see Section 1.6, takes place near the quarter-critical density and generates plasma waves propagating obliquely with respect to the laser wave. The energy of these plasma waves is eventually transferred to electrons that penetrate into the dense fuel and cause its premature heating.

The relationship between SRS and TPD instabilities and the generation of energetic electrons was first demonstrated in the 1970s and 1980s. The first observation of hot

electron generation caused by the TPD instability was reported in 1980 by Ebrahim et al. [100] using a $CO_2$ laser. Keck et al. [101] and Mead et al. [102] later demonstrated hot electron generation by TPD in single-beam experiments using 0.35-$\mu$m laser light.

Hot electron preheat can negatively impact target adiabat and performance in full-scale, direct-drive ignition experiments if more than 0.15% of the laser energy is transferred to the cold fuel [103]. The amount of preheat depends on several factors, including the radial displacement of the quarter-critical surface and the angular size of the cold shell. With a near-$2\pi$ angular divergence of hot electrons, it is estimated that only 25% of them will reach the cold shell and cause preheating [104].

Both SRS and TPD produce large amplitude plasma wave with high phase velocities and thus lead to energy transfer from the laser to the hot electrons. It is demonstrated theoretically [88], [105] and experimentally [27], [64] that SRS generates suprathermal electrons with energies $40-60$ keV that a stopped in the shell and can be used to drive the shell compression [106], while TPD can produce "too-hot" electrons with energies exceeding $100-200$ keV and lead to the fuel preheat. Fortunately, despite the importance of TPD, it has not been observed in experiments under the SI conditions [18], nor in our 2D simulations [65]. For this reason, in this study we focus on the SRS generated electrons.

### 1.7.1 Mechanisms of hot electron generation

To comprehend the development and outcomes of laser light coupling into electrostatic waves such as EPW and IAW, it is essential to understand how plasma electrons interact with the electron plasma waves. The energy of these waves does not escape the plasma, it is ultimately transferred to the supra-thermal electrons through linear or nonlinear damping mechanisms.

In this section, we provide a short description of three main processes responsible for the electron acceleration in the laser plasma interaction. These are: Landau damping, particle trapping, and wavebreaking. These phenomena are crucial to understanding the energy dissipation in plasmas and generation of hot, suprathermal electrons, which may penetrate deep into the dense target, preheat the fuel and thus reduce the fusion yield.

#### Landau damping

Landau damping is a phenomenon where the collective oscillations of charged particles in a plasma are damped due to the energy transfer from the wave to the particles propagating with the velocity close to the wave phase velocity. This process was first predicted by Landau in 1946 for Langmuir oscillations [76], but has since been observed in various other modes of collective plasma oscillations. Over the years, modifications have been made to

account for non-Maxwellian particle distributions, plasma inhomogeneity, magnetic fields, multiple plasma species, and nonlinear effects, making Landau damping a crucial aspect of modern plasma physics.

According to the linear theory, the damping rate of the electrostatic plasma wave (EPW) is given by:

$$\gamma_{\mathrm{EPW}} = -\sqrt{\frac{\pi}{8}} \frac{\omega_{\mathrm{pe}}^2 \omega_{\mathrm{EPW}}^2}{|k_{\mathrm{EPW}}|^3 v_{\mathrm{Te}}^3} \exp\left(-\frac{\omega_{\mathrm{EPW}}^2}{2k_{\mathrm{EPW}}^2 v_{\mathrm{Te}}^2}\right), \tag{1.75}$$

where $k_{\mathrm{EPW}}$ is the wave number of the EPW and $\omega_{\mathrm{EPW}}^2 = \omega_{\mathrm{pe}}^2 + 3k_{\mathrm{EPW}}^2 v_{\mathrm{Te}}^2$ is the frequency of the electrostatic wave.

Landau damping transforms energy of electron plasma wave into the kinetic energy of electrons. However, the rate of Landau damping decreases strongly with on the phase velocity of the EPW. The damping rate is substantial when $v_{\mathrm{ph}} = \omega_{\mathrm{EPW}}/k_{\mathrm{EPW}} \lesssim 3v_{\mathrm{Te}}$, meaning that $k_{\mathrm{EPW}}\lambda_{\mathrm{De}} \gtrsim 0.4$, so the linear interaction of electrons with a monochromatic plasma cannot lead to acceleration of a large number of electrons to large energies.

Dawson presented a clear and intuitive interpretation of Landau damping and related nonlinear effects in 1961 [107]. He explained the phenomenon as the rate of energy exchange between the wave and particles having velocity close to the wave phase velocity. Electrons are moving in the wave periodic potential and the damping time is limited by period of oscillations in the wave trough, known as the bounce time, $t_b = (m_e/eE_0k_{\mathrm{EPW}})^{1/2}$, where $E_0$ is the plasma wave amplitude.

Electrons moving with velocity as close to $v_{\mathrm{ph}}$ as $v_b = 1/k_{\mathrm{EPW}}t_b$ are trapped in the wave. They can gain in addition to their energy $\frac{1}{2}m_e v_{\mathrm{ph}}^2$ in the laboratory reference frame a trapping energy $\sim m_e v_{\mathrm{ph}} v_b$, which is relatively small. Electron resonance acceleration becomes much more efficient if there is a continuous spectrum of plasma waves in a large range of phase velocities. Such a situation can be created if a convective SRS is excited in an inhomogeneous plasma. Since the phase velocity of the daughter plasma wave increases with the plasma density and its direction is parallel to the density gradient, electrons can be accelerated successively in several plasma waves of small amplitudes with increasing phase velocities and eventually attain velocities on the order of the light velocity.

### Electron trapping in plasma wave

A large amplitude monochromatic plasma wave characterized by the bounce velocity comparable to the electron thermal velocity can itself trap a significant amount of electrons. The concept of particle trapping has motivated theoretical studies of nonlinear Bernstein-Greene-Kruskal (BGK) modes. Trapped particles lead to a reduction of Landau damping, nonlinear frequency shift, and a sideband instability.

The role of electron trapping in the long time evolution of SRS driven Langmuir waves was reported in [108], [109]. Excitation of the sideband instability causes electrons to escape from the trap with a larger velocity. Electron acceleration through trapping occurs when the wave has high enough amplitude and a large number of particles are captured in the wave potential. Trapped particles can also be released if the wave amplitude or phase is disrupted by a fast spatial or temporal perturbation resulting in a wavebreaking.

#### Wavebreaking of plasma waves

Langmuir waves driven by parametric instabilities such a SRS and TPD can grow to so large amplitudes that the bounce velocity becomes comparable to the phase velocity, $v_b \lesssim v_{\rm ph}$. Under such conditions, accelerated electrons can escape the wave taking with them a significant amount of energy and thus destroying the wave. The wave amplitude at which breaking occurs in a cold plasma was first obtained by Dawson in 1959 [110]:

$$eE_0 = m_e \omega_{\rm pe} v_{\rm ph}.$$

Coffey in 1971 [111] calculated the wavebreaking by using a waterbag distribution of electrons and a fixed background of ions, and derived an expression for the maximum amplitude of oscillations in function of the plasma temperature. As the ratio of the electron thermal velocity $v_{\rm Te}$ to the wave phase velocity increases, the maximum amplitude decreases. Schroeder et al. [112] extended the wavebreaking analysis to relativistic plasma waves in a warm plasma. Their calculation determined the maximum wave amplitude and the distribution function of trapped electrons. Wavebreaking leads to a destruction of the plasma wave and transforming plasma into a turbulent state.

### 1.7.2 Two-temperature approximation

Electron acceleration through SRS-generated plasma waves is a key process in the laser plasma interaction where a significant amount of laser energy can be transferred to a small group of supra-thermal electrons. The role of this collisionless absorption process is demonstrated in our simulations through the electron energy flux:

$$F_e = \int d\mathbf{p}\, v_x\, \varepsilon_e\, f_e(\mathbf{p}), \tag{1.76}$$

where $v_x = p_x/m_e\gamma_e$ represents the component of electron velocity in the direction of laser propagation, $\varepsilon_e = m_e c^2(\gamma_e - 1)$ is the electron kinetic energy and $\gamma_e$ is the relativistic factor. The differential electron energy flux integrated over the transverse components of electron

momentum is given by:

$$\frac{dF_e}{dp_x} = \int d\mathbf{p}_\perp \, v_x \, \varepsilon_e \, f_e(\mathbf{p}), \tag{1.77}$$

where $\mathbf{p}_\perp$ represents the components of momentum in the plane perpendicular to the $x$ axis. This function is typically calculated in the quasi-steady state of the simulation, in a dense plasma behind the quarter critical density.

Since we are interested in the energy flux into the dense plasma, it is desirable to eliminate the backward energy flux. To this end, various techniques may be employed, such as the use of absorbing boundary condition for the electrons that cross the virtual boundary in dense plasma with artificially enhanced collision frequency [88], [113], or by subtracting the backward energy flux [67].

According to the numerical simulations and experiments, the energy distribution of electrons in laser plasma interactions can often be represented by a two-temperature Maxwellian distribution: the bulk distribution $f_{e,i}$ and the hot suprathermal particles $f_h$, each of them characterized by their own densities and temperatures. Consequently, the electron differential energy flux in our simulations is represented as :

$$\frac{dF_e}{dp_x} = \sum_{j=e,h} \frac{n_j \, v_x}{\sqrt{2\pi m_e T_j}} \Big( \frac{p_x^2}{2m_e} + T_j \Big) \exp\Big( - \frac{p_x^2}{2m_e T_j} \Big), \tag{1.78}$$

where $j$ refers to either the bulk (e) or hot (h) electrons, $n_j$ is the density and $T_j$ is the temperature. The density fraction of hot electrons is defined as $n_h/n_e$.

Numerical simulations concerning the hot electron generation and transport are discussed in Section 2.5.

## 1.8 Conclusion for Chapter 1

This chapter provides a brief description of the parametric instabilities that occur in the context of ICF, including Stimulated Brillouin Scattering (SBS) and Stimulated Raman Scattering (SRS). Through an analysis of laser propagation and collisional absorption in Section 1.1, we derived Helmholtz equation for the electric and magnetic fields (1.4) and calculated the dispersion relation for electromagnetic waves (1.7). Using the WKB technique, we solved this equation and examined the collisional damping of a light wave propagating into an inhomogeneous plasma, ultimately finding the total collisional absorption coefficient (1.17).

Analysis of SBS and SRS has provided important insights into their performance in the context of shock ignition ICF. Our study of SBS in Section 1.3 reveals the crucial impact of flow velocity and laser bandwidth on its development, as well as the significance of

multiple ion species. We derived the dispersion equation for ion acoustic waves in the case of two ion species (1.30) and solved it, determining the wave phase velocities and damping rates. The results show that damping rates of both modes are higher than in the average species case due to a stronger interaction with hydrogen ions. Damping of the slow mode was found to be almost independent on ion temperature, while damping of the fast mode increases significantly with the ion temperature, see Figure 1.2. Utilizing these phase velocities and damping rates, we calculated the convective amplification factor of SBS, which is integrated numerically in the case where the width of resonance $\Delta x_{\mathrm{res}}$ is comparable to the size of the plasma. Furthermore, we provided examples of practically interesting parameters for ICF.

Our exploration of SRS examined its temporal and spatial characteristics and the role of plasma cavitation in the nonlinear laser energy absorption and hot electron generation. In particular, we develop a theoretical model describing trapping of electromagnetic waves in cavities and calculated the frequencies and damping of trapped modes and surface impedance either analytically in limiting cases or numerically by solving Eq. (1.69). We also calculated the absorption coefficient (original result). We revised mechanisms of hot electron generation, including Landau damping, particle trapping, and wavebreaking and their relationship to SRS and TPD. We noted that SRS presents the main concern in the context of shock ignition ICF.

# Chapter 2

# Numerical simulations of SBS and SRS under the shock ignition conditions

This chapter is dedicated to discussion of the use of Particle-in-Cell (PIC) simulations for studying the kinetics of plasmas. PIC codes are powerful numerical tools that are based on the Vlasov-Maxwell system of equations and are widely used for modeling collisionless and weakly collisional plasmas. They use the concept of macro-particles to capture the essential features of the plasma dynamics. In this chapter we also discuss the principle of using PIC simulations for the interpretation of experiments by using hydrodynamic simulations as an intermediary that provides input data.

## 2.1 General principles of PIC simulations

The Particle-In-Cell method was initially developed for fluid dynamics studies [114], but has since gained widespread popularity due to its advantages, including conceptual simplicity and efficient implementation on massively parallel computers. It has become a crucial simulation tool for a wide range of physics studies, such as semiconductors, cosmology, accelerator physics, and particularly plasma physics. Today, the kinetic simulation of plasmas in various settings, from laboratory to astrophysics, heavily relies on PIC codes [115].

The kinetic description of a collisionless plasma is achieved through the Vlasov-Maxwell system of equations. In this description, the various types of particles that make up the plasma are represented by their distribution functions $f_s(\mathbf{r}, \mathbf{p}, t)$ of the species $s$ with the charge $q_s$ and mass $m_s$ at the position $\mathbf{r}$ and momentum $\mathbf{p}$ in the phase-space. The

distribution function $f_s$ follows Vlasov's equation:

$$\left(\frac{\partial}{\partial t} + \frac{\mathbf{p}}{m_s\gamma_s}\cdot\frac{\partial}{\partial \mathbf{r}} + \mathbf{F_s}\cdot\frac{\partial}{\partial \mathbf{p}}\right) f_s = 0, \tag{2.1}$$

where $\gamma_s = \sqrt{1+\mathbf{p}^2/(m_s c)^2}$ is the (relativistic) Lorentz factor, $c$ is the speed of light in vacuum, and

$$\mathbf{F}_s = q_s\left(\mathbf{E} + \frac{\mathbf{v}}{c}\times\mathbf{H}\right), \tag{2.2}$$

is the Lorentz force acting on a particle $s$ with velocity $\mathbf{v} = \mathbf{p}/(m_s\gamma)$. The collective electric $\mathbf{E}(\mathbf{r},t)$ and magnetic $\mathbf{H}(\mathbf{r},t)$ fields in plasma satisfy Maxwell's equations (2.3):

$$\begin{aligned}
\nabla\cdot\mathbf{E} &= 4\pi\rho, \\
\nabla\cdot\mathbf{H} &= 0, \\
\nabla\times\mathbf{E} &= -\frac{1}{c}\frac{\partial}{\partial t}\mathbf{H}, \\
\nabla\times\mathbf{H} &= \frac{4\pi}{c}\mathbf{J} + \frac{1}{c}\frac{\partial}{\partial t}\mathbf{E}.
\end{aligned} \tag{2.3}$$

The Vlasov-Maxwell system of equations (2.1)-(2.3) describes the self-consistent dynamics of the plasma, where the constituents of the plasma are affected by the Lorentz force, and in turn, the collective electric and magnetic fields are modified by the charge and current densities of the plasma:

$$\begin{aligned}
\rho(\mathbf{r},t) &= \sum_s q_s \int d\mathbf{p}\, f_s(\mathbf{r},\mathbf{p},t), \\
\mathbf{J}(\mathbf{r},\mathbf{t}) &= \sum_s q_s \int d\mathbf{p}\,\mathbf{v}\, f_s(\mathbf{r},\mathbf{p},t),
\end{aligned} \tag{2.4}$$

One of the key features of PIC simulations is the use of quasi-particles. These are macro-particles that represent a group of real particles with similar properties, such as position, momentum, and charge. By using quasi-particles, PIC simulations are able to capture the essential features of the plasma dynamics while avoiding the need to track the motion of each individual particle.

$$f_s(\mathbf{r},\mathbf{p},t) = \sum_{\alpha=1}^{N_s}\frac{w_\alpha}{V_c}\, S\left[\mathbf{r}-\mathbf{r}_\alpha(t)\right]\,\delta\left[\mathbf{p}-\mathbf{p}_\alpha(t)\right], \tag{2.5}$$

here $w_\alpha$ is a quasi-particle weight, $\mathbf{r}_\alpha$ is its position, $\mathbf{p}_\alpha$ is its momentum, $V_c$ is the hypervolume of the cell, $S$ is the shape-function of all quasi-particles, and $\delta$ is the Dirac distribution.

Maxwell's equations are solved using the Finite Difference Time Domain (FDTD)

method and its refined algorithms. In these methods, the electromagnetic fields are discretized on a staggered grid, known as the Yee-grid, which allows for spatial centering of the curl operators in Maxwell's equations. The time-derivative in Maxwell's equations is time-centered by defining electric fields at integer time-steps ($n$) and magnetic fields at half-integer time-steps ($n + 1/2$). Magnetic fields are time-centered for diagnostic purposes and computing the Lorentz force on quasi-particles. A leap-frog scheme is used to update particle positions and velocities, which are defined at integer ($n$) and half-integer ($n - 1/2$) time-steps, respectively.

After all the particles in the simulation domain have been created, the total charge density $\rho(t = 0, \mathbf{r})$ and current densities $\mathbf{J}(t = 0, \mathbf{r})$ are calculated on the grid using a straightforward projection method:

$$\rho(t = 0, \mathbf{r}) = \sum_{\alpha,\, s} \frac{q_s w_\alpha}{V_c} S[\mathbf{r} - \mathbf{r}_\alpha(t = 0)]. \tag{2.6}$$

Next, the initial electric fields are determined by solving Poisson's equation. This is done by using the conjugate gradient method. This iterative technique is advantageous as it can be efficiently implemented on parallel computing systems and mainly involves exchanging information between neighboring processes.

At the end of the initialization stage, all quasi-particles in the simulation domain have been loaded, and the electromagnetic fields have been calculated throughout the simulation grid. The PIC loop then begins, comprising many time steps. Each time-step consists of four stages:

1. Interpolating the electromagnetic fields to the particle positions.
2. Calculating the new particle velocities and positions.
3. Projecting the updated charge and current densities onto the grid.
4. Computing the new electromagnetic fields on the grid.

PIC codes are widely used in the simulation of plasma physics, as they provide a powerful tool to study the behavior of charged particles in electromagnetic fields. However, like any simulation method, PIC codes have both advantages and disadvantages.

Advantages of PIC codes:

- **High-Fidelity**: PIC codes provide a high-fidelity representation of the plasma, capturing the collective behavior of the charged particles and their interactions with the electromagnetic fields;
- **Versatility**: PIC codes can be applied to a wide range of plasma systems and configurations, making it a multi-purpose simulation tool;
- **Scalability**: PIC codes can be run on parallel computing architectures, making it possible to run large-scale simulations and analyze complex systems.

Disadvantages of PIC codes:

- **Computational cost**: PIC codes require large computational resources, making it difficult to run large-scale simulations with fine spatial and temporal resolutions;
- **Numerical noise**: PIC codes can introduce numerical noise into the simulation results, especially in regions with low particle density. This may penalize the studies of excitation of instabilities and particle acceleration;
- **Limited time-step**: PIC codes are limited by the stability (CFL) condition, which restricts the maximum time-step that can be taken, making it difficult to simulate systems with short temporal scales.

### 2.1.1 Simulation of plasma dynamics with a code SMILEI

SMILEI is an open-source, multi-purpose PIC code for plasma simulations, offering physicists a high-performance and user-friendly tool [116]. The development of SMILEI was driven by advancements in the ultra-high intensity (UHI) laser technology and new initiatives to construct multi-petawatt laser facilities, in particular ELI pillars. UHI laser-plasma interaction is used to study matter under extreme temperature and pressure, leading to potential applications such as charged-particle acceleration, ultra-bright short-duration light sources, and electron-positron pair production.

The code is written in C++ and includes various options for geometries, laser/plasma profiles, Maxwell solvers, particle pushers, interpolators, projectors, advanced boundary conditions and more. The input is written in PYTHON and includes run-time diagnostics and post-processing tools. SMILEI is designed for high-performance on parallel supercomputers, with a hybrid MPI/OpenMP parallelization and SIMD vectorization, and has been tested on several architectures including Intel Cascadelake and Fujitsu A64FX. The code uses the Yee mesh method and a charge-conservation scheme for Maxwell's equation solving and charge deposition. SMILEI includes additional physics modules such as field ionization, binary collisions, and QED processes and is used in a wide range of applications, including laser-plasma interaction and astrophysics.

The PIC method has been designed originally to simulate the self-consistent evolution of a collisionless plasma by solving the coupled system of Vlasov-Maxwell equations (2.1)-(2.3). However, modern PIC codes incorporate additional modules to account for various kinetic processes including collisions. In the code SMILEI, the relativistic collisions have been implemented using a scheme based on Nanbu's approach [117], with improvements such as the ability to handle relativistic particles, a correction for low-temperature collision rates, and a variable Coulomb logarithm [118].

Collisions play a crucial role in PIC simulations of plasmas. They are important for achieving thermal equilibrium between ions and electrons, which is necessary for accu-

rately modeling the plasma's temperature. Additionally, ion-ion collisions are crucial for achieving thermal equilibrium within the ion population, particularly in the case of foam plasmas as discussed in Section 4. Collisions are also important for understanding the damping of plasma waves, which is discussed in Section 1.4.2. This is crucial for understanding the processes of growth and decay of SRS-driven waves and for understanding nonlinear absorption processes.

### 2.1.2 Coupling hydrodynamic and PIC simulations for interpretation of experiments

PIC codes provide a detailed information of the particle dynamics in the phase space, but their application is limited to relatively small plasma volumes and relatively short time intervals corresponding to hundreds of microns and tens of picoseconds. These scales are significantly smaller than the realistic plasmas produced in the laser interaction with solid or gaseous materials. Large plasmas are described with hydrodynamic codes using simplifying approximations about the particle distribution in the phase space. The PIC codes are used for obtaining a more detailed information about kinetic processes taking place within limited volumes and time intervals. In this section we describe the principles of coupling kinetic and hydrodynamic simulations and experiments by taking as example the hydrodynamic code CHIC [70].

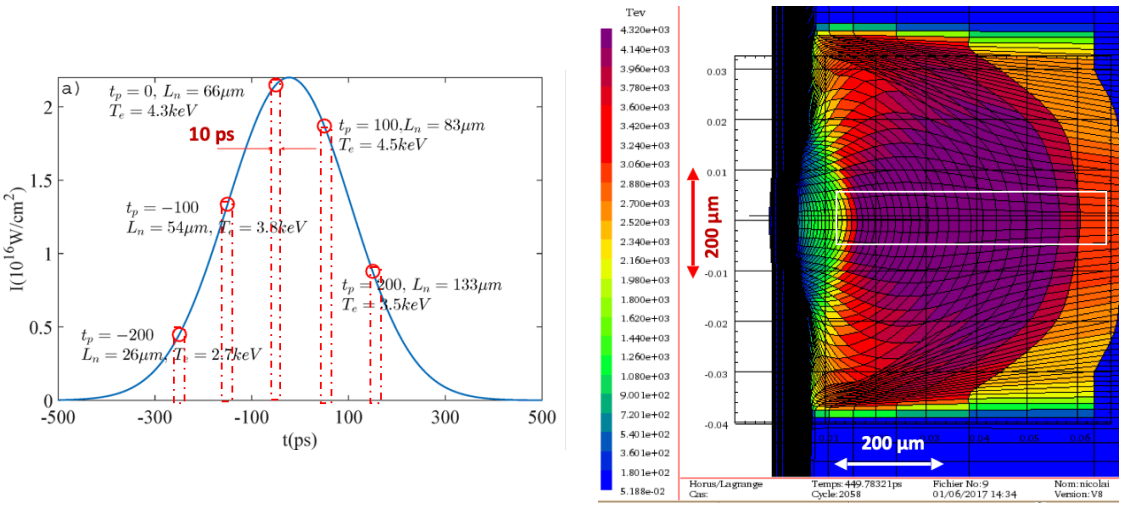


Figure 2.1: a) Laser pulse shape and the selected representative points for the kinetic simulations, b) 2D plot of density and temperature obtained from the CHIC code showing the volume chosen for kinetic simulations.

The radiation hydrodynamic code CHIC [70] is widely used for simulating laser-plasma experiments. It can model large-scale hydrodynamic behavior of the plasma over the time scales of a few nanoseconds or more. The code includes two-dimensional axially symmetric

hydrodynamics, ion and electron heat conduction, thermal coupling of electrons and ions, and detailed radiation transport. The laser propagation is described using the paraxial complex geometrical optics approximation, and it includes simplified models for resonance absorption and hot electron generation due to the TPD and SRS. However, these models have been tested only at low laser irradiances and short wavelength lasers; they may not be adequate for the conditions of shock ignition studied in this thesis. The nonlinear absorption, reflection and hot electron generation are added in hydro simulations with simplified *ad hoc* formulations deduced from detailed kinetic simulations.

Nonlinear laser plasma interactions are described with PIC simulations on a time interval of a few picoseconds and on a spatial scale of a few hundred microns with initial conditions calculated with the hydro code. These initial conditions include the profiles of plasma density $n_e$, electron and ion temperatures $T_{e,i}$ and plasma flow velocity $u$. Examples of the profiles are shown in Figure 1.3. These profiles can be taken at different time moments of laser pulse in order to evaluate the contribution of nonlinear and kinetic effect. The choice of time points is shown in Figure 2.1 where the continuous line represents the laser pulse temporal profile. Duration of the PIC simulation is defined by the time needed for nonlinear processes to develop and to attain a quasi-stationary state. For the case of our interest, SRS and SBS, the characteristic time is in the range of $5 - 10$ ps.

The spatial domain for the PIC simulation is chosen to cover the plasma volume where these nonlinear processes can develop. The PIC simulation provides detailed information on nonlinear absorption processes, such as the absorption coefficient, nonlinear reflectivity, spectrum of scattered waves and the number and energy of hot electrons. This information can be used to improve the accuracy of the interaction model introduced in the hydro codes, and can also be compared with the experimental data for validation.

A similar approach is used in the second part of the our study described in Chapter 3, which is dedicated to the laser interaction with foams. A multi-scale model of laser pulse absorption in porous materials is developed and realized in the arbitrary Lagrangian-Eulerian hydro-code PALE [119] and Eulerian code FLASH [120], [121]:

- **micro-scale**: expansion of solid elements in a pore is described in 1D model according to the cell characteristics supplied by the 2D macroscopic model;
- **macro-scale**: the plasma homogenization in the ionization front is controlled by the microscopic dynamics.

This approach shown schematically in Figure 2.2 combines a large-scale hydrodynamic description of homogenized cells with a more detailed sub-grid representation of the cells undergoing homogenization. The micro-scale model describing the cell homogenization is governed by several empirical parameters, which are determined through a comparison with kinetic simulations of laser interaction with a single pore and with experiments of

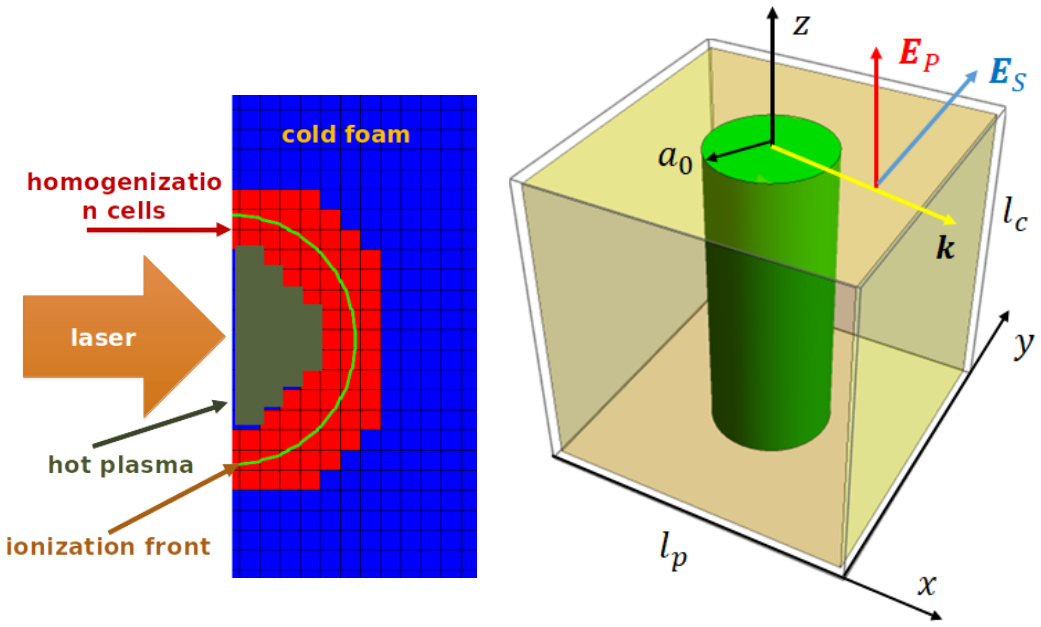


Figure 2.2: Multi-scale modeling of micro-structured targets (left), scheme of laser interaction with a single cell (right).

laser interaction with foam targets. The multi-scale model is described in Ref. [122] and results are compared with several experiments showing good agreement in terms of plasma parameters and the speed propagation of the ionization front.

## 2.2 Setup of numerical simulations of SBS and SRS

In order to evaluate the SBS-SRS competition and its role in the efficiency of laser energy absorption under the shock ignition conditions, we consider six representative cases:

i) the reference case of the interaction of a monochromatic laser pulse with a collisionless plasma with zero fluid velocity and a single ion species having effective charge $Z_{\text{eff}} = 3.5$ and mass $A_{\text{eff}} = 6.5$ corresponding to the equimolar mixture of hydrogen and carbon;

ii) the reference case is repeated with the electron-ion collisions switched on;

iii) the same as case i) but with expanding plasma with a fluid velocity linearly increasing with the coordinate, $u(x) = u_s(x/l_u - 1)$, with $l_u = 300\lambda_0$ and $u_s = 0.75\,\mu$m/ps;

iv) the case iii) of expanding plasma is repeated with the electron-ion collisions switched on.

v) the same as case i) but with two ion species, fully ionized carbon and hydrogen of equal concentrations;

vi) the same as the reference case i) but with a phase-modulated laser pulse with a correlation time $\tau_c \sim 0.5$ ps.

To further analyze the results, we also investigate the spatial and temporal evolution of the laser intensity, electron and ion density, temperature and particle velocity distributions. Additionally, we compare the growth rates and spatial gains of SBS and SRS in each case, which are presented in Sections 1.3.4 and 1.4.2. The results are presented in a series of figures and tables for easy comparison and discussion. Overall, the first part of this study aims to provide a comprehensive understanding of the role of SBS-SRS competition in laser energy absorption and the influence of various plasma parameters on this process.

### 2.2.1 Input parameters

In order to demonstrate the possibilities of controlling nonlinear laser energy absorption, we consider the interaction of an intense laser pulse incident normally on an expanding underdense inhomogeneous plasma made of a plastic (CH) with parameters relevant to the shock ignition scenario [18], [25]. Plasma has a linear density profile, $n_e/n_{\rm cr} = 0.05 + 0.23\, x/l_n$, increasing from 0.05 to 0.28 $n_{\rm cr}$ over a length $l_n = 286\,\lambda_0$ for the laser wavelength $\lambda_0 = 0.351\,\mu$m. The initial electron temperature, $T_e = 3.4$ keV, and ion temperature, $T_i = 1.0$ keV, are assumed to be homogeneous in space. These are representative values reported in numerical simulations and experiments [18], [65] and shown in Figure 1.3. The laser pulse intensity, $I_0 = \frac{1}{2}c\epsilon_0 E_0^2 = 6 \times 10^{15}$ W/cm$^2$, is maintained constant during the simulation time of 8 ps, that is, about $10^4$ laser periods, after a linear ramp during first ten laser periods. This time is sufficient for achieving a quasi-steady state in the simulation.

The simulation box length is $314\,\lambda_0$ with $14\,\lambda_0$ vacuum margins at the front and rear sides of the box in order to enable a free plasma expansion. Boundary conditions are open for electromagnetic waves, the particles reaching front and rear boundaries are re-injected with a Maxwellian distribution corresponding to the initial temperature. These boundary conditions, however, do not describe ejection of hot electrons into a dense plasma as it happens in the experiment. Instead, we evaluate the distribution of the energy flux carried by electrons and ions in the denser plasma near the right boundary.

In the following sections we analyse the particle energy evolution, spectra of scattered light and hot electron generation. The bulk temperature of species $j = e, i$ at the position $x$ is defined via the distribution function $f_j$:

$$T_{e,i} = \frac{2}{3n_{e,i}} \int d\mathbf{p}\, \varepsilon f_{e,i}(\mathbf{p}, x, t). \tag{2.7}$$

The distribution functions obtained from simulations are fitted by a sum of two Maxwellian functions (1.42) corresponding to the bulk and hot particles. For example, the electron

distribution function is approximated as:

$$f_e(\mathbf{p}) = \sum_{j=e,h} \frac{n_j}{\sqrt{2\pi m_e T_j}} \exp\Big(-\frac{\mathbf{p}^2}{2m_e T_j}\Big), \tag{2.8}$$

While analysing temporal evolution of the distribution functions of electrons and ions in the simulations, we define effective temperatures averaged over the length of simulation box as shown in Figure 2.3. In addition, we approximate the distribution functions of electrons and ions with two Maxwellian functions with different densities and temperatures as described in Section 1.7.2, and evaluate the energy flux carried with hot electrons according to Eq. (1.78).

## 2.3 Role of SBS in the particle energy evolution

In the absence of collisional damping, which can be a minor effect under the conditions of interest, the energy transfer between the laser and the particles is mediated by electrostatic fields. In the case of SRS, the laser energy is transferred to an electron plasma wave, which then transfers it to electrons. In addition, in the case of cavitation, the scattered electromagnetic wave is trapped and transfers a part of its energy to ions. The energy transfer in the case of SBS is weaker because of the smallness of the ion acoustic wave frequency, but then, ion acoustic wave transfers its energy directly to ions.

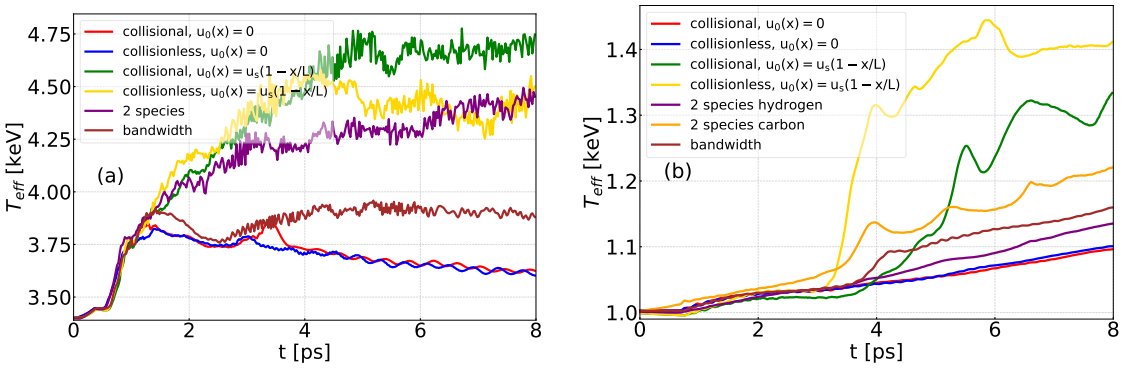


Figure 2.3: Temporal evolution of the space averaged bulk temperature of electrons (a) and ions (b) in the runs described in the legend. Parameters are given in Section 2.2.1.

The particle energy starts evolving at $t = 0.7$ ps when the laser pulse enters the plasma. The first fast increase of electron temperature, same in all simulations in Figure 2.3a, is related to the excitation of SRS near the quarter critical density. After that, two different evolution paths are observed. In the reference case of a single species plasma with zero velocity, the electron temperature gradually decreases independently on the presence (red) or absence (blue) of electron collisions. A comparison of the collisional and collisionless

runs confirms the minor role played by collisions in the reference case. By contrast, the ion temperature shown in Figure 2.3b increases at a later time of $\sim 3.5$ ps when the SBS instability is excited.

In the cases i) and ii) of a plasma with zero velocity shown in Figure 2.3 with red (collisional case) and blue (collisionless case), SBS dominates the interaction. After a short delay of $\sim 3$ ps a strong backscattering prevents the laser radiation to penetrate to the quarter critical density where SRS can be excited. Consequently, SRS is suppressed and electron temperature decreases. A small peak in the electron temperature near $t = 3.5$ ps is explained by the collisional absorption of SRS reflected light excited near the quarter critical density. As shown in Table 2.1, only about 2% of laser energy is absorbed in the reference case i) and distributed between electrons and ions. The level of SBS reflectivity is very high, about 93% at the late stage of interaction ($t > 5$ ps).

| # | Simulation | Reflected | Transmitted | Absorbed |
|---|---|---|---|---|
| i) | Reference, collisionless plasma | 91% | 4% | 5% |
| ii) | Reference, collisional plasma | 88% | 10% | 2% |
| iii) | Expanding collisionless plasma | 36% | 37% | 27% |
| iv) | Expanding collisional plasma | 37% | 27% | 36% |
| v) | Two ion species, collisionless | 36% | 30% | 34% |
| vi) | Phase-modulated pump, collisionless | 81% | 16% | 3% |

Table 2.1: Averaged values of reflected and transmitted light for the last 4 ps of simulation time for the six considered cases.

In the cases iii) and iv) of expanding plasma shown in Figure 2.3 with green (collisional case) and gold (collisionless case) lines, electron and ion temperatures are increasing to higher levels, thus demonstrating a much better laser absorption. As discussed in Section 1.3.3, divergence of the plasma velocity suppresses SBS as the amplification length of the scattered wave is shorter. Consequently, laser absorption is dominated by SRS near the quarter of critical density and plasma cavitation. Similar effect has been already observed by Klimo et al. [88]. In our case about 9% of laser energy is absorbed and deposited into electrons and ions. The electron energy rises to 4.5 keV during first $4 - 5$ ps and then remains approximately constant when the interaction enters in a quasi-stationary regime.

The role of electron collisions is more important in the expanding plasma. Switching the collisions on results in the increase of the average electron temperature from 4.5 to 4.7 keV (Figure 2.3a), which corresponds to a difference of more than 20% compared to the total temperature increment $\sim 1$ keV with respect to the initial temperature of 3.5 keV. By contrast, collisions have an opposite effect on the average ion temperature. It increases by 40% in the collisionless case but only by 30% in the collisional case. Explanation of the effect of collisions on particle heating is given in the next section.

In the case v) of two ion species shown in Figure 2.3 with a purple line, the increase of electron temperature is similar to in the case of expanding plasma without collisions. The improved laser absorption in this case is also explained by the SBS suppression, but it is related in this case to a stronger ion acoustic damping on light (hydrogen) ions. The level of SBS reflectivity in this case is 36%. Consequently, less laser radiation penetrates to the quarter critical density and produces a stronger electron heating. The effect of hydrogen ions on SRS saturation and hot electron production was reported in several experiments [64], [123], [124].

The case vi) of a phase-modulated laser pulse shows a smaller increase of electron and ion temperatures compared to the cases iii) and v). This particle heating is also explained by a partial SBS suppression related to spectral bandwidth of the laser driver. However, the considered pump correlation time of 0.5 ps is of the same order as the SBS growth time $1/\gamma_{\mathrm{SBS}}$ as described in Section 1.3.1. Consequently, the laser bandwidth is not sufficient for a strong suppression of SBS and the level of SBS reflectivity in this case is maintained on a high level of 81%. The energy partition in Table 2.1 shows that laser energy absorption in plasma increases significantly when SBS is suppressed.

## 2.4 Laser backscattering and transmission

The reflection of incident laser light and the roles of SRS and SBS are confirmed through analysis of the reflected light spectrum in Figure 2.4a. In simulation cases i) and vi), the peak near the laser frequency dominates the spectrum. This peak is downshifted by $\Delta\omega_{\mathrm{IAW}} \simeq 0.0028\,\omega_0$, which corresponds to the frequency of a driven ion wave $\omega_{\mathrm{IAW}} = 2k_0c_s$. In simulation case v), the downshift in the spectrum $\Delta\omega_{\mathrm{IAW}} \simeq 0.0032\,\omega_0$ matches the excitation of the fast wave as described in Section 1.3.2.

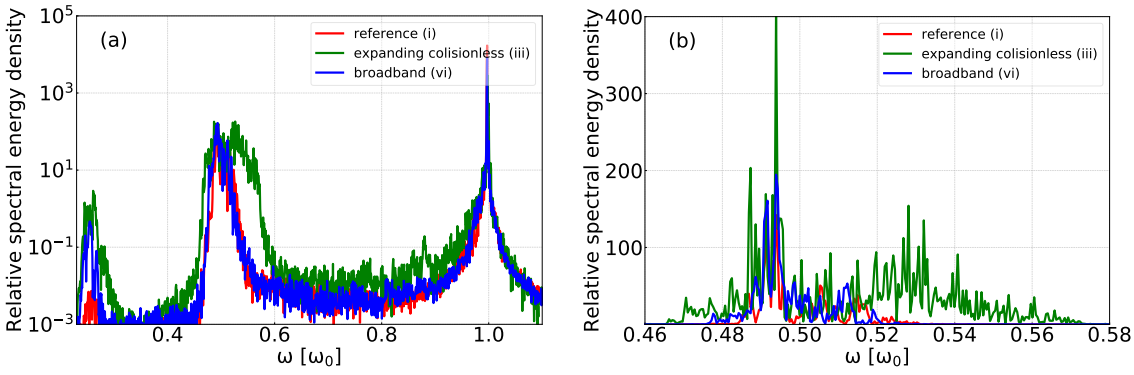


Figure 2.4: Overall view (a) and a detailed structure (b) of the spectrum of the light reflected from the plasma for the reference case (i, red), expanding collisionless (iii, green) and broadband (vi, blue) cases.

A particular feature of SRS spectrum shown in Figure 2.4 is that it extends to the frequencies smaller than $0.5\,\omega_0$. It contains several spectral components but the strongest one is downshifted by $\Delta\omega_s = \omega_s - \omega_0/2 \approx -0.01\,\omega_0$. This shift was predicted theoretically in Ref. [87]. It is explained by thermal electron motion, which leads to effective increase of the plasma wave frequency and to a correspondent decrease of the scattered wave frequency. According to equation (56) in Ref. [87], expression for the frequency shift of the scattered wave reads:

$$\frac{\Delta\omega_s}{\omega_0} = \frac{\omega_s - \omega_0/2}{\omega_0} \simeq -\frac{9T_e}{8m_ec^2} + \frac{1}{4k_0L_n(v_{os}/c)^{1/2}}. \tag{2.9}$$

The first term in the right hand side of this equation is negative and it is on the order of 0.01 under our conditions, which agrees very well with the observed shift. The second term is much smaller, it is on the order of 0.001. A similar negative shift was observed in several other publications [65], [105], but its origin was not explained.

An additional peak in left side of the spectrum shown in Figure 2.4a near the quarter of the laser frequency is attributed to the secondary SRS process, which is excited by the backscattered SRS daughter wave near the one-sixteenth of the critical density. Such effect was already reported in the previous publication [88] and manifested itself in formation of secondary density cavities at $n_e/n_{cr} \simeq 1/16$. This feature is stronger in the cases iii) and vi) where the SBS suppressed and the amplitude of the backscattered SRS wave is enhanced.

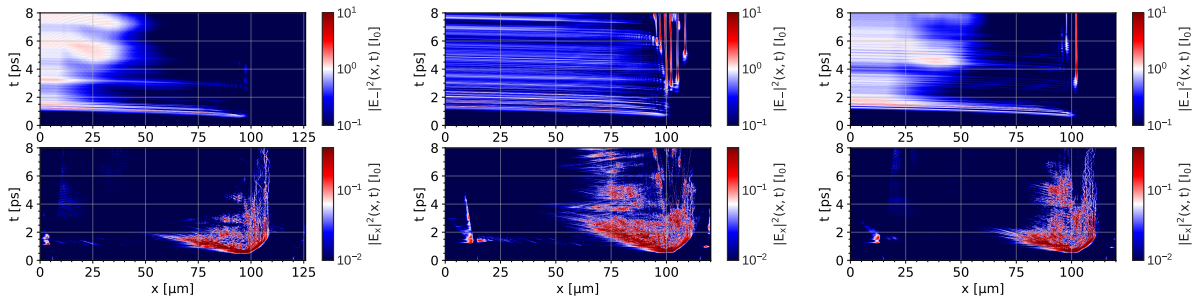


Figure 2.5: Spatial and temporal evolution of the backscattered light (top row) and electrostatic field $E_x$ (bottom row) for the reference case (i, left column), expanding collisionless plasma (iii, central column) and broadband laser pulse (vi, right column).

Both SBS and SRS contribute to the backscattered signal. Their contributions can be distinguished in the spatio-temporal plots in Figure 2.5. Excitation of Raman scattered electromagnetic waves, shown in the top row plots, is correlated with the excitation of large amplitude plasma waves shown in the bottom row. Dynamics of the Raman scattered electromagnetic wave is rather different in the three cases presented in this figure: in the left and right columns corresponding to cases i) and vi), the SBS reflectivity is high, which

leads to the inhibition of SRS near the quarter critical density and to suppression of the cavitation process. By contrast, in the central column corresponding to case iii) SBS is suppressed resulting in a stronger SRS and cavitation.

The first short SRS burst comes from the region near the quarter critical density at $t \sim 0.7$ ps. The SRS instability develops very fast, the Langmuir waves are excited in a region near the point $x \simeq 100\,\mu$m, corresponding to $n_e/n_{\rm cr} = 0.23 - 0.25$, where temporal and spatial gains plotted in Figure 1.5 are maximized. At this time, reflected SRS wave is strong enough to excite secondary SRS near the plasma density of $n_{\rm cr}/16$ at $x \approx 12\,\mu$m manifested by short-lived bursts of plasma waves. This, however, has a very weak effect on the laser reflection and absorption. A steady excitation of SRS is produced later in time $t > 4$ ps in the cases iii) and vi), and it is manifested by formation of cavities – narrow localized packets of electromagnetic field trapped in deep density depressions. There is practically no electrostatic field in the cavities because the electrons are expelled. Formation of plasma cavities near the quarter and one-sixteenths of the critical density due to Raman backscattering was reported by Klimo et al. [88].

In the case i) (left column in Figure 2.5), the SRS instability is excited near the quarter critical density only at the transient stage. It produces one or two bursts of scattered light with frequency $\sim 0.5\,\omega_0$ as shown in Figure 2.4a, which could be partially absorbed via collisional damping while propagating through the plasma. Later in time, for $t > 4$ ps, the scattered light originates from a plasma with density less than $0.1 n_{\rm cr}$, and it is due to SBS. Similar effect is observed in the case vi) of a broadband laser pulse (right column in Figure 2.5). However, here SBS is partially suppressed and the absolute SRS excited at later time, $t > 4$ ps, which is manifested in formation of two cavities and stronger backscattering in Figure 2.4.

By contrast, SBS is much stronger suppressed in the case iii) of expanding plasma, which is shown in the central column in Figure 2.5. Here, in addition to the absolute SRS, excited near the quarter critical density and produced multiple cavities, a convective SRS is excited in a lower density plasma. The latter is manifested by excitation of Langmuir waves in a plasma with density $\gtrsim 0.15\, n_{\rm cr}$ and a broad spectrum of backscattered waves in Figure 2.4.

Formation of cavities is considered in Section 1.5. It is related to the fact that the group velocity of the scattered electromagnetic wave near the quarter critical density is close to zero and thereby it stays a relatively long time in the resonance with the pump wave [51], [87]. Consequently, a strong ponderomotive force produced by the daughter electromagnetic and plasma waves induces a density depression where they are self-trapped. The plasma wave disappears when electrons are expelled from the cavity, while electromagnetic waves are weakly damped and persist for a long time. Ions are accelerated under the

ponderomotive pressure of trapped light as discussed in Section 2.6. The cavity formation is manifested by a strong reduction of backscattering level to $\sim 25\%$.

In the Section 1.5, the mode damping is discussed in detail. It is attributed to the interaction of the wave with plasma electrons in the skin layers at both sides of the well, which is known as collisionless absorption. The damping coefficient $-\mathrm{Im}\,\omega_w/\omega_0$ is estimated to be in the range of $(3-5)\times 10^{-4}$ and increases with temperature as shown in Figure 1.9b.

The formation of a cavity is a gradual process and can be described as a gradual increase in the well width. During this process, the wave energy is absorbed, leading to a decrease in the mode frequency with time. This process is quantified by the absorption coefficient, defined as the ratio of the imaginary part of the wave frequency to its real part, as described by (1.71). The absorption coefficient is approximately constant during the later stages of the cavity's evolution, with a temperature dependence that tends to increase.

The cavity formation is terminated when the ponderomotive pressure of trapped waves is equalized with the thermal pressure of the ambient plasma. So, the energy stored in the cavity can be estimated as $0.25\, n_{\mathrm{cr}} T_e \Delta x_w$, which corresponds to about 1 kJ/cm$^2$ for our conditions. The cavity life time is defined by the damping of the trapped mode, which is about 1 ps according to equation (1.71). Therefore, cavitation and subsequent collisionless absorption of trapped electromagnetic waves could be an important mechanism of laser energy absorption as one can see in Table 2.1. We estimate the value of $f_{\mathrm{cav.abs}}$ in Section 1.5 to be approximately 0.1% for the cavity width $\Delta x_w/\lambda_0 = 7.7$ and electron temperature of 3.4 keV. This estimate is in agreement with the similar value observed in our PIC simulations.

The mode damping in a cavity is an important aspect of the nonlinear laser absorption process, with a flexible way of controlling the absorption via SRS. The collisional and collisionless processes compete with each other, as the damping rate of the trapped electromagnetic wave is compatible with the collisional damping rate.

Collisional damping rate of the scattered electromagnetic wave is proportional to the electron-ion collision frequency evaluated at the quarter critical density $\nu^*_{\mathrm{ei}}$, which is $\sim 1-2$ ps$^{-1}$ for the conditions of interest. This value corresponds to the ratio $\nu^*_{\mathrm{ei}}/\omega_0 \simeq 4\times 10^{-4}$, which is an order of magnitude smaller than the SRS temporal growth rate shown in figure 1.5a, but could be comparable or larger than the collisionless damping rate of the electromagnetic wave trapped in the cavity (1.71). For the chosen plasma parameters the value of absorption coefficient is $f_{\mathrm{col.abs}} \approx 0.3$. Thus about 30% of the scattered wave energy could be absorbed in plasma due to collisions.

Moreover, the collisional absorption of the scattered electromagnetic wave makes also

a notable contribution to the absorption process. This can be seen in Figure 2.3 when comparing the cases with and without collisions. In the reference case, there is no difference between the runs i) and ii): since the SRS is suppressed by a strong SBS in a low density plasma. By contrast, there is a notable electron and ion heating in the case of expanding plasma: in the run iii) without collisions, both electrons and ions are heated due to SRS excitation and energy absorption in cavities. In the run iv) with collisions, there is less ion heating and more electron heating due to the collisional absorption of the SRS scattered wave.

## 2.5 Hot electron generation

The energy fluxes for both electrons and ions are shown in Figure 2.6. The electron energy flux is almost zero for densities below the quarter critical density. A dramatic increase in the electron energy flux near the quarter critical density indicates the location of SRS activity and the zone where electrons and ions are accelerated. A correlation of strong electron and ion energy fluxes is due to the formation of a cavity, where a trapped strong electromagnetic field ejects electrons and ions in both directions. Electrons dominate the energy flux, with ion contributions being less than 10%. The electron energy flux through the rear boundary is maintained at a level of 6-7% in the quasi-stationary regime, in agreement with the overall energy balance discussed above in Section 2.3.

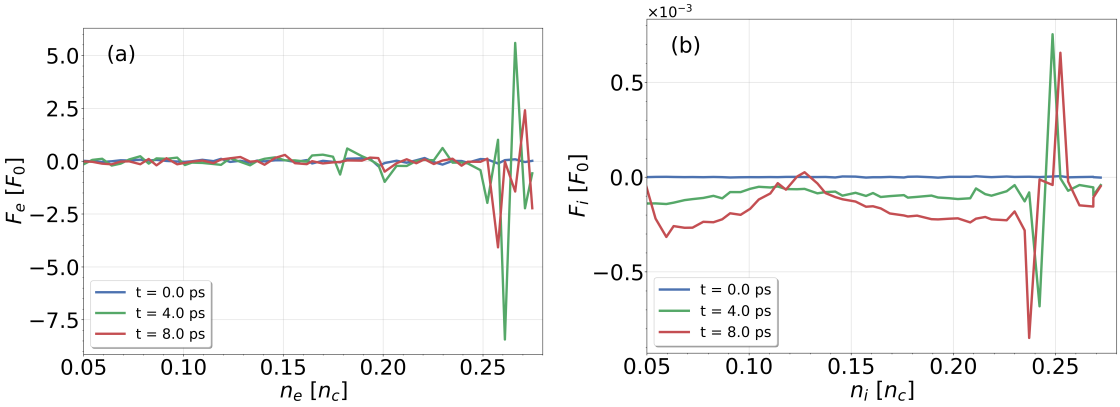


Figure 2.6: Electron (a) and ion (b) energy flux in the simulation box as a function of initial plasma density for the case i) of a collisionless plasma at time of 0, 4 and 8 ps. The curves are normalized to the incident laser intensity.

In the case of strong SRS excitation iii), the electron acceleration in Langmuir waves leads to the formation of a two-temperature distribution, as shown in Fig. 2.7a. This distribution can be fit with a Maxwellian two-temperature distribution Eq. (1.78) with temperatures $T_{e,\mathrm{bulk}} \simeq 3.5$ keV for the bulk component and $T_{e,\mathrm{hot}} \simeq 35$ keV for the hot component, with a relative concentration ratio $n_h/n_{\mathrm{bulk}}$ of 10.7%. The high energy tail of

the distribution function corresponds to $p_x > 0.3\, m_e c$.

In case v) of two ion species, the electron energy flux density contains only the bulk part, without a notable high energy tail at $p_x \simeq 0.3 - 0.4\, m_e c$ as it is shown in Figure 2.7a. Despite the lower hot electron concentration compared to case iii), the distribution is still fitted with a two-temperature Maxwellian function, with temperatures of bulk $T_{e,\mathrm{bulk}} \simeq 3.4$ keV and hot $T_{e,\mathrm{hot}} \simeq 35$ keV and a ratio of concentrations $n_h/n_{\mathrm{bulk}}$ of 3.3%. The temperature of hot electrons is similar to the case iii), but the concentration of hot electrons and total flux are 2.5 times lower.

In case vi) of broadband laser the electron energy flux is similar to the case v) with two ion species, but with a small plateau near $p_x \simeq 0.15 m_e c$, which is probably related to a collisional absorption. The energy flux is fitted with a Maxwellian two-temperature distribution, with temperatures of bulk electrons $T_{e,\mathrm{bulk}} \simeq 3.4$ keV and hot electrons $T_{e,\mathrm{hot}} \simeq 10$ keV and a ratio of concentrations $n_h/n_{\mathrm{bulk}}$ of 8.8%. These parameters are presented in Table 2.2.

The two-temperature approximations observed in the cases iii) and v) provide valuable insights into the dynamics of the electron acceleration in Langmuir waves. However, the presence of density cavities, as discussed in Section 1.5, may contribute in shaping the distribution.

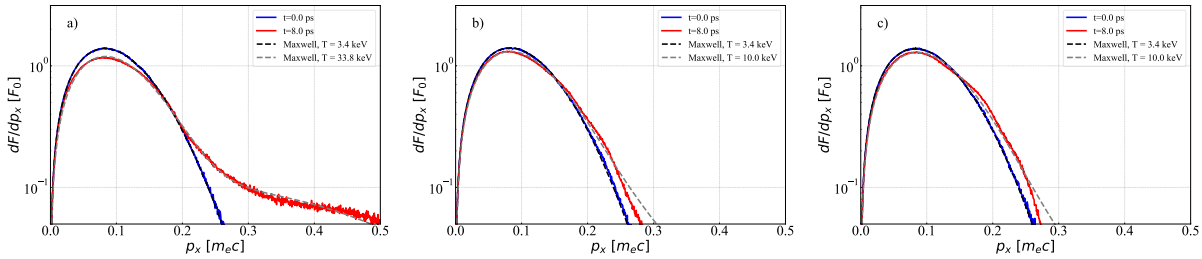


Figure 2.7: Distribution of the electron energy flux density near the quarter critical plasma ($n_e \sim 0.25\, n_{\mathrm{cr}}$) on the parallel momentum, $dF/dp_x$ averaged over the first (blue) and last 0.5 ps (red) for the case iii) of expanding plasma (a), for the case v) with two ion species (b) and for the case vi) of broadband laser pulse (c). Black/gray dashed line is an electron energy flux fitted with a Maxwellian function (1.78) for $p_x > 0$, corresponding to temperatures of 3.4/34 keV (a), 3.4/10 keV (b) and 3.4/10 keV (c). All curves are normalized to the incident laser energy flux density $F_0$.

The electron distribution function, represented in Figure 2.9, can be approximated by a sum of two Maxwellian functions (2.8). A closer look at the figure reveals that the relative concentration of hot electrons is higher for the case iii) near quarter critical density as compared to cases v) and vi), and the relative temperature is also higher. The Maxwellian two-temperature fit, used to determine bulk temperatures for all cases, indicates that these temperatures are slightly lower than the initial temperature of 3.4 keV, which is due to a relatively large noise level. The correct value of the bulk temperature

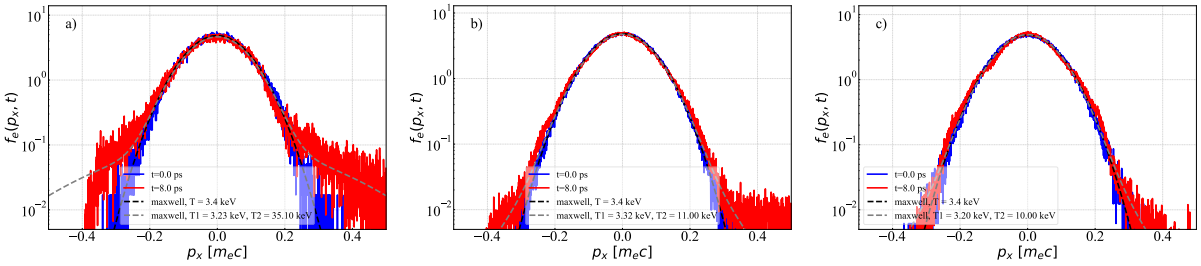


Figure 2.8: Electron distribution function $f_e$ on the parallel momentum near the quarter critical plasma $n_e \sim 0.25\, n_{\rm cr}$, at $t = 0$ ps (blue) and $t = 8$ ps (red) for the case iii) of expanding plasma (a), the case v) with two ion species (b) and the case vi) of broadband laser pulse (c). Black/gray dashed line is an electron distribution function fitted with Maxwellian function (2.8) for $p_x > 0$, corresponding to the bulk/hot temperatures of 3.3/35 keV (a), 3.3/11 keV (b) and 3.3/10 keV (c). All curves are normalized to unity.

is calculated from the distribution function averaged over the entire simulation box, i.e. $\bar{f}_e = \int dx f_e(p_x, x)/l_n$. The effect of spatial averaging can be seen from comparison Figures 2.8 and 2.9.

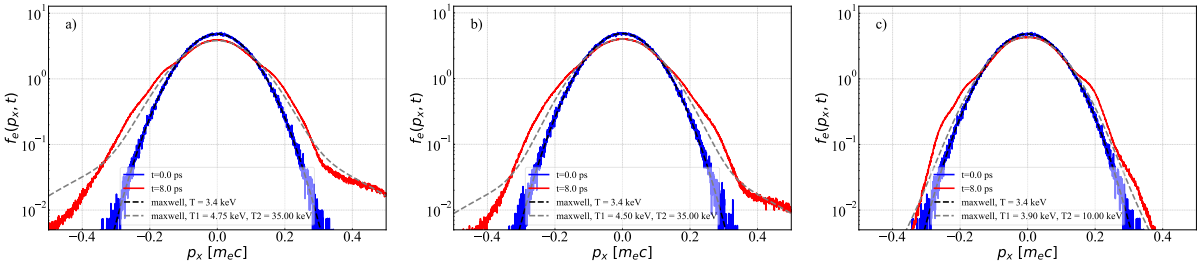


Figure 2.9: Electron distribution function $f_e$ on the parallel momentum averaged over the simulation box at $t = 0$ ps (blue) and $t = 8$ ps (red) for the case iii) of expanding plasma (a), for the case v) with two ion species (b) and for the case vi) of broadband laser pulse (c). Black/gray dashed line is an electron distribution function fitted with Maxwellian function (2.8) for $p_x > 0$, corresponding to the initial/current bulk/hot temperature of 3.4/4.75/35 keV (a), 3.4/4.5/11 keV (b) and 3.4/3.9/10 keV (c). All curves are normalized to unity.

At $t = 8$ ps, the temperatures of the bulk plasma are consistent with the values shown in Figure 2.3. In terms of the generation of hot electrons, the relative contribution of SRS in cases iii) and v) are estimated to be roughly equal. However, the instantaneous electron energy distribution near a quarter of critical density cannot provide an accurate picture of the entire simulation box. Electrons with energies of $\sim 35$ keV may appear slightly below a quarter of critical density due to convective SRS amplification, which is observed in the cases iii) and v). The relative timing of the appearance of these electrons may also differ, as the SRS-SBS competition is a complex process, with SRS sometimes suppressing SBS and vice versa. Table 2.2 illustrates this interplay. The relative concentrations and temperatures of the hot electrons are calculated by averaging them over the entire box,

and the total flux is computed using (1.78) by selecting particles with $|p| > 0.3 m_e c$. Although cases iii) and v) are quite similar, the total amount of hot electrons and their temperature are higher compared to the case vi).

| # | Simulation | $n_h/n_{\text{bulk}}$ | $T_h$ | Total flux $F/F_0$ |
|---|---|---|---|---|
| iv) | Expanding collisional plasma | 10% | 35 keV | 10% |
| v) | Two ion species, collisionless | 10% | 35 keV | 9% |
| vi) | Phase-modulated pump, collisionless | 7% | 10 keV | 6.1% |

Table 2.2: Hot electron concentration, temperature and total flux averaged over the last 0.5 ps of simulation time and over the simulation box for the three representative cases.

## 2.6 Ion heating and acceleration

Excitation of parametric instabilities leads also to the ion heating. It is related to two processes: damping of ion acoustic waves excited by SBS in a low density plasma, $n_e/n_{\text{cr}} \lesssim 0.2$, and expansion of cavities created at nonlinear stage of SRS evolution near the quarter critical density. A negative ion energy flux in a low-density plasma ($n_e < 0.22\, n_{\text{cr}}$) shows two specific features. First, a steady ion flux linearly increasing with time is due to plasma expansion. From the expression for the ion energy flux related to the plasma expansion, $F_i = \frac{3}{2} n_i T_i v_i$, and the increase rate $dF_i/dt$ presented in Figure 2.6b of $4 \times 10^{-5} F_0$ over 4 ps, we can evaluate the ion acceleration, $dv_i/dt = -10^{-3}\mu\text{m/ps}^2$. Another particular feature of the ion energy flux is its increase in the low-density region ($n_e/n_{\text{cr}} = 0.10 - 0.15$). This corresponds to forward ion acceleration by SBS-driven ion acoustic. This effect is weak at $t = 4$ ps and becomes much stronger at $t = 8$ ps, indicating that SBS is excited later, after $3 - 4$ ps, and creates a strong ion flux on the order of $0.1\, F_0$.

A comparison of the ion temperature evolution for different cases in Figure 2.3b shows that cavitation makes a strong contribution with ion temperature increase by more than 30% during the simulation time.

A more detailed analysis of the ion dynamics is presented in Figures 2.10 and 2.11 showing distribution of the ion energy flux on the momentum $p_x$ near the quarter critical density. Figure 2.10 shows the case v) of two ion species. According to [60], [61], for the temperature ratio, $T_i/T_e \simeq 0.3$, the fast mode has a smaller damping increment, $\text{Im}\,\omega_{\text{IAW}}/\text{Re}\,\omega_{\text{IAW}} \simeq 0.24$, and it is excited in the SBS process. The phase velocity of this mode $\simeq 0.76\,\mu\text{m/ps}$ is approximately two times the hydrogen thermal velocity and it is approximately eight times the carbon thermal velocity. Consequently, a comparison of the left and right panels in Figure 2.10 shows that hydrogen ions are gaining much more energy than carbon ions from the ion acoustic waves.

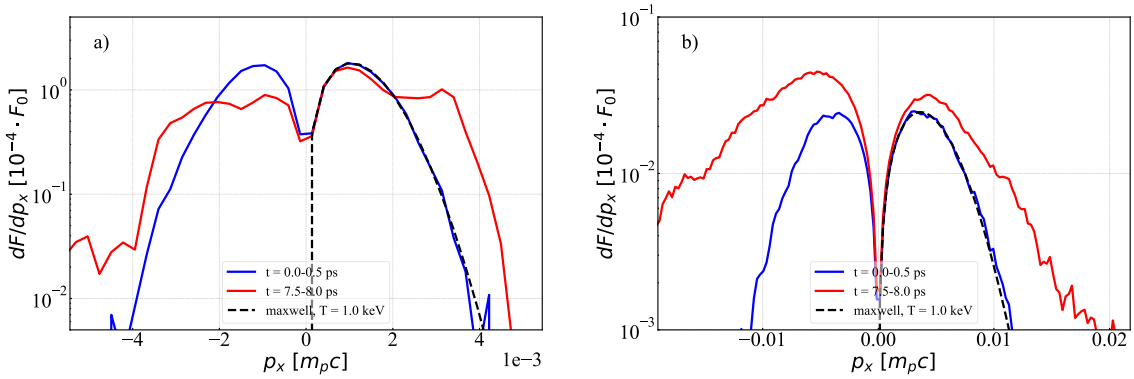


Figure 2.10: Distribution of the ion energy flux density near the quarter critical plasma on the parallel momentum, $dF/dp_x$ averaged over the first (blue) and last 0.5 ps (red) for the case v) with two ion species: a) hydrogen and b) carbon. Black dashed line is an ion energy flux fitted with Maxwellian function (1.78) for $p_x > 0$ corresponding to the initial temperature of 1 keV. All curves are normalized to the incident laser energy flux density $F_0$. Total ion energy flux through the quarter critical plasma is about $1.6 \times 10^{-3} F_0$ for hydrogen and $\sim 10^{-4} F_0$ for carbon.

SBS develops in the case v) near the quarter critical density. Indeed, the distribution function of both ion species is modified essentially for positive velocities and in the range larger than the ion acoustic velocity. The cutoff of the proton distribution at $p_x \simeq 5 \times 10^{-3} m_p c$ corresponds to the proton energy of 12 keV and velocity approximately three times the phase velocity of the slow mode. Velocity of carbon ions is about 5 times smaller than the hydrogen velocity and they are carrying an order of magnitude smaller energy flux.

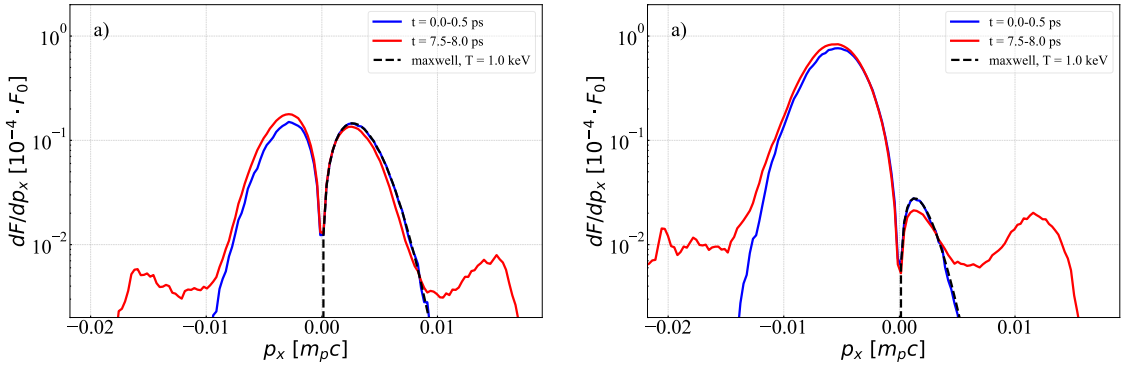


Figure 2.11: Distribution of the ion energy flux density entering the quarter critical plasma on the parallel momentum, $dF/dp_x$ averaged over the first (blue) and last 0.5 ps (red) for broadband laser pulse vi) a) and for expanding plasma iii) b). Black dashed line is an ion energy flux fitted with Maxwellian function (1.78) for $p_x > 0$ corresponding to the initial temperature of 1 keV. All curves are normalized to the incident laser energy flux density $F_0$.

Figure 2.11 shows the ion energy flux for two other simulations with a single ion species with an expanding plasma iii) and a broadband laser pulse vi). SBS is suppressed in these

two runs and modification of the ion distribution function is completely different. The ions are accelerated symmetrically in the positive and negative directions and their velocities are 1.5 times larger than the ion acoustic velocity $c_s \simeq 0.5\,\mu$m/ps, which corresponds to the ion momentum $\sim 10^{-2} m_p c$. This symmetric ion acceleration is explained by their expansion from the cavities produced at the nonlinear stage of SRS evolution. This interpretation is confirmed by the reduction of backward reflectivity and electron heating observed in these runs.

The overall comparison of cases is presented below.

- In case v), two ion species are considered, and the ion temperature evolution is shown in Figure 2.3b. The results show that cavitation makes a significant contribution to ion temperature increase during the simulation time, by more than 30%. The distribution function of both ion species is modified by SBS, and the hydrogen ions are gaining much more energy than carbon ions from the ion acoustic waves.

- In case iii), a single ion species is considered, and the plasma expands due to the cavities produced at the nonlinear stage of SRS evolution. The ions are accelerated symmetrically in the positive and negative directions, and their velocities are 1.5 times larger than the ion acoustic velocity. The reduction of backward reflectivity and electron heating observed in this case confirms that this symmetric ion acceleration is explained by their expansion from the cavities produced by SRS.

- In case vi), a broadband laser pulse is used, and the total amount of hot electrons and their temperature are lower than in cases iii) and v). The ion energy flux shows a steady linear increase with time due to plasma expansion, but there is no significant increase in the low-density region. The ion temperature evolution shows that cavitation makes a smaller contribution to ion temperature increase than in case v).

Furthermore, these cases demonstrate that the excitation of parametric instabilities leads to ion heating, and the specific characteristics of the ion dynamics and heating depend on various factors such as the plasma density, the presence of multiple ion species, and the type of laser pulse used. In particular, the presence of SBS leads to significant ion heating through the excitation of ion acoustic waves and modification of the ion distribution function. The expansion of plasma due to cavities produced by SRS also contributes to ion acceleration and heating.

## 2.7 Comparison of one- and two-dimensional simulations

The simulations of SBS-SRS competition presented in this chapter in one-dimensional (1D) geometry are representative for the shock ignition scenario. This is demonstrated in this section, where we present the results of simulations performed in 2D geometry for the similar interaction conditions. Although 2D simulations require much larger computational resources, the results not much different from the corresponding 1D case. In particular, we do not observe TPD in the 2D simulations and the characteristics of hot electrons driven by SRS are similar.

The methodology of 2D simulations is described in Section 2.1.2, where we discuss the use of hydrodynamic simulations for producing the initial conditions for PIC simulations. The large scale laser plasma interaction is modeled with a radiation hydrodynamic code CHIC [70]. We characterized the plasma corona by four parameters: the laser intensity in the center of focal spot $I_{\mathrm{las}}$, the density scale length $L_n$ at the quarter critical density, assuming an exponential density profile $n_e(x) = n_{\mathrm{cr}} \exp(x/L_n)$ along the target normal, and the electron and ion temperatures $T_e$ and $T_i$, respectively. The plasma of plastic (CH) is modeled as a combination of electrons and a single species of ions with a charge of $Z_{\mathrm{eff}} = 3.5$ and atomic mass of $A_{\mathrm{eff}} = 6.5$. Figure 2.1a displays the temporal profile of the laser pulse, with five representative points marked by circles.

### 2.7.1 Energy balance

In each simulation point, the interaction process enters a quasi-stationary regime after $5-6$ ps, when the internal energy in the simulation box remains roughly constant. In this analysis, we only consider the asymptotic stage of each simulation. The energy balance averaged over the last 1 ps of the simulation is presented in Table 2.3.

| pulse time $t_p$, ps | backscattered fraction SBS/SRS | sidescattered fraction | transmitted fraction | hot electron temperature, keV | bulk electron temperature, keV |
|---|---|---|---|---|---|
| -200 | 0.40/0.001 | 0.55 | 0.05 | 48 | 2.9 |
| -100 | 0.33/0.02 | 0.58 | 0.07 | 62 | 4.6 |
| 0 | 0.12/0.03 | 0.64 | 0.21 | 90 | 5.7 |
| 100 | 0.12/0.04 | 0.6 | 0.24 | 93 | 5.0 |
| 200 | 0.35/0.02 | 0.6 | 0.07 | 57 | 4.4 |

Table 2.3: Energy balance in the simulation box observed in PIC simulations.

The data presented in Table 2.3 reveal that most of the scattered energy is carried by slightly frequency-shifted light. This can be attributed to the specular reflection and

SBS. The fraction of scattered light due to these processes gradually decreases from 95% at the start of the laser pulse, where the reflection from the critical density dominates, to approximately 80% at the maximum of the laser pulse, where SBS dominates. The strongly shifted light only contributes a relatively small portion, reaching only 3-4% at the maximum of the laser pulse.

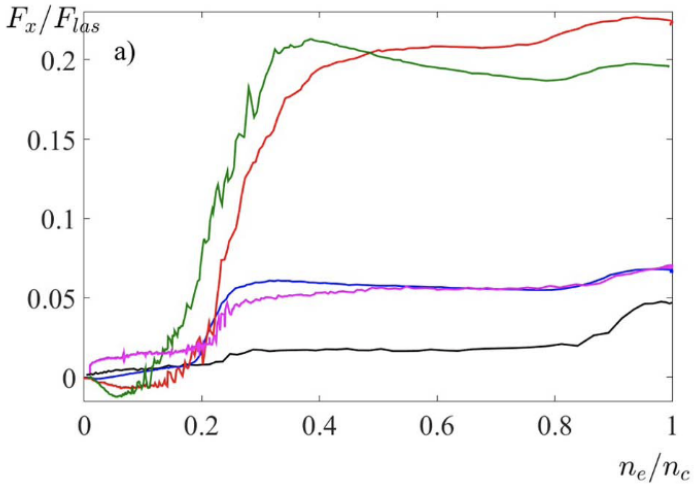


Figure 2.12: Dependence of the longitudinal component of the electron energy flux $F_x$ (1.76) on the plasma density averaged over the transverse coordinate and last 1 ps of the simulation time. All curves are normalized to the incident laser energy flux density $F_{\text{las}}$. The five lines correspond to the pulse times $t_p$ given in Table 2.3: black $t_p = -200$ ps, blue $t_p = -100$ ps, red $t_p = 0$, green $t_p = 100$ ps and pink $t_p = 200$ ps.

The energy flux transmitted beyond the critical density is carried by thermal and suprathermal electrons. In the quasi-stationary state, the energy flux of these electrons equals the absorbed laser energy flux. As indicated in Table 2.3, the average energy of the suprathermal electrons is 10 times higher than the plasma temperature. The origin of these hot electrons is illustrated in Figure 2.12. The left panel of the figure displays the dependence of the longitudinal component of the electron energy flux $F_x$ on the plasma density averaged over the transverse direction. The electron energy flux $F_{ex}$ is defined by Eq. (1.76).

According to the results presented in Figure 2.12 and Table 2.3, the coupling of laser energy to plasma is negligible in the density range below $0.2\,n_{\text{cr}}$, as the electron energy flux is almost zero. At the quarter critical density, there is a significant increase in the electron energy flux in the density interval of $0.2\,n_{\text{cr}}$ to $0.3\,n_{\text{cr}}$, indicating a significant absorption of the laser energy through parametric instabilities. However, in the region before the critical density of $0.85\,n_{\text{cr}}$ to $0.95\,n_{\text{cr}}$, there is also an increase in electron flux in early times at $t_p = -200$ and $-100$ ps, but not in later times. This is likely due to the absence of collisions in the simulation, and the observed laser energy absorption is fully

nonlinear. Further analysis reveals that SRS is the dominant absorption process.

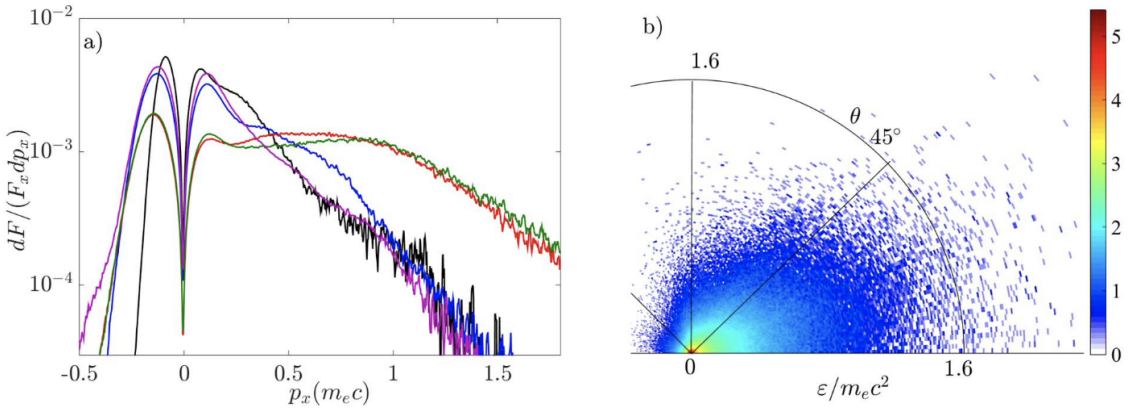


Figure 2.13: a) Distribution of the electron energy flux entering in the overcritical plasma $n_e \geq n_{\rm cr}$ on the parallel momentum, $dF_x/dp_x$. All curves are normalized to the total electron energy flux at that position. Five lines in both panels correspond to the pulse times $t_p$ given in Table 2.3. The color code is the same as in Figure 2.12. Distribution of electrons in the plasma near the critical density in function of the energy $\varepsilon$ and the polar angle $\theta$. The laser pulse time $t_p = 0$ and the quasi-steady phase of the simulation are considered. Color bar is in logarithmic scale.

Compared to 1D simulations, the behavior of hot electrons in the 2D case is more intricate. Despite the bulk electron temperatures being similar to those in 1D simulations, the effective temperature of hot electrons is higher in some cases and similar in others. The effective temperature of hot electrons gradually increases from 48 keV at $t_p = -200$ ps to 93 keV at $t_p = 100$ ps, representing an increase of at least $1.5 - 2.5$ times. The hot electron flux of $5 - 20\%$ is comparable to that observed in 1D simulations. The primary absorption mechanism is linked to the excitation of side scattered SRS, which is an absolute instability similarly to backward SRS near the quarter critical density. The obliquely propagating scattered daughter waves experience difficulty escaping the plasma due to their small group velocity and large amplitude. They are partially trapped near the excitation zone. The daughted electron plasma waves drive a secondary parametric decay instability (PDI), which corresponds to the excitation of pairs of electron plasma and ion acoustic waves with equal and opposite wave vectors. However, we did not observe PDI in our 1D simulations, instead we observed a stronger cavitation.

The distribution of hot electron flux on the parallel momentum, $dF_x/dp_x$ corresponds to the effective temperatures of hot electrons presented in Table 2.3 is similar to the one presented in Section 2.5. The angular distribution of hot electrons is shown in Figure 2.13, and it is observed to be rather broad with a characteristic opening angle of approximately 50 degrees. This broad distribution is explained by the broad angular spectrum of plasma wave turbulence excited in the zone of laser energy absorption.

Based on this comparison, we observe many similarities for the case of a single species

static plasma. The role of additional effects such as two species or plasma flow in 2D case needs further studies. However, based on 1D simulations, we expect the suppression of SBS and a larger contribution of SRS in the nonlinear laser absorption.

## 2.8 Conclusion for Chapter 2

This chapter presents the results of PIC simulations for studying the competition of SRS and SBS processes in laser plasma interaction for shock ignition conditions. The use of PIC codes has proven to be a powerful tool for modeling collisionless and weakly collisional plasmas, and allows us to capture the essential features of plasma dynamics. We begin this chapter by describing the Maxwell-Vlasov system of equations used for modeling the dynamics of a plasma. We then introduce the concept of macro-particles, which are used to capture the essential features of the plasma dynamics in PIC simulations. We also discuss how the Maxwell's equations are solved using the PIC method and the advantages and drawbacks of using PIC codes for plasma simulations.

To interpret experiments that involve laser-plasma interactions, it is often necessary to use both hydrodynamic simulations and PIC simulations. Coupling of these two approaches is discussed in Section 2.1.2. Hydrodynamic simulations are effective for modeling the plasma dynamics on longer time and larger length scales, but are limited in their ability to accurately capture the details of the nonlinear processes that occur in the plasma. On the other hand, PIC simulations can accurately capture the nonlinear processes, but are computationally expensive and can only model a small region of the plasma. We discuss the principle of using PIC simulations to inform the input data for hydrodynamic simulations, which can then be used to model the interaction between the laser and the plasma on larger scales. The hydrodynamic simulations provide the initial conditions (Section 2.1.2) for the PIC simulations, which then provide detailed information on the nonlinear absorption processes and the resulting plasma dynamics.

The competition between SBS and SRS and their role in laser energy absorption under shock ignition conditions is considered by choosing six representative cases described in Section 2.2. Spatial and temporal evolution of various plasma parameters are analyzed, and the growth rates and spatial gains of SBS and SRS in each case are compared. The results are presented in figures and tables for easy comparison and discussion. The study provides a comprehensive understanding of the SBS-SRS competition in laser energy absorption and the influence of various plasma parameters on this process.

In the collisional and collisionless simulations of a plasma with zero flow velocity, SBS dominates and suppresses SRS, resulting in a low laser absorption, see Section 2.3. In the case of expanding plasma, SBS is suppressed, and laser absorption is dominated

by SRS near the quarter of critical density and plasma cavitation, resulting in a much better absorption. The role of electron collisions is more important in the expanding plasma, resulting in an increase of electron temperature. In the case of two ion species, the improved laser absorption is explained by the SBS suppression related to a stronger ion acoustic damping on light ions. We conclude that laser energy absorption in plasma increases significantly when SBS is suppressed.

The use of a phase-modulated laser pulse can also lead to SBS suppression and favor SRS, but the specific case considered in the study has a correlation time of $\tau_c \sim 0.5$ ps, which is relatively large and results in only a small reduction of reflectivity. To achieve a more efficient SBS suppression, it is recommended to increase the laser bandwidth by at least $2 - 3$ times.

In the cases of strong SRS excitation discussed in Section 2.5, the electron acceleration in Langmuir waves leads to the formation on an suprathermal tail, which is fitted with a Maxwellian two-temperature distribution with temperatures of bulk and hot electrons and corresponding concentrations. The electron acceleration in Langmuir waves and the resulting two-temperature distribution provide valuable insights into the dynamics of this process. The findings can be utilized in the improvement of models for SRS and electron acceleration in plasmas.

In addition, these cases show a significant modification of the ion distribution functions. As shown in Section 2.6, the excitation of parametric instabilities induces ion heating and acceleration. The distinctive features of ion dynamics are influenced by such factors as plasma density, multiple ion species, and laser pulse intensity. Notably, SBS triggers considerable ion heating through ion-acoustic wave Landau damping, and ion acceleration is facilitated by the plasma expansion caused by SRS-induced cavities.

In summary, we have reviewed a range of adaptable techniques for managing the competition between SRS and SBS in inertial fusion plasmas. Reducing SBS reflectivity promotes the occurrence of absolute and convective SRS excitation, electron acceleration, and cavitation. The latter effect has the potential to significantly enhance laser absorption by capturing the backscattered light. A comparison with the 2D simulation of a collisionless, single species plasma shows that the conclusions related to other cases can be relevant to large dimensions and to experiments in the shock ignition conditions.

# Chapter 3

# Studies of laser interaction with low density foams

## 3.1 Introduction

The use of low-density foams in laser-plasma interaction experiments and in applications, such as inertial confinement fusion and bright sources of x-rays and charged particles [125]–[128], has gained attention due to their attractive properties. However, the process of transforming a cold foam into hot plasma remains complicated and poorly understood. Through experiments and numerical simulations, it has been observed that the ionization of foam by laser occurs slower compared to that of a homogeneous material with the same average density. The reason behind this lies in the additional energy needed to transform foam solid elements into plasma and fill the spaces between them.

The transformation of a cold heterogeneous foam into a hot homogeneous plasma is a complex process including laser ionization and heating of solid elements, their expansion and mixing. Experiments and numerical simulations have shown that the ionization of foam by laser occurs slower than the ionization of a homogeneous material with the same average density, thus enabling more laser energy to be stored in the same plasma volume. This can be explained by the time required for the foam's solid elements to expand and mix.

Direct numerical modeling of the laser-foam interaction and foam homogenization using hydrodynamic codes [129], [130] is computationally intensive and requires excessive computational resources. This is due to the need to accurately resolve the density differences within the foam micro-structure. Additionally, the phosics in the conventional hydrodynamic models is limited and does not account for all micro-physics processes that occur at such small sub-wavelength spatial scales.

The process of laser interaction with foam is complex and requires a comprehensive

approach to capture the dynamics of the foam micro-structure. Analytical models [36], [39], [131], while useful in describing idealized one-dimensional interactions, have limitations in their ability to capture the interaction between an inhomogeneous laser beam and a real-sized target. A more advanced approach consists in using a two-scale model, which combines a micro-scale description of the solid element dynamics with a conventional radiation-hydrodynamic description of a plasma produced as a result of mixing of structural elements and foam homogenization. This way, the transformation of a cold foam into a hot plasma can be captured, including effects that may be overlooked in simplified analytical models.

The first sub-grid model proposed by Velechovsky et al. [132] used numerical calculations to determine the laser absorption and expansion of solid foam elements having a planar shape, based on the theory presented by Gus'kov et al. [39]. Belyaev et al. [36], [133] from the Lawrence Livermore National Laboratory proposed an analytical model of foam homogenization based on self-similar isothermal expansion of foam elements having planar, cylindrical or spherical shape. This model is specifically designed for foams with small pores, around 1 $\mu$m, and with a small average density of approximately 2 mg/cm$^3$. The model is implemented in the three-dimensional electromagnetic paraxial code pF3D and was shown to slow down the propagation of the ionization front. However, the results of the model have been found to overestimate the ionization velocity when compared to other experiments with underdense foams [38], [134], [135].

The models mentioned above have a limitation in determining the cross-section of laser absorption in the solid elements based solely on the geometrical size of the overcritical region within the foam. This is particularly problematic for under-critical foams where the width of the solid elements is often smaller or comparable to the laser wavelength. To address this issue, the second part of our study focuses on the analysis of laser interaction with sub-wavelength-sized objects using the wave-based analytical description and detailed 2D PIC simulations. This approach is aimed at providing a more accurate understanding of the laser absorption process, which is highly dependent on laser polarization and the internal structure of the solid elements. Our findings indicate [37] that the geometrical models may either overestimate the absorption rate or severely underestimate the scattering cross-section, in comparison to the data obtained from the Mie theory of electromagnetic scattering on cylindrical particles.

## 3.2 Theory of laser interaction with sub-wavelength structures

The focus of this research is on the interaction of laser radiation with low-density foams made of plastic materials that contain low-$Z$ elements such as hydrogen, carbon, and oxygen. These foams are dielectrics with energy gaps of $4-6$ eV and are transparent to low-intensity light. The interaction process involves the following stages: (i) ionization of solid elements under intense laser radiation, (ii) heating, expansion, and ablation of dense, opaque elements, and (iii) mixing of hot plasmas between neighboring cells and their homogenization. This interaction takes place within the range of laser intensities from $10^{13}$ to $10^{15}$ W/cm$^2$.

The laser intensities under consideration result in a multi-photon ionization process that occurs in sub-picosecond time frames [136]. For laser pulses of duration longer than 100 ps, ionization happens almost instantaneously and solid structural elements become opaque when the laser intensity exceeds $10^{12}-10^{13}$ W/cm$^2$. Hence, in this study, we concentrate on the second step of interaction, which assumes that the solid element in the pore is already opaque and has reached an initial temperature of approximately $T_0 \simeq 1$ eV. The exact value of $T_0$ has a small impact on our results.

Our focus is on the interaction of laser radiation with a single elementary cell or pore in a foam, modeled as a parallelepiped with length $l_c$ and square cross-section of side $l_p$ as shown in Figure 3.1. The pore contains a solid cylinder with an initial radius $a_0$ and density $\rho_s$. Since the cylinder length $l_c$ is much larger than its radius and equal to the pore length, the interaction is effectively two-dimensional. The average foam density $\bar{\varrho}$ is related to the cylinder radius and pore size through mass conservation: $\pi a_0^2 \varrho_s = l_p^2 \rho_{\mathrm{av}}$. We are interested in sub-critical foams, where the fully ionized foam density is lower than the critical density, resulting in a transparent pore after homogenization.

The mathematical treatment of laser absorption and scattering on a cylinder with a radius comparable to the wavelength can be performed using the Mie theory [137], [138]. However, this standard approach considers homogeneous scattering objects, while the radial inhomogeneity of the cylinder plays a crucial role in our study as it enables resonance absorption near the critical density.

In this study, we examine a scenario that can be mathematically analyzed with two simplified physical assumptions. Firstly, we examine the case of an infinitely long straight cylinder that is exposed to a plane wave, which is incident at an oblique angle. Secondly, we consider a cylindrical object with radial density distribution that is axially symmetric, and consider the case of a normal incidence of electromagnetic wave. Despite the anisotropic nature of laser energy deposition and resulting cylinder expansion, this

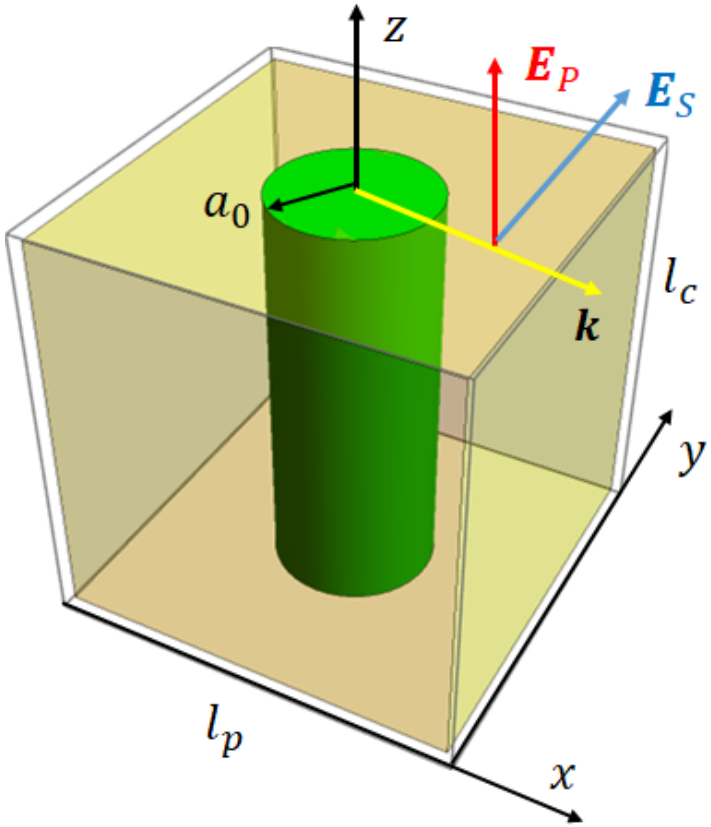


Figure 3.1: Scheme of laser interaction with a cylinder in the case of P (red) and S (blue) polarization.

example offers valuable insights into the physics of laser absorption in a foam.

### 3.2.1 Theory of laser absorption and scattering

The study of electromagnetic wave absorption and scattering by sub-wavelength objects has a rich history dating back to the 19th century and includes notable names such as Young, Fresnel, Stokes, Rayleigh, and Mie. In the monograph by Van de Hulst [137], the interaction of a plane electromagnetic wave with a solid object is quantified by the absorption and scattering efficiency factors $Q_{\text{abs}}$ and $Q_{\text{sca}}$, which are ratios of the corresponding cross-section to the geometrical cross-section of the obstacle. The sum of two processes involved, scattering and absorption, is referred to as extinction. The scattering center is characterized by the dielectric permittivity $\epsilon$ and the dimensionless parameter $ka$, where $a$ is the cylinder radius, $k = \omega/c$ is the wave number of the laser, and $\omega$ is the frequency. The calculations are performed in cylindrical coordinates $r, \theta, z$, with the cylinder aligned along the $z$ axis.

### Incident laser field

We examine the case of oblique incidence, which can be separated into two representative cases: linear polarization in the plane of incidence (P-polarization) and polarization perpendicular to the plane of incidence (S-polarization), see Figure 3.1. The former can be described by the electric field vector $\mathbf{E}_p = (-\sin\alpha, 0, \cos\alpha)$, while the latter is described by the electric field vector $\mathbf{E}_s = (0, 1, 0)$. To determine magnetic field, we apply the Faraday equation, which gives us the relationship $\mathbf{k}\times\mathbf{E}_0 = (\omega/c)\,\mathbf{B}_0$. Specifically, the magnetic field components for P-polarization and S-polarization are: $\mathbf{B}_s = (-\sin\alpha, 0, \cos\alpha)$ and $\mathbf{B}_p = (0, -1, 0)$, respectively. These polarizations correspond to the cases I and II, respectively, as defined in Ref. [137].

The coordinate dependence of electric and magnetic fields on the incident wave can be expressed as a function $w_0(x, z) = \exp(ik_z z + ik_x x)$, which can be written in cylindrical coordinates as an expansion in a series of Bessel functions of the first kind, $J_n$:

$$w_0(r, \theta) = \mathrm{e}^{ik_z z} \sum_n i^n \mathrm{e}^{in\theta} J_n(k_x r). \tag{3.1}$$

To calculate the scattered field, we must determine the tangential components of the electric and magnetic fields, which can be obtained using the following expressions:

$$w_0 \cos\theta = -i\mathrm{e}^{ik_z z} \sum_n i^n \mathrm{e}^{in\theta} J_n'(k_x r),$$
$$w_0 \sin\theta = -\frac{1}{k_x r}\mathrm{e}^{ik_z z} \sum_n i^n \mathrm{e}^{in\theta} n J_n(k_x r).$$

Thus, the components of the incident field in the cylindrical coordinates for the case of P-polarization are given by:

$$\begin{aligned} \{E_z, E_r, E_\theta\} &= \{\cos\alpha\, J_n, i\sin\alpha\, J_n', -\frac{n}{\xi}\sin\alpha\, J_n\}, \\ \{B_z, B_r, B_\theta\} &= \{0, \frac{n}{\xi} J_n, iJ_n'\}. \end{aligned} \tag{3.2}$$

Here, $\xi = k_x r = kr\cos\alpha$ is the argument of the Bessel functions and the common factor in all expressions, $\mathrm{e}^{ik_z z}\sum_n i^n \mathrm{e}^{in\theta}$, is omitted. Similarly, for the case of S-polarization, the electric and magnetic fields are inverted:

$$\begin{aligned} \{E_z, E_r, E_\theta\} &= \{0, -\frac{n}{\xi} J_n, -iJ_n'\}, \\ \{B_z, B_r, B_\theta\} &= \{\cos\alpha\, J_n, i\sin\alpha\, J_n', -\frac{n}{\xi}\sin\alpha\, J_n\}. \end{aligned} \tag{3.3}$$

### Scattered fields

Scattered fields for P and S-polarization can only be separated in the case of normal incidence of an electromagnetic wave ($\alpha = 0$). In the general case, they contain both polarizations. The scattered fields can be determined by using the Ampere and Faraday equations:

$$\begin{aligned} -i\omega\epsilon\mathbf{E} &= c\,\mathrm{rot}\mathbf{B}, \\ i(\omega/c)\,\mathbf{B} &= \mathrm{rot}\mathbf{E}. \end{aligned} \tag{3.4}$$

If we exclude either the magnetic or electric field and use the other pair of Maxwell's equations, i.e., $\mathrm{div}(\epsilon\mathbf{E}) = 0$ and $\mathrm{div}\mathbf{B} = 0$, we can express them as two separate equations:

$$\begin{aligned} \triangle\mathbf{E} + \left(\frac{\omega}{c}\right)^2 \epsilon\mathbf{E} &= -\nabla\left(\frac{\nabla\epsilon}{\epsilon}\cdot\mathbf{E}\right), \\ \triangle\mathbf{B} + \left(\frac{\omega}{c}\right)^2 \epsilon\mathbf{B} &= -\frac{\nabla\epsilon}{\epsilon}\times\mathrm{rot}\mathbf{B}. \end{aligned} \tag{3.5}$$

In our case, the dependence on the axial coordinate is given by the incident wave in the form of $\mathrm{e}^{ik_z z}$, and we need to determine the scattered field in the polar coordinates $r$ and $\theta$. One approach is to use Eqs. (3.5) for the axial components of the electric and magnetic fields, and Eqs. (3.4) to solve the coupling terms in the right-hand side of Eqs. (3.5). To do this, we introduce two auxiliary functions $u$ and $v$ such that

$$\begin{aligned} E_z &= u(r,\theta)\,\cos\alpha\,\mathrm{e}^{ik_z z}, \\ B_z &= v(r,\theta)\,\cos\alpha\,\mathrm{e}^{ik_z z}, \end{aligned} \tag{3.6}$$

which verify the following equations:

$$\left(\partial_r^2 u + \frac{1}{r}\partial_r u + \frac{1}{r^2}\partial_\theta^2 u + \frac{\omega^2}{c^2}\left(\epsilon - \sin^2\alpha\right)u\right)\cos\alpha\,\mathrm{e}^{ik_z z} = -ik_z\frac{\epsilon'}{\epsilon}E_r$$

$$\left(\partial_r^2 v + \frac{1}{r}\partial_r v - \frac{\epsilon'}{\epsilon}\partial_r v + \frac{1}{r^2}\partial_\theta^2 v + \frac{\omega^2}{c^2}\left(\epsilon - \sin^2\alpha\right)v\right)\cos\alpha\,\mathrm{e}^{ik_z z} = -ik_z\frac{\epsilon'}{\epsilon}B_r$$

The radial and azimuthal components of the fields can be expressed in terms of the auxiliary functions using Eqs. (3.4):

$$E_r = \frac{i\cos\alpha}{\epsilon - \sin^2\alpha}\frac{c}{\omega}\left(\frac{1}{r}\partial_\theta v + \sin\alpha\partial_r u\right), \quad E_\theta = \frac{i\cos\alpha}{\epsilon - \sin^2\alpha}\frac{c}{\omega}\left(\frac{\sin\alpha}{r}\partial_\theta u - \partial_r v\right) \tag{3.7}$$

$$B_r = \frac{i\cos\alpha}{\epsilon - \sin^2\alpha}\frac{1}{\omega}\left(-\frac{\epsilon}{r}\partial_\theta u + \sin\alpha\partial_r v\right), \quad B_\theta = \frac{i\cos\alpha}{\epsilon - \sin^2\alpha}\frac{1}{\omega}\left(\frac{\sin\alpha}{r}\partial_\theta v + \epsilon\partial_r u\right). \tag{3.8}$$

In these expressions, we have omitted the common factor $e^{ik_z z}$ on the right-hand side. Therefore, the scattering process is governed by a system of two coupled equations for the functions $v$ and $u$. As the coefficients in these equations do not depend on the azimuthal angle, they can be expanded in a series of angular harmonics, similar to the equation (3.1):

$$u(r,\theta) = e^{ik_z z}\sum_n i^n e^{in\theta} u_n(\rho), \qquad v(r,\theta) = e^{ik_z z}\sum_n i^n e^{in\theta} v_n(\rho). \tag{3.9}$$

The expansion coefficients $u_n$ and $v_n$ depend on the dimensionless radial coordinate $\rho = kr$, and satisfy the ordinary differential equations:

$$u_n'' + \left(\frac{1}{\rho} - \frac{\sin^2\alpha}{\epsilon - \sin^2\alpha}\frac{\epsilon'}{\epsilon}\right) u_n' + \left(\epsilon - \sin^2\alpha - \frac{n^2}{\rho^2}\right) u_n = \frac{in}{\rho}\frac{\sin\alpha}{\epsilon - \sin^2\alpha}\frac{\epsilon'}{\epsilon} v_n, \tag{3.10}$$

$$v_n'' + \left(\frac{1}{\rho} - \frac{\epsilon'}{\epsilon - \sin^2\alpha}\right) v_n' + \left(\epsilon - \sin^2\alpha - \frac{n^2}{\rho^2}\right) v_n = -\frac{in}{\rho}\frac{\epsilon'\sin\alpha}{\epsilon - \sin^2\alpha} u_n. \tag{3.11}$$

The coefficients $u_n$ and $v_n$ for negative $n$ can be defined using the relations $u_{-n} = (-1)^n u_n$ and $v_{-n} = (-1)^n v_n$, similar to the Bessel functions. Equations (3.10) and (3.11) can be solved numerically for each angular harmonic separately. When the incidence angle $\alpha$ non-zero, the equations are coupled. However, in the special case of normal incidence, the equations are decoupled, and the function $u$ describes the scattering of p-polarized waves, while the function $v$ describes the scattering of s-polarized waves. In the case of a piecewise constant dielectric permittivity, such as a homogeneous cylinder, Eqs. (3.10) and (3.11) are also decoupled. We will consider these two limits in the following sections.

The boundary conditions for Eqs. (3.10) and (3.11) require them to take finite values at the origin, $\rho = 0$, and describe the incoming plane wave of unit amplitude far away from the cylinder. The condition at the origin can be expressed as:

$$u_0'(0) = v_0'(0), \quad u_n(0) = v_n(0) \quad \text{for } n > 0. \tag{3.12}$$

The conditions at $\rho \to \infty$ can be expressed as follows: if the scattering cylinder is localized on a radius $r \sim a$, then far away from the cylinder, $r \gg a$, we can set $\epsilon = 1$ and Eqs. (3.10) and (3.11) are reduced to the standard Bessel equation. The scattered wave can be described by the Hankel function of the first kind, $H_n^{(1)} = J_n + iN_n$. As a result, the solution can be written as a sum of the incident wave of unit amplitude and an outgoing scattered wave:

$$u_n = \sigma J_n(\rho\cos\alpha) - b_n H_n^{(1)}(\rho\cos\alpha), \quad v_n = (1-\sigma) J_n(\rho\cos\alpha) - a_n H_n^{(1)}(\rho\cos\alpha), \tag{3.13}$$

where the scattering amplitudes $a_n$ and $b_n$ introduced in the same way as in [137], $\sigma = 1$

for the p-polarized incident wave and $\sigma = 0$ for the S-polarization. One can use the asymptotic expressions (3.13) to continuously connect the functions $u_n$ and $v_n$ and their derivatives at some point $\rho_m \gg \omega a/c$. This serves two purposes. Firstly, by eliminating coefficients $a_n$ and $b_n$, we obtain the second boundary condition:

$$u_n(\rho_m \cos\alpha) H_n^{(1)\prime}(\rho_m \cos\alpha) \cos\alpha - u_n'(\rho_m \cos\alpha) H_n^{(1)}(\rho_m \cos\alpha) = \frac{2i\sigma}{\pi\rho_m}, \tag{3.14}$$

$$v_n(\rho_m \cos\alpha) H_n^{(1)\prime}(\rho_m \cos\alpha) \cos\alpha - v_n'(\rho_m \cos\alpha) H_n^{(1)}(\rho_m \cos\alpha) = \frac{2i(1-\sigma)}{\pi\rho_m}. \tag{3.15}$$

Secondly, we define the scattering amplitudes

$$b_n = -i\frac{\pi\rho_m}{2}\left[u_n(\rho_m \cos\alpha) J_n'(\rho_m \cos\alpha)\cos\alpha - u_n'(\rho_m \cos\alpha) J_n(\rho_m \cos\alpha)\right], \tag{3.16}$$

$$a_n = -i\frac{\pi\rho_m}{2}\left[v_n(\rho_m \cos\alpha) J_n'(\rho_m \cos\alpha)\cos\alpha - v_n'(\rho_m \cos\alpha) J_n(\rho_m \cos\alpha)\right]. \tag{3.17}$$

**Absorption and scattering coefficients**

By using the asymptotic expression for the Hankel function,

$$H_n^{(1)}(z \to \infty) = \sqrt{2/\pi z}\exp(iz - in\pi/2 - i\pi/4),$$

the scattered field far away from the cylinder can be expressed as shown in Eq. (3.13). This allows for to calculate the fraction of incident energy that is scattered and absorbed. The fields of the outgoing wave take on a simple form as follows:

$$\{E_\theta, E_z\} = -\mathrm{e}^{ik_z z + ik_x x - i\pi/4}\sqrt{\frac{2}{\pi k_x r}}\,\{T_a(\theta), \cos\alpha\, T_b(\theta)\},$$

$$\{B_\theta, B_z\} = \mathrm{e}^{ik_z z + ik_x x - i\pi/4}\sqrt{\frac{2}{\pi k_x r}}\,\{T_b(\theta), -\cos\alpha\, T_a(\theta)\}.$$

The radiated field components that decrease as $r^{-1/2}$ with the coordinate are kept, and are described by the functions $T_a$ and $T_b$, which represent the angular dependence of the scattered field:

$$T_a(\theta) = \sum_n a_n \mathrm{e}^{in\theta}, \quad T_b(\theta) = \sum_n b_n \mathrm{e}^{in\theta}. \tag{3.18}$$

The above equations provide information about the distribution of the radial component of the Poynting vector with respect to the angle:

$$P_r(\theta) = \mathrm{Re}\,(E_\theta B_z^* - E_z B_\theta^*) = \frac{2\cos\theta}{\pi k_x r}(|T_a|^2 + |T_b|^2). \tag{3.19}$$

The scattering cross section per unit length of the cylinder can be obtained by dividing the expression for the radial component of the Poynting vector given in the previous equation

by the radial component of the Poynting vector of the incident wave, $P_{r0} = \cos\alpha$, and then integrating over a large circle with $r \gg a$:

$$\sigma_{\rm sca} = \frac{4}{k_x}(\overline{|T_a|^2} + \overline{|T_b|^2}), \tag{3.20}$$

where overline indicates the angle average,

$$\overline{|T_a|^2} = |a_0|^2 + 2\sum_{n=1}^{\infty}|a_n|^2, \quad \overline{|T_b|^2} = |b_0|^2 + 2\sum_{n=1}^{\infty}|b_n|^2. \tag{3.21}$$

Normalized angular distribution of the scattered light reads:

$$I(\theta) = (|T_a|^2 + |T_b|^2)/(\overline{|T_a|^2} + \overline{|T_b|^2}). \tag{3.22}$$

A similar method can be used to calculate the absorption coefficient, but it would require integration of the dissipated power over the volume of the cylinder, which can be a complex process. A more direct approach is based on the energy conservation, which states that the sum of scattered and absorbed power is equal to the incident power minus the power scattered in the near-forward direction (i.e., $\theta \simeq 0$). By combining the incident and transmitted fields, we can obtain an expression for the total energy flux in the forward direction. For P-polarization, this expression is:

$$P_{r\,\rm tot}(\theta \simeq 0) = -{\rm Re}\,[E_{z0} + E_z(0)][B^*_{y0} + B^*_\theta(0)]. \tag{3.23}$$

We can simplify the expression for the forward energy flux by only considering linear terms in the scattered field, which decreases with the coordinate $x$ as $x^{-1/2}$. Thus, we have $P_{r\,\rm tot} = \cos\alpha - P_{p\,\rm ext}$, where the first term on the right-hand side represents the radial component of the incident Poynting vector, and the second term corresponds to the extincted flux:

$$P_{p,\rm ext} = 2\cos\theta\sqrt{\frac{2}{\pi k_x x}}{\rm Re}\,T_b(0)\,{\rm e}^{-ik_x x + ik_x r - i\pi/4}. \tag{3.24}$$

At large distances $x \gg |y|$, the difference $r - x$ can be expressed as $y^2/2x$. Thus, the factor in the exponential can be simplified. Integrating $P_{\rm ext}(y)$ over the transverse aperture of a sufficiently large width $h \gg (2x/k_x)^{1/2}$, we obtain an expression for the total extincted power:

$$\int dy\, P_{p,\rm ext} = 2\cos\theta\sqrt{\frac{2}{\pi k_x x}}{\rm Re}\,T_b(0)\int dy\,{\rm e}^{ik_x y^2/2x - i\pi/4}. \tag{3.25}$$

After performing the integration $\int dy\, e^{iy/2-i\pi/4} = 2\pi$, dividing the resulting expression by the incident energy flux $P_{r0} = \cos\alpha$ yields the extinction cross section:

$$\sigma_{p,\text{ext}} = \frac{4}{k_x}\text{Re}\, T_b(0). \tag{3.26}$$

Expression for the extinction cross section in the case of S-polarization is similar to that of P-polarization, but contains $T_a$ instead of $T_b$. Dividing the cross sections (3.20) and (3.26) by the geometrical cross section of the cylinder, $2a$, gives us the efficiency factors for extinction and scattering. The absorption factor can be obtained as the difference between the two:

$$Q_{p,\text{ext}} = \frac{2}{ka\cos\alpha}\text{Re}\, T_b(0), \qquad Q_{s,\text{ext}} = \frac{2}{ka\cos\alpha}\text{Re}\, T_a(0), \tag{3.27}$$

$$Q_{\text{sca}} = \frac{2}{ka\cos\alpha}(\overline{|T_a|^2} + \overline{|T_b|^2}), \qquad Q_{\text{abs}} = Q_{\text{ext}} - Q_{\text{sca}}. \tag{3.28}$$

Taking an average over the orientation of the cylinder with respect to the laser polarization corresponds to calculating an arithmetic mean of the efficiency factors for S- and P-polarization. The average over the angle of incidence is computed separately for each polarization as follows:

$$\overline{Q} = \int_0^{\pi/2} d\alpha\, Q\cos\alpha. \tag{3.29}$$

## 3.3 Laser absorption and scattering from a homogeneous cylinder

For a homogeneous cylinder with radius $a$, the solutions to Eqs. (3.10) and (3.11) can be explicitly written in terms of Bessel functions. By applying the boundary conditions (3.12), the solution for $r < a$ is given by:

$$v_n(\rho) = (s/\cos\alpha)\, c_n J_n(s\rho), \quad u_n(\rho) = (s/\cos\alpha)\, d_n J_n(s\rho), \tag{3.30}$$

where $s = \sqrt{\epsilon - \sin^2\alpha}$, and $\epsilon$ is the dielectric permittivity of the cylinder defined by (3.39) below. The solution for $r < a$ can be written explicitly in terms of Bessel functions by applying the boundary conditions (3.12), and it reads as follows. The solution outside the cylinder ($r > a$) is given by expressions (3.14)-(3.15), and four coefficients $A = a_n, b_n, c_n, d_n$ are defined by the continuity conditions of the tangential components of the

electric and magnetic fields at $r = a$. For P-polarization, the outer solution is given by:

$$\begin{aligned}\{E_\theta, E_z\} &= \{ia_n H_n^{(1)\prime}(\xi_a) - (n/\xi_a)\sin\alpha[J_n(\xi_a) - b_n H_n^{(1)}(\xi_a)], \cos\alpha[J_n(\xi_a) - b_n H_n^{(1)}(\xi_a)]\},\\ \{B_\theta, B_z\} &= \{(n/\xi_a)a_n \sin\alpha H_n^{(1)}(\xi_a) + +i[J_n'(\xi_a) - b_n H_n^{(1)\prime}(\xi_a)], -a_n\cos\alpha H_n^{(1)}(\xi_a)\}, \quad (3.31)\end{aligned}$$

where $\xi_a = ka\cos\alpha$. The inner solution reads:

$$\begin{aligned}\{E_\theta, E_z\} &= \{-ic_n J_n'(\zeta) - (n/\zeta)d_n \sin\alpha J_n(\zeta), sd_n J_n(\zeta)\},\\ \{B_\theta, B_z\} &= \{-(n/\zeta)c_n \sin\alpha J_n(\zeta) + i\epsilon d_n J_n'(\zeta), sc_n J_n(\zeta)\}, \quad (3.32)\end{aligned}$$

where $\zeta = ska$. Similar expressions can be obtained also for the S-polarization.

The continuity conditions of the field at the surface of the cylinder $r = a$ can be expressed in the matrix form as:

$$M(ka, \alpha) \cdot A_{s,p} = S_{s,p}(ka, \alpha), \quad (3.33)$$

where $A_{s,p}$ are the coefficients for the scattered fields in the case of S-polarization and P-polarization, respectively and the vectors $S_s$ and $S_p$ on the right-hand side represent the contribution of the incident wave:

$$\begin{aligned}S_s &= \{-iJ_n'(\xi_a), 0, -(n/\xi_a)\sin\alpha J_n(\xi_a), \cos\alpha J_n(\xi_a)\},\\ S_p &= \{-(n/\xi_a)\sin\alpha J_n(\xi_a), \cos\alpha J_n(\xi_a), iJ_n'(\xi_a), 0\},\end{aligned} \quad (3.34)$$

and $M$ is $4 \times 4$ matrix coupling the incident and scattered fields:

$$M = \begin{Bmatrix} -iH_n^{(1)\prime}(\xi_a) & -(n/\xi_a)\sin\alpha H_n^{(1)}(\xi_a) & -iJ_n'(\zeta) & -(n/\zeta)\sin\alpha J_n(\zeta) \\ 0 & \cos\alpha H_n^{(1)}(\xi_a) & 0 & sJ_n(\zeta) \\ -(n/\xi_a)\sin\alpha H_n^{(1)}(\xi_a) & iH_n^{(1)\prime}(\xi_a) & -(n/\zeta)\sin\alpha J_n(\zeta) & i\epsilon J_n'(\zeta) \\ \cos\alpha H_n^{(1)}(\xi_a) & 0 & sJ_n(\zeta) & 0 \end{Bmatrix} \quad (3.35)$$

We consider a simplified case of normal incidence of a laser beam on a cylinder, where the laser propagates in the $x$ direction and the cylinder axis is aligned with the $z$ direction, as shown in Figure 3.1. In this configuration, the two polarizations, S and P, can be analyzed independently. The plane of incidence is defined by the laser propagation direction $x$ and the cylinder axis $z$. The P-polarization corresponds to an electric field in the plane of incidence, with $E_{z0} = \mathrm{Re}\, E_0 \mathrm{e}^{ikx - i\omega t}$, while the S-polarization corresponds to an electric field directed along the $y$ axis.

In the case of normal incidence ($\alpha = 0$), the inner solution reads:

$$v_n(\rho) = s\, c_n J_n(s\rho), \qquad u_n(\rho) = s\, d_n J_n(s\rho), \tag{3.36}$$

where $s = \sqrt{\epsilon}$. The scattering coefficients are defined by the conditions of continuity of tangential components of electric and magnetic fields at the cylinder surface. That gives the following system of equations for the scattering coefficients in the case of P-polarization:

$$\begin{pmatrix} H_n^{(1)\prime}(ka) & s^2 J_n'(ska) \\ H_n^{(1)}(ka) & s J_n(ska) \end{pmatrix} \times \begin{pmatrix} b_n \\ d_n \end{pmatrix} = \begin{pmatrix} J_n'(ka) \\ J_n(ka) \end{pmatrix}. \tag{3.37}$$

For S-polarization, the continuity conditions for the tangential components of electric and magnetic fields at the cylinder surface yield the following system of equations for the coefficients $a_n$ and $c_n$:

$$\begin{pmatrix} H_n^{(1)\prime}(ka) & J_n'(ska) \\ H_n^{(1)}(ka) & s J_n(ska) \end{pmatrix} \times \begin{pmatrix} a_n \\ c_n \end{pmatrix} = \begin{pmatrix} J_n'(ka) \\ J_n(ka) \end{pmatrix}. \tag{3.38}$$

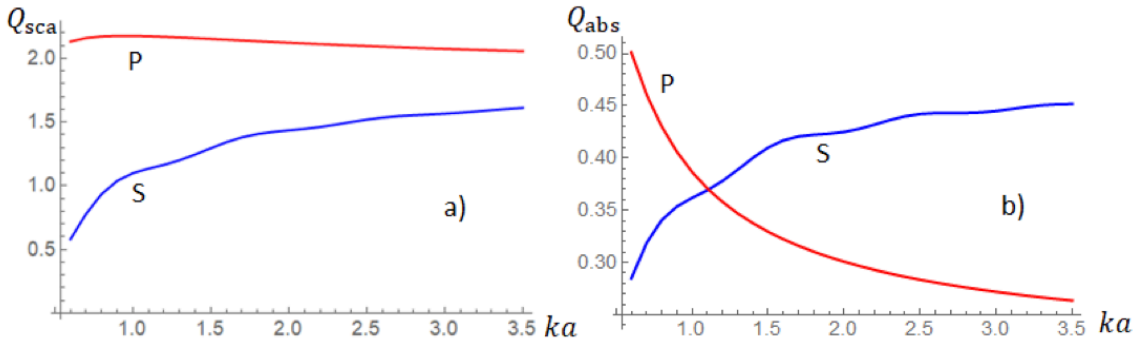


Figure 3.2: Dependence of the efficiency factors for scattering (a) and absorption (b) for the p (red) and s (blue) polarized light on the radius of a homogeneous cylinder. Dielectric permittivity is given by Eq. (3.39) with $\omega_{pe}/\omega = 6$ and $\nu_{ei}/\omega = 1$.

In what follows we consider the dielectric permittivity in the form

$$\epsilon = 1 - N(r)\,(\omega_{pe}/\omega)^2/[1 + i\, N(r)\,\nu_{ei}/\omega], \tag{3.39}$$

where $\omega_{pe}$ and $\nu_{ei}$ represent the electron plasma frequency and electron collision frequency at the cylinder axis, respectively, and $N(r)$ is a dimensionless function that describes the density profile in the cylinder. For a homogeneous cylinder, $N(r)$ is a Heaviside function:

$$N(r) = \begin{cases} 1 & \text{if } r \le a \\ 0 & \text{if } r > a \end{cases} \tag{3.40}$$

An illustration of the dependence of the scattering and absorption efficiency factors on the radius of a homogeneous cylinder is shown in Figure 3.2 for $\omega_{\rm pe}/\omega = 6$ and $\nu_{\rm ei}/\omega = 1$. The scattering factor is greater for P-polarization and increases with the radius for both polarizations. The absorption factor is greater for P-polarization when $ka$ is small, and it decreases as $ka$ increases. In contrast, the absorption factor for S-polarization increases with the radius. As the electromagnetic wave penetrates deeper into the cylinder, the absorption factor becomes greater since it is proportional to the electron collision frequency and increases as the cylinder density decreases. The scattering factor, on the other hand, is less dependent on the collision frequency and the density.

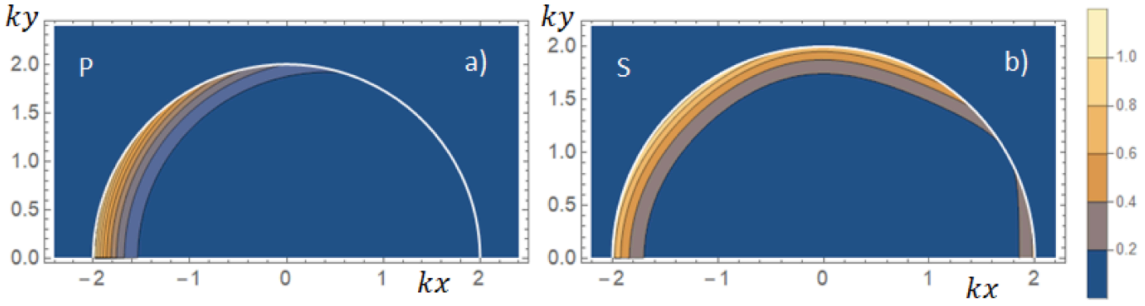


Figure 3.3: Laser power deposition over the volume of the cylinder, $W_{\rm abs} = (\omega/4\pi)\,{\rm Im}\,\epsilon\,|\mathbf{E}|^2$, normalized by $kI_0$ for the case of P (a) and S (b) polarization for $\omega_{\rm pe}/\omega = 6$ and $\nu_{\rm ei}/\omega = 1$. White circle shows the position of cylinder boundary, $ka = 1.5$. Laser comes from the left.

A difference between absorption rates for P and S polarization is further presented in Figure 3.3, which shows the distribution of absorbed power, $W_{\rm abs} = (\omega/4\pi)\,{\rm Im}\,\epsilon\,|\mathbf{E}|^2$, throughout the cylinder volume. The absorption is concentrated in a narrow skin layer on the front side of the cylinder, and the absorption rate is similar for both polarizations. However, the difference lies in the larger extent of the absorption zone to the sides of the cylinder in the case of S-polarization, due to the normal component of the laser electric field.

Angular distribution of the scattered light $I(\theta) = |T(\theta)|^2/\pi\overline{|T|^2}$ is shown in Figure 3.4. For narrow cylinders, there is a notable difference in the angular distributions, which arises from the interference of the angular harmonics. However, for large values of $ka$, scattering is dominated in the forward direction for both polarizations.

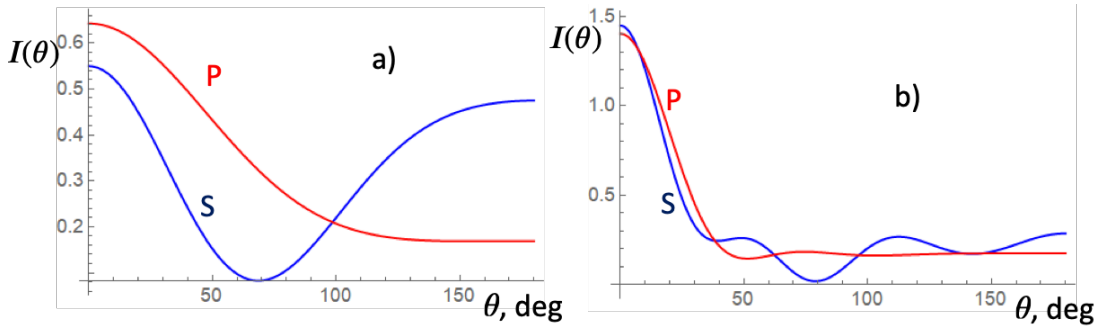


Figure 3.4: Angular distribution of the scattered light from a cylinder of radius, $ka = 1$ (a) and 3 (b) for the case of P (red) and S (blue) polarization. Dielectric permittivity is given by Eq. (3.39) with $\omega_{\rm pe}/\omega = 6$ and $\nu_{\rm ei}/\omega = 1$.

### 3.3.1 Laser absorption and scattering from a radially inhomogeneous cylinder

Here, we consider a representative case of a bell-shaped density profile

$$N(r) = \exp\left[-(r/a)^p \ln 2\right], \tag{3.41}$$

where parameter $p$ controls the steepness of the density profile and $a$ is the cylinder radius at a half of density maximum. The dielectric function is given by Eq. (3.39). Solution to Eqs. (3.10) and (3.11) is found numerically by using Wolfram Mathematica package [139]. In difference from a homogeneous cylinder, there is now the possibility for plasma resonance, $\omega = \omega_{\rm pe}(r)$, which has a strong effect on absorption of the S-polarized wave where the normal component of the electric field, $E_r$ is present. This effect is demonstrated in Figure 3.5 showing the shape of zone of energy deposition $W_{\rm abs} = (\omega/4\pi)\,{\rm Im}\,\epsilon\,|\mathbf{E}|^2$ for the case of a Gaussian density profile corresponding to $p = 2$ in Eq. (3.41).

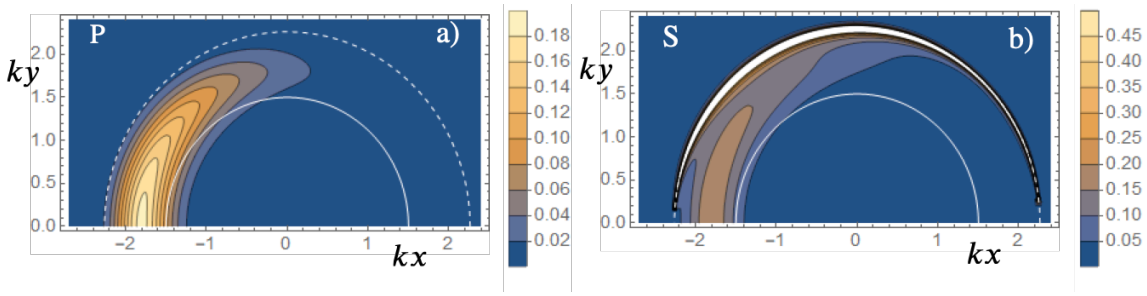


Figure 3.5: Map of the laser energy deposition $W_{\rm abs}/kI_0$ at normal incidence for a Gaussian density profile ($p = 2$) in a cylinder of radius $ka = 1.5$ for the case of P (a) and S (b) polarization for $\omega_{\rm pe}/\omega = 6$ and $\nu_{\rm ei}/\omega = 1$. White circle shows the position of effective radius, $r = a$ (solid line), and the critical density, ${\rm Re}\,\epsilon = 0$, dashed line.

In contrast to the case of a homogeneous cylinder shown in Figure 3.3, the energy deposition zone is displaced to the low-density plasma. In the case of P-polarization, the

zone of absorption is situated between the critical density and the cylinder effective radius as a trade-off between the screening of the laser field in the evanescent zone and the increase of the collision frequency. In the case of S-polarization, the energy deposition is much larger and the maximum is shifted to the critical density. This figure demonstrates the efficiency of resonance absorption, which is a transformation of the laser electromagnetic wave into a longitudinal electron plasma oscillations. This collisionless process does not exist in the case of a homogeneous cylinder, but it becomes a dominant process when the density scale length is larger than the skin depth.

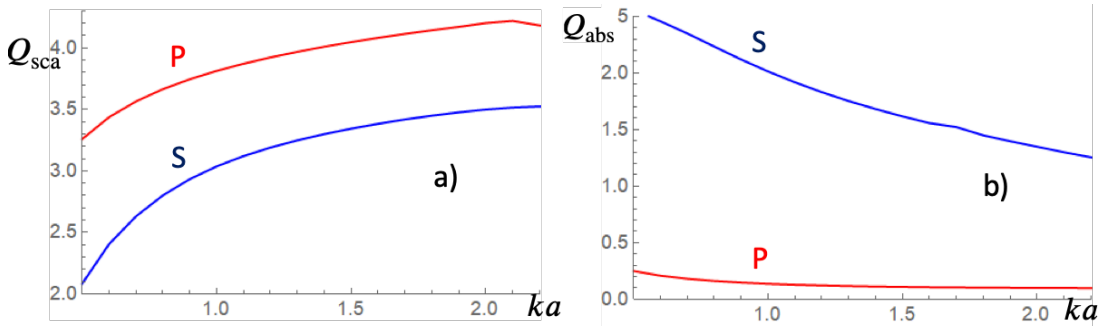


Figure 3.6: Dependence of the efficiency factors for scattering (a) and absorption (b) for the p (red) and s (blue) polarized light on a radius of a cylinder with a Gaussian density profile $p = 2$. Dielectric permittivity is given by Eq. (1.69) with $\omega_{pe}/\omega = 6$ and $\nu_{ei}/\omega = 1$.

The role of density inhomogeneity on the laser scattering and absorption is further evidenced in Figure 3.6 showing the dependence of the efficiency factors on the radius of the cylinder having a Gaussian density profile. Compared to similar graphs shown in Figure 3.2 for the case of a homogeneous cylinder, both scattering and absorption factors are increased in the case of S-polarization. By contrast, the absorption efficiency is decreased in the case of P-polarization. An increase of the scattering efficiency for both S and P-polarization is explained by the fact that the radius of opaque zone is larger than the effective cylinder radius.

The increase of absorption in the case of S-polarization is a consequence of the plasma resonance. This is confirmed by calculation of the dependence of $Q_{abs}$ on the electron collision frequency. In the case of P-polarization, absorption efficiency is proportional to the electron collisional frequency. It decreases in an inhomogeneous cylinder because laser field cannot reach the center of cylinder and absorption takes place at a lower density. By contrast, the S-polarization absorption efficiency increases due to the efficient resonance absorption near the critical density layer. It is independent on the collision frequency and depends weakly on the cylinder maximum density and the profile steepness. Angular distribution of the scattered light shown in Figure 3.7 depends weakly of the cylinder density profile and is very similar to the case of a homogeneous cylinder shown in Figure 3.4.

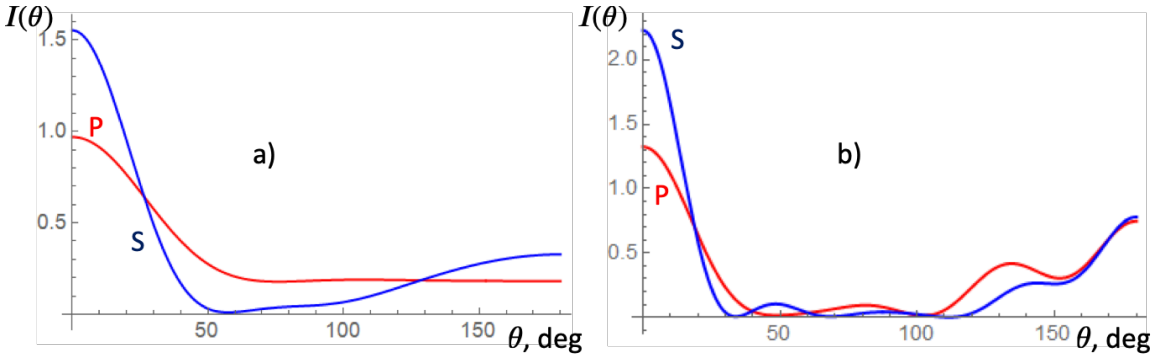


Figure 3.7: Angular distribution of the scattered light from a cylinder of radius with a Gaussian density profile $p = 2$, $ka = 1$ (a) and 3 (b) for the case of P (red) and S (blue) polarization. Dielectric permittivity is given by Eq. (1.69) with $\omega_{\rm pe}/\omega = 6$ and $\nu_{\rm ei}/\omega = 1$.

Absorption efficiency presented in Figure 3.6 can be compared with the estimate given in Appendix 3 in Ref. [36], where no polarization was specified and the authors assumed total absorption of the laser light incident within the distance smaller than the position of the critical density. For a cylinder having a Gaussian density profile, this hypothesis corresponds to the value $Q_{\rm abs} = (\ln(\omega_{\rm pe}/\omega)^2/\ln 2)^{1/2} = 2.3$, which is larger that the one shown in Figure 3.6(b).

### 3.3.2 Resonance absorption

A contribution of the plasma resonance to the laser absorption can be described as follows. Total energy absorption can be calculated as an integral of $W_{\rm abs}$ over the cylinder cross section. By taking an integral over the azimuthal angle and dividing by the geometric cross section, we obtain the following expression for the absorption efficiency factor:

$$Q_{p,\rm abs} = \frac{\pi}{ka}\int_0^\infty \rho\, d\rho\, \mathrm{Im}\,\epsilon \sum_n |u_n|^2\,, \quad Q_{s,\rm abs} = \frac{\pi}{ka}\int_0^\infty \rho\, d\rho\, \frac{\mathrm{Im}\,\epsilon}{|\epsilon|^2}\sum_n \left(|v_n'|^2 + \frac{n^2}{\rho^2}\,|v_n|^2\right).$$

In difference from $Q_{p,\rm abs}$, which just proportional to the imaginary part of dielectric permittivity, $Q_{s,\rm abs}$ contains in addition the absolute value of dielectric permittivity in the denominator. So, the integral over the resonance $\mathrm{Re}\,\epsilon(\rho_{\rm res}) = 0$, assuming $\mathrm{Im}\,\epsilon(\rho_{\rm res}) \ll 1$, can be taken analytically:

$$\int_0^\infty \rho\, d\rho\, \frac{\mathrm{Im}\,\epsilon}{|\epsilon|^2} \approx \frac{\rho_{\rm res}}{|d\mathrm{Re}\,\epsilon/d\rho|}\int d\mathrm{Re}\,\epsilon\, \frac{\mathrm{Im}\epsilon}{\mathrm{Re}\,\epsilon^2 + \mathrm{Im}\,\epsilon^2} = \frac{\pi\rho_{\rm res}}{|d\mathrm{Re}\,\epsilon/d\rho|}.$$

It does not depend on the collision frequency, in contrast to the case of a homogeneous cylinder. The resonance absorption is inversely proportional to the derivative of $\epsilon$ in the resonant point and it is decreases as the steepness of the cylinder density profile increases. This is shown in Figure 3.8, where the integrands in $Q_{p,\rm abs}$ and $Q_{s,\rm abs}$ are

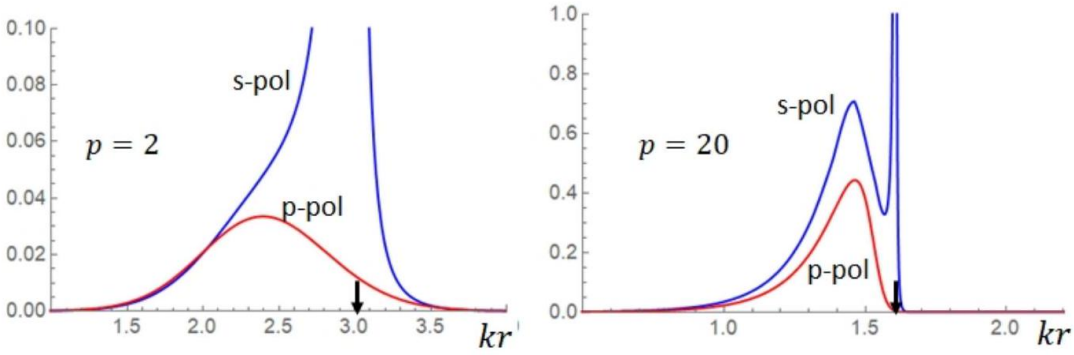


Figure 3.8: Radial distribution of the laser energy deposition at normal incidence for a Gaussian density profile ($p = 2$, left) and a steep profile with $p = 20$ (right) in a cylinder of radius $ka = 1.5$ for the electromagnetic wave of P (red) and S (blue) polarization, for $\omega_{\rm pe}/\omega = 6$ and $\nu_{\rm ei}/\omega = 1$.

plotted for two scenarios: a Gaussian density profile $p = 2$ and a steep profile with $p = 20$. For the P-polarization, the energy deposition curve has a simple bell-like shape in both cases, corresponding to collisional absorption in the bulk. However, for the S-polarization, the energy deposition curve is more complex. It includes two contributions: collisional absorption in the bulk and resonance absorption at the critical density. The two contributions are clearly separated in the case of a steep profile, $p = 20$, but overlap in the case of a Gaussian profile.

To demonstrate dependence of absorption and scattering on the steepness of the density profile, we show in Figure 3.9 distribution of the absorbed energy across the cylinder cross section for a steep density profile $p = 20$. In the case of a steep density profile, the energy deposition occurs at the front edge of the cylinder for the P-polarization and at the flanks of the cylinder for the S-polarization, which agrees well with the energy deposition in a homogeneous cylinder. On the other hand, for a Gaussian density profile shown in Figure 3.5, the energy deposition zone shifts to a lower density plasma. For P-polarization, the absorption zone is between the critical density and the effective radius of the cylinder, while for S-polarization, the maximum absorption occurs at the critical density. This indicates that resonance absorption, which is not present in a homogeneous cylinder, becomes the dominant process.

Figures 3.6a and 3.10a illustrate a comparison between the absorption efficiency factors for two different density profiles, a Gaussian profile with $p = 2$ and a steeper profile with $p = 20$, for the same parameters. The results show that for a steep density profile, the absorption efficiency factor is similar to that of a homogeneous cylinder. However, for a smoother density profile, the absorption efficiency factor increases by approximately two times. This outcome is expected because the wave energy is deposited near the critical density at a radius approximately two times larger than $a$.

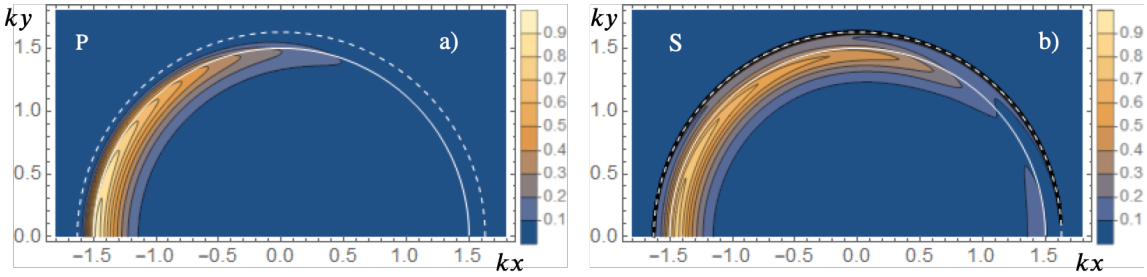


Figure 3.9: Map of the laser energy deposition $W_{\rm abs}/kI_0$ at normal incidence for a steep density profile ($p = 20$) in a cylinder of radius $ka = 1.5$ for the case of P (a) and S (b) polarization for $\omega_{pe}/\omega = 6$ and $\nu_e/\omega = 1$. White circle shows the position of effective radius, $r = a$ (solid line), and the critical density, $\mathrm{Re}\,\epsilon = 0$, dashed line.

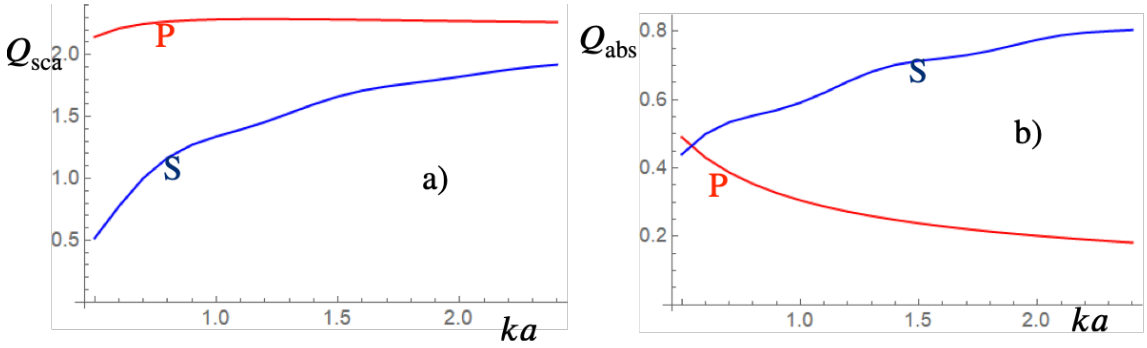


Figure 3.10: Dependence of the efficiency factors for scattering (a) and absorption (b) for the p (red) and s (blue) polarized light on a radius of a cylinder with a steep density profile $p = 20$. Dielectric permittivity is given by Eq. (1.69) with $\omega_{\rm pe}/\omega = 6$ and $\nu_{\rm ei}/\omega = 1$.

## 3.4 Conclusion for Chapter 3

Theoretical analysis of the laser interaction with a sub-wavelength cylinder shows a strong dependence on the laser polarization and density profile of the cylinder. The results show that the assumption that the absorption cross section is equal to the geometrical cross section leads to a severe overestimate of the absorption rate. In Section 4, by using detailed 2D PIC simulations, we confirm the analytical theory and consider the temporal evolution of the plasma in the pore due to expansion and ablation of solid element due to laser absorption.

We extend the Mie theory to the case of hot plasma and intense laser pulse. We determine the efficiency factors $Q_{\rm abs}$ and $Q_{\rm sca}$ in function of the cylinder dielectric permittivity and the dimensionless radius $ka$. This theory can be directly applied to simulations described in Section 4 by extracting required parameters such as density and temperature, as described in Section 4.2.1. The $Q$ factors calculated for the simulation parameters are shown in Section 4.5.

Our analysis of laser absorption in small high density cylinders leads to several con-

clusions:

- In a homogeneous cylinder, absorption cross section weakly depends on the laser polarization and angle of incidence. Electron collisions are responsible for absorption, which decreases as the imaginary part of the dielectric permittivity decreases. For a collision frequency appropriate to our interaction conditions, the absorption cross section is of the same order as the geometric cross section, and the typical absorption efficiency factor is about 0.5, but it decreases dramatically with a decrease in collision frequency.

- For cylinders with a radially inhomogeneous density, the absorption cross section is larger than that of a homogeneous cylinder with the same geometric cross-section. This is due to two reasons: collisional absorption occurs at distances where density is above the critical density, and the radius of critical density is larger than the geometrical radius, leading to an increase in the absorption cross-section. Additionally, an absorption due to the plasma resonance, which is not considered in the case of a homogeneous density, contributes to the increase in absorption. Resonance absorption is proportional to the value of the component of electric field parallel to the density gradient and does not depend on the imaginary part of the dielectric permittivity. For Gaussian density profiles, resonance absorption is responsible for over 90% of the absorption cross section.

- Resonance absorption occurs in the case of S-polarization at any angle of incidence and in the case of P-polarization at oblique incidence. Taking an average over laser polarization and angle of incidence, we can assume the absorption efficiency factor to be in the range of $Q_{\text{abs}} \sim 1.5 - 2$.

# Chapter 4

# Numerical simulations of laser interaction with under-dense foams

This chapter focuses on the use of Particle-in-Cell simulations to study the kinetics of plasmas in foam targets. We confirmed and evaluated the characteristics of laser interaction with sub-wavelength cylinders predicted by the analytic theory using the Smilei code [116], a massively parallel fully relativistic electromagnetic particle-in-cell simulation tool, which is described in detail in Section 2.

## 4.1 Setup of numerical simulations

Simulations for both laser polarizations at normal incidence are performed in a two-dimensional geometry in the plane $x$, $y$ perpendicular to the cylinder axis as it shown in Figure 3.1. The size of a square computing box $l_p$ was chosen such that the plasma density after the cylinder ablation and expansion is smaller than the critical density, which is the case of under-dense foams. Boundary conditions are open for electromagnetic waves in the propagation direction $x$ and reflecting in the transverse direction $y$. Boundary conditions for the particles are reflecting. The number of particles per cell is 1000, which is sufficient for resolving the processes of interest. The simulations are performed for the cases of P and S-polarization with electron–ion collisions taken into account including non-ideal effects [118] in a cold and dense material of cylinder. The case with ion-ion collisions is considered only for S-polarization. Ionization is not considered, and ion charge is taking a constant value.

We simulate the interaction of an incident plane wave with constant intensity, $I_0 = 10^{14}$ W/cm$^2$, at a wavelength of $\lambda = 0.35\,\mu$m. The initial radius of the cylinder is $a_0 = 0.1$ $\mu$m, corresponding to $ka_0 = 1.8$, and the density is $\varrho_s = 1$ g/cm$^3$, resulting in an electron density ratio of $n_e/n_{\rm cr} \simeq 35$ and $\omega_{\rm pe}/\omega \simeq 5.9$, assuming an ion effective charge

of $Z_{\text{eff}} = 4.54$ and atomic mass $A_{\text{eff}} = 8.73$. These parameters correspond to the TMPTA plastic foams used in experiments [31], [38], [140]. The size of the computational box is $L_x = L_y = l_p = 2.7\,\mu$m, the time step is $dt = 0.02\,\lambda/c$, and the cell size $dx = 0.03\,\lambda$ is smaller than the skin depth of the laser field penetration in a cylinder. The initial electron and ion temperatures are set to $T_e = T_i = 1$ eV. An additional simulation is performed without the laser pulse to evaluate the role of cylinder expansion at the initial temperature. The simulation results are analyzed in the following order: particle density and energy evolution and then the laser energy absorption and scattering.

The particle distribution energy functions in this section are fitted by a combination of power and exponential functions,

$$f_h(\varepsilon) = \frac{n_h}{T_h^{k+1}\Gamma(k+1)}\varepsilon^{k_h}\exp\left(-\frac{\varepsilon}{T_h}\right), \tag{4.1}$$

where $n_h$ is the number of hot particles ($h = e, i$) with respect to the total number of particles in the simulation box and $\Gamma(z)$ is the gamma function:

$$\Gamma(z) = \int_0^\infty dt\, e^{-t}\, t^{z-1}. \tag{4.2}$$

## 4.2 Plasma density distribution

Figure 4.1 displays the cylinder density distribution at three time moments of 1.6, 10.9, and 15.6 ps for the S-polarization case. At $t = 1.6$ ps (panel a), a rarefaction wave is formed at the cylinder edge and propagates towards the center. This wave converges to the cylinder axis at $t \simeq 11$ ps (panel b), causing a decrease of the maximum plasma density at later times due to the cylinder expansion. Despite the asymmetric absorption shown in Figure 3.5, the cylinder maintains its axial symmetry, and its shape can be approximated with a two-parameter exponential function given by Eq. (3.41) and a central density $\varrho_c$. This quasi-symmetric expansion is due to lateral electron transport, which spreads the absorbed energy over the cylinder surface.

The simulation results for the P-polarization case shown in Figure 4.2 present similar density distributions but delayed in time. The convergence of rarefaction wave occurs at a time $t \simeq 15 - 16$ ps (panel d). This slower temporal evolution indicates a smaller absorption of the P-polarized laser compared to the S-polarized one.

### 4.2.1 Parametrization of plasma density distribution

To construct a model of the evolution of the cylinder density profile, we use a non-linear least square minimization approach with a function $\rho_c N(r)$, where $N$ is defined

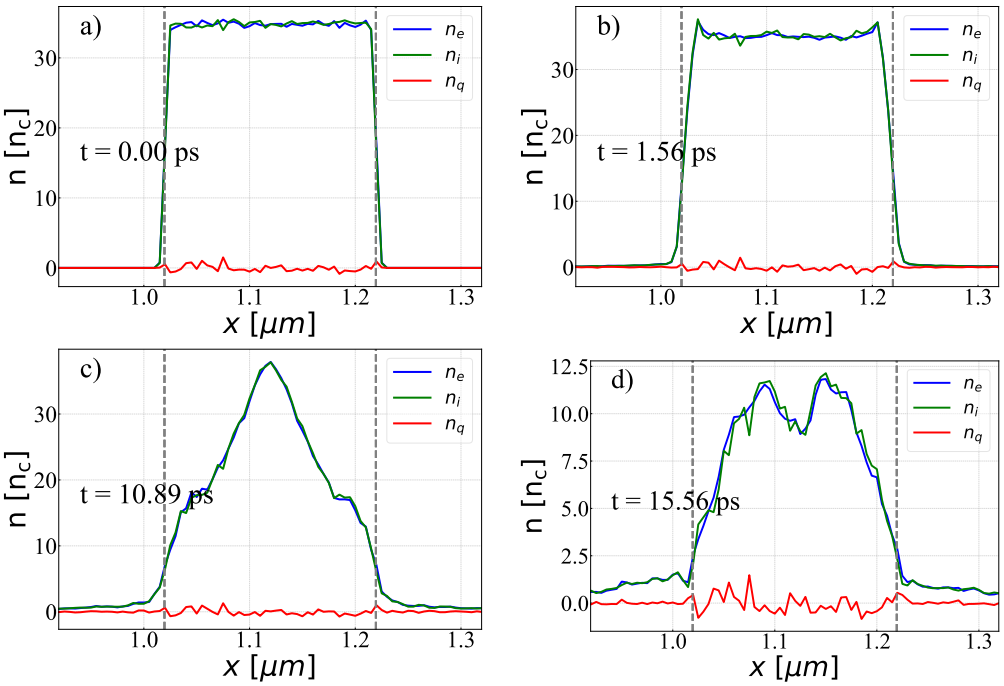


Figure 4.1: Cut of the electron (blue), ion (green) and charge (red) density along the $x$ axis through the center of the cylinder $y = 1.35$ at time 0.0 ps (a), 1.6 ps (b), 10.9 ps (c) and 15.6 ps (d), in the case of S-polarization. Dashed gray lines mark the initial position of a cylinder. Simulation parameters are given in the text; Laser propagates from the left to the right.

by Eq. (3.41). It contains three time-dependent parameters: the on-axis density $\rho_c$, the width of the profile at a half maximum $a$, and the steepness factor $p$ that varies with time from very large values at earlier times ($t \leq 2$ ps) to intermediate values ($p \sim 2 - 4$) at later times.

Figure 4.3 schematically shows the accuracy of parametrization, where the coordinate $x_c = x - L_x/2$ is defined with respect to the center of the simulation box. This parametrization is useful for calculation of the total cylinder mass (4.3) and defining the ablation and expansion velocities discussed in Section 4.4.

The time-dependent nature of these parameters is shown in Figure 4.4(a-c) for both P and S-polarization cases. The evolution of the cylinder can be separated into two distinct phases. In the first phase, lasting about 8 ps, the cylinder radius decreases by approximately 30%, and the power index of the density profile decreases significantly to $p \simeq 2 - 4$, while the central density remains constant. This phase corresponds to the converging rarefaction wave moving from the edge of the cylinder to its center, as demonstrated by the density profiles shown in Figure 4.1. In the case of S-polarization, the cylinder radius decreases even more due to the involvement of the ablation process in addition to the converging rarefaction wave.

The estimated velocity of the converging wave is about $2-4$ nm/ps, in agreement with

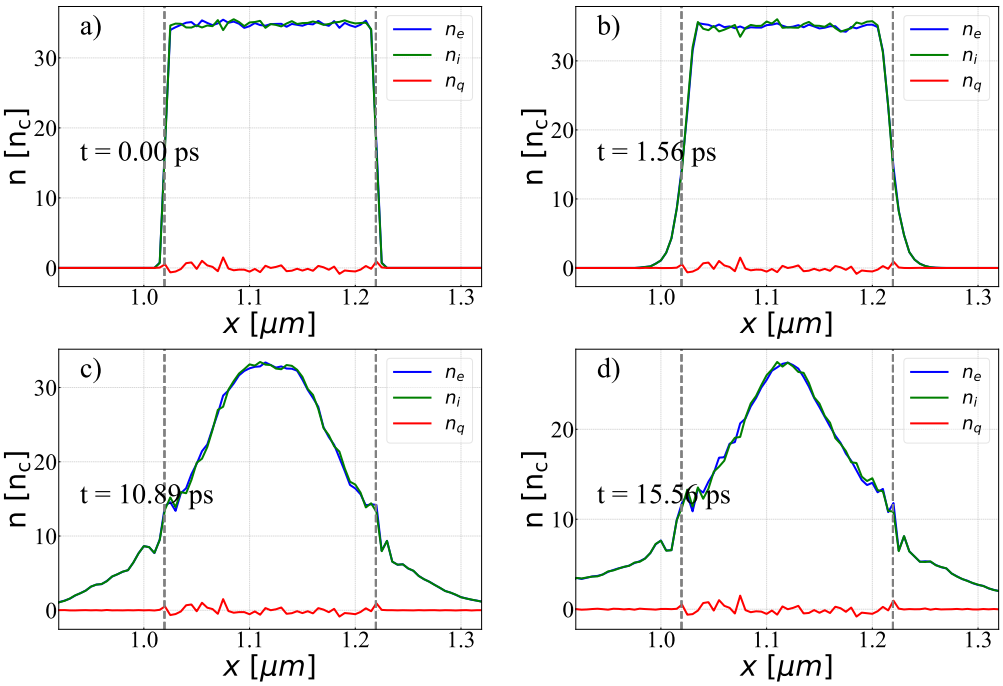


Figure 4.2: Cut of the electron (blue), ion (green) and charge (red) density along the $x$ axis through the center of the cylinder $y = 1.35$ at time 0.0 ps (a), 1.6 ps (b), 10.9 ps (c) and 15.6 ps (d), in the case of P-polarization. Dashed gray lines mark the initial position of a cylinder. Simulation parameters are given in the text; Laser propagates from the left to the right.

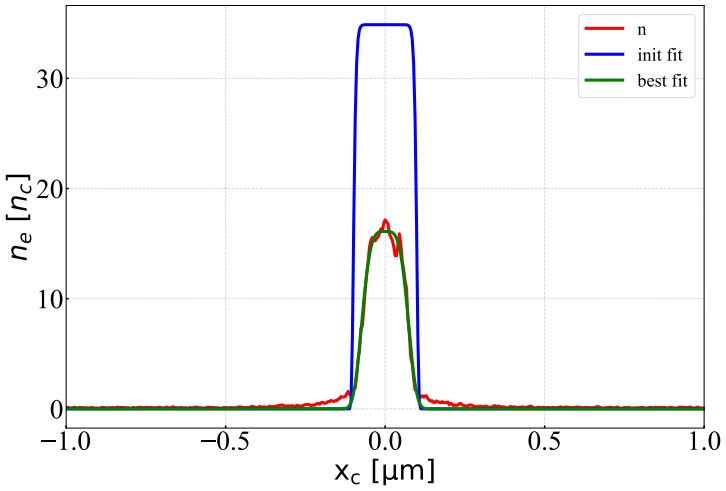


Figure 4.3: Parametrization of plasma density using a non-linear least square minimization method with a function $\rho_c N(r)$. The red line represents the plasma density at $t = 14$ ps, the green line represents the fitted plasma density, and the blue line represents the initial ($t = 0$ ps) plasma distribution. The initial density is $\varrho_s = 36\varrho_{\mathrm{cr}}$.

the acoustic velocity at a cylinder temperature of approximately 1 eV (see Section 4.3 for temperature evaluation). After 8 ps, the second phase commences, where the cylinder undergoes rapid expansion accompanied by a fast decrease in the central density and an increase in the cylinder radius. This phase is observed in both P and S-polarization cases.

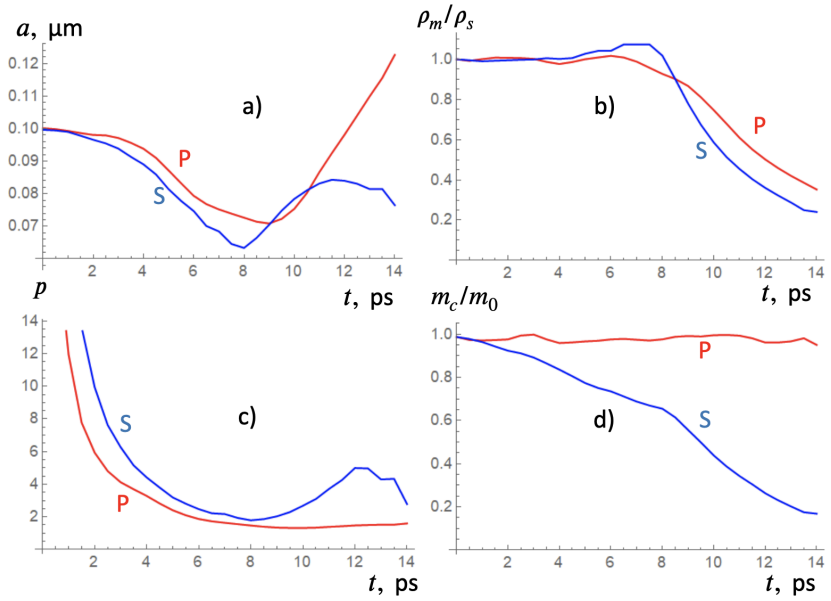


Figure 4.4: Temporal evolution of the parameters characterizing the cylinder density profile in the case of S (blue) and P (red) polarization: (a) radius $a$, (b) maximum density $\varrho_m$ normalized to the initial density $\varrho_s$, (c) power factor $p$ and (d) mass $m_c$ normalized to the initial mass $m_0 = \pi a_0^2 \varrho_s$. Initial density $\varrho_s = 36\,\varrho_{\mathrm{cr}}$.

There is, however, a significant difference in the cylinder mass evolution, which is shown in Figure 4.4a-c. It is defined as

$$m_c = 2\pi \int_0^\infty \varrho(r)\, r\, dr = \pi a^2 \varrho_c g(p), \tag{4.3}$$

where $g(p) = \Gamma(1 + 2/p)\,(\ln 2)^{-2/p}$ and $\Gamma$ is the gamma function defined in (4.2).

For P-polarization, the cylinder mass remains constant with time, whereas for S-polarization, the mass continuously decreases, indicating ablation induced by laser absorption at the surface. Approximately 80% of the plasma is estimated to have been ablated during the 14 ps period, as confirmed by using the particle energy distribution function described in Section 4.3. In Section 4.4, we evaluate the relative contributions of the ablation and expansion processes.

## 4.3 Particle energy evolution

The processes of ablation and expansion of the cylinder are further analyzed by considering distribution of electrons and ions on energy and in space. Figure 4.5 presents evolution in time of the distribution of average energy of electrons and ions along the $x$ axis, which

is defined as:

$$\bar{\varepsilon}(x) = \left[\int_{\Delta y} dy \int_0^{\varepsilon_{\max}} d\varepsilon\, f(\varepsilon)\right]^{-1} \cdot \int_{\Delta y} dy \int_0^{\varepsilon_{\max}} d\varepsilon\, \varepsilon\, f(\varepsilon), \tag{4.4}$$

where $f(\varepsilon, x, y)$ is the energy distribution function of electrons or ions. The integral over $y$ is taken over a narrow strip of a width $\Delta y \sim 0.1\,\mu$m centered at the cylinder axis. Similar analysis has been performed in the perpendicular direction confirming a quasi-isotropic plasma expansion.

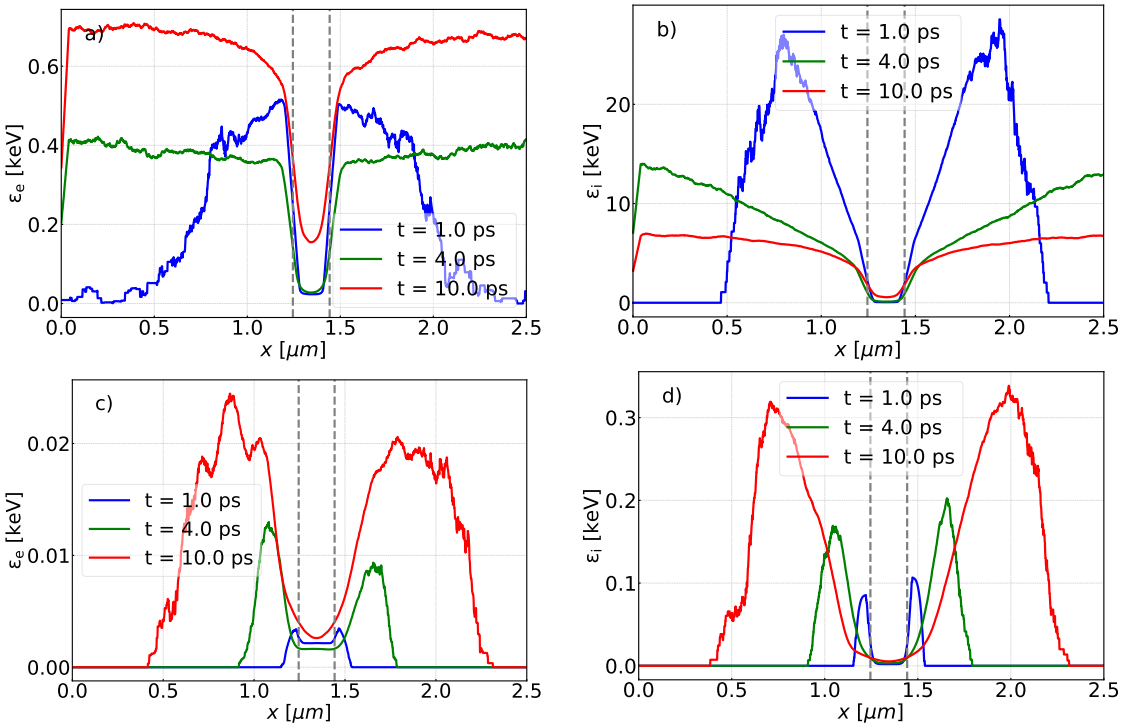


Figure 4.5: Cut of the electron (a, c), and ion (b, d) average energy along the $x$ axis through the center of the cylinder $y = 1.35$ at a time $t = 1.0$ ps (blue), $t = 4$ ps (green) and $t = 10$ ps (red) for the case of S (a, b) and P (c, d) polarization. Simulation parameters are given in the text. Dashed gray lines mark the initial position of a cylinder.

Figure 4.5 confirms that the cylinder expansion is quasi-neutral, the electrons and ions expand with the same average velocity. However, the average energies of electrons and ions are very different. In the case of P-polarization, the maximum ion expansion velocity of $\sim 50$ nm/ps at $t = 10$ ps corresponds to the kinetic energy of 120 eV, which is comparable with the average ion energy shown in Figure 4.5d. By contrast, the electron total energy in panel c) is much larger than the kinetic energy, which is $\sim 4$ eV at $t = 1$ ps. This fact indicates that plasma expansion is driven by the thermal energy of laser heated electrons. In the case of S-polarization, the average ion energy in Figure 4.5b is about $\sim 20$ keV at time of 1 ps. This value agrees with the ion expansion velocity estimated to be $\sim 0.8\,\mu$m/ps, thus confirming a much more efficient ion acceleration. This is attributed

to a laser absorption at the surface of cylinder. After 4 ps, the ablated plasma fills the pore and energy distribution of electrons and ions becomes homogeneous.

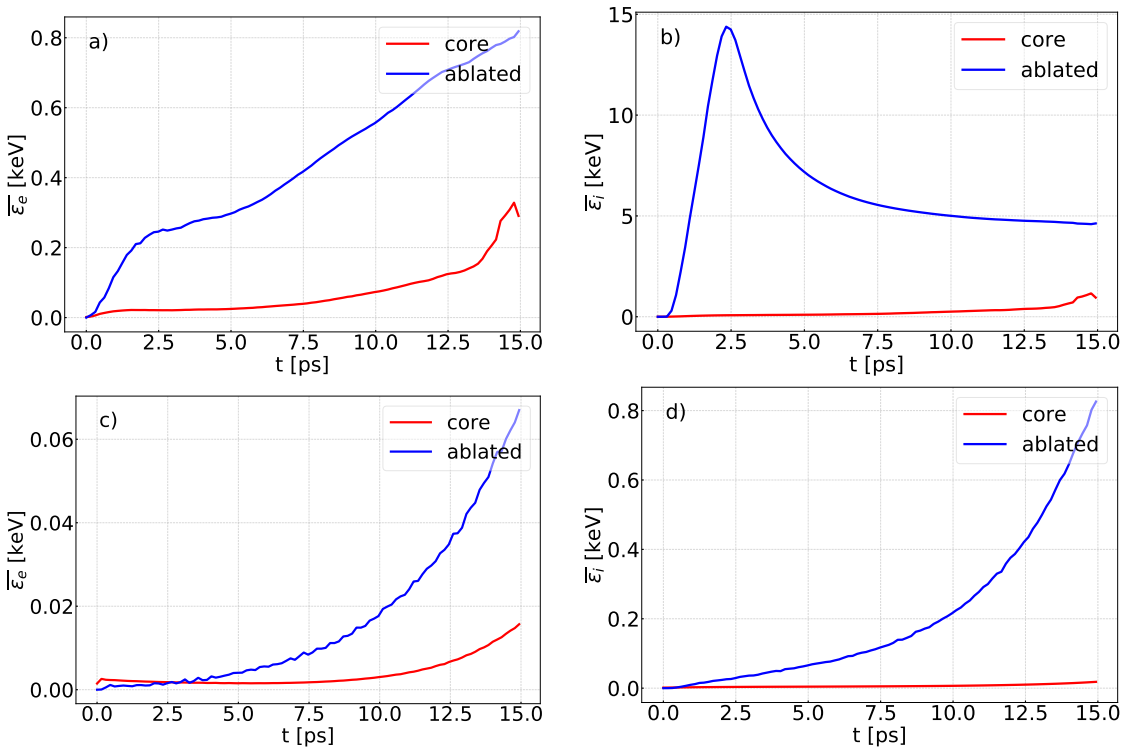


Figure 4.6: Time dependence of electron (a, c) and ion (b, d) energy averaged over the volume inside cylinder (red) and outside cylinder (blue) for the case of S (a, b) and P (c, d) polarization.

These observations are further confirmed in Figure 4.6 showing time dependence of electron and ion energies averaged over the cylinder (red) and outside the cylinder (blue) in the ablated plasma. The electron and ion energy dynamics in the case of P-polarization is consistent with the expansion process driven by laser heating of electrons in the bulk of cylinder. Laser absorption takes place in a narrow skin layer of thickness of $\sim 30$ nm at the surface of cylinder. It is proportional to the electron collision frequency. The energy transport inside the cylinder is suppressed due to a very large electron collision frequency, and the electron and ion temperatures in the cylinder remain very low for a long time of 10 ps or more.

In the case of S-polarization, absorption is dominated by the plasma resonance. In agreement with the theory, see Figure 3.6, absorption is much larger, and the absorbed energy is transferred from electrons to ions more efficiently by the ablation process at the surface of the cylinder. Ablated plasma fills the pore at $t \simeq 4$ ps and after that time reflected ions mix with incoming ions, thus converting their kinetic energy into internal energy. The ion energy is stabilized at a level of 5 keV, while the electron energy in the ablated plasma increases due to inverse Bremsstrahlung laser absorption.

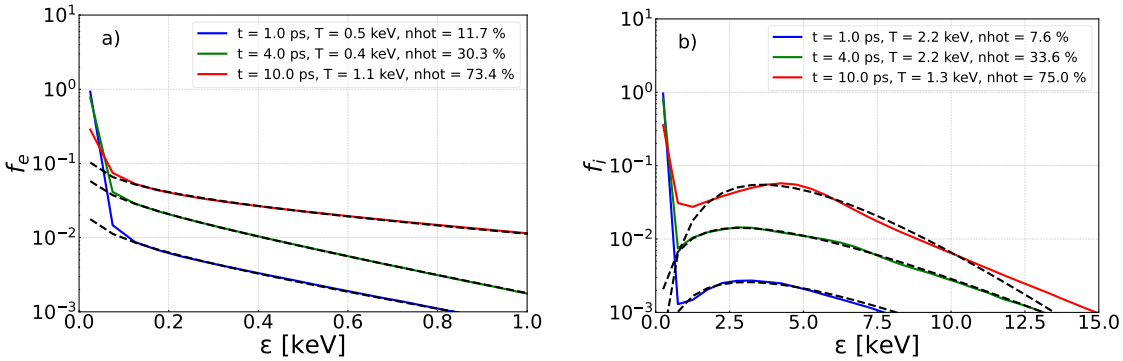


Figure 4.7: Distribution function of electrons (a) and ions (b) at a time $t = 1.0$ ps (blue), $t = 4.0$ ps (green) and $t = 10.0$ ps (red) for the case of S-polarization.

Particle distribution on energy in the hot ablated plasma is shown in Figure 4.7. It can be approximated by a combination of power and exponential functions (4.1). Fitted parameters for electrons and ions are shown in Table 4.1.

| $t$, ps | $T_e$, keV | $T_i$, keV | $n_e$, % | $n_i$, % | $k_e$ | $k_i$ |
|---|---|---|---|---|---|---|
| 1 | 0.5 | 2.2 | 11.7 | 7.6 | -0.3 | 1.4 |
| 4 | 0.4 | 2.2 | 30.3 | 33.6 | -0.3 | 1.3 |
| 10 | 1.1 | 1.3 | 73.4 | 75.0 | -0.4 | 2.8 |

Table 4.1: Fitting parameters for the distribution function of hot electrons and ions obtained in the simulation at 1 ps, 4 ps and 10 ps. The case of S-polarization. Simulation parameters are given in the text.

A slight difference between the number of hot electrons and ions at $t = 1$ ps indicates that some electrons are spatially localized in a narrow region at the periphery of the cylinder and create an electrostatic field accelerating ions. The hot electron distribution shown in Figure 4.7a is well-approximated by an exponential function and the temperature agrees with the data shown in Figure 4.6a.

The number of hot ions shown in Table 4.1 is in good agreement with the number of ablated ions shown in Figure 4.4d. Therefore, the ion distribution shown in Figure 4.7b represents all ablated plasma. The maximum of the ion distribution at $2.5 - 3$ keV indicates that a significant amount energy remains in the form of a radial flow. A decrease of effective temperature $T_i$ and increase of power index $k_i$ with time corresponds to the ion distribution being more peaked around the maximum with an average energy of $\bar{\varepsilon}_i = (k_i+1)T_i \approx 5$ keV independent of time. This value is in good agreement with the blue line in Figure 4.6(b). The simulation time of $10-15$ ps is shorter than the ion relaxation time. It is expected that the ion distribution function will converge to a Maxwellian function within the next $10 - 20$ ps due to the ion-ion collisions and flow-driven turbulence.

## 4.4 Characterization of the ablation/expansion process

By characterizing the cylinder density with three time-dependent parameters as discussed in Section 4.2.1, we can assess the relative roles of expansion and ablation processes. Taking the time derivative of the right hand side of Eq. (4.3) and using the definition of the ablation velocity:

$$v_{\rm abl} = -\frac{\dot{m}_c}{2m_c}a. \tag{4.5}$$

where $m_c$ is the cylinder mass (4.3), we can derive the time derivative of the cylinder radius as follows:

$$\dot{a} = -v_{\rm abl} - a\frac{\dot{g}}{g} - a\frac{\dot{\varrho}_c}{2\varrho_c} \equiv -v_{\rm abl} + v_{\rm exp}. \tag{4.6}$$

where $v_{\rm exp}$ represents the expansion velocity.

The ablation velocity steadily increases during the first 8 ps to 4 nm/ps, and it further increases to $10-12$ nm/ps at later time, see Figure 4.8. Interestingly, this ablation velocity corresponds to the mass ablation rate $\varrho_c v_{\rm abl} \simeq (5-10)\times 10^5$ g/cm$^2$s, which is in qualitative agreement with the theory of stationary laser ablation [2], [141] assuming laser absorption of $\sim 20\%$. However, in our case the process is strongly non-stationary and the plasma is accelerated over a distance smaller than $1\,\mu$m. By contrast, in the case of P-polarization, the ablation velocity is practically zero during the first 10 ps, and it slightly increases at later time.

The cylinder radius changes due to two processes, ablation and expansion. The ablation velocity is identified as the first term in the right-hand side of Eq. (4.6), while the last two terms in that equation represent the expansion velocity. Figure 4.8 shows the temporal evolution of the ablation and expansion velocities, which reveals two distinct regimes of cylinder expansion. During the first $7-10$ ps, the negative expansion velocity corresponds to the propagation of the rarefaction wave to the center of the cylinder, with a magnitude on the order of $2-4$ nm/ps, which is comparable to the cylinder expansion velocity without laser. At later times $t > 8$ ps, the expansion velocity increases to around $\sim 15$ nm/ps for S-polarization. However, because a significant fraction of the initial mass is spread out over the simulation cell, the definition of the cylinder radius at later times is less precise.

For S-polarization, the ablation process dominates throughout the simulation, which is consistent with a smaller homogenization time estimated as $t_h \simeq a_0/v_{\rm abl} \simeq 30$ ps. On the other hand, for P-polarization, the ablation velocity is negligible, and we estimate the homogenization time as the time for the cylinder to expand to the pore edges: $t_h \simeq l_p/2v_{\rm exp} \simeq 100$ ps.

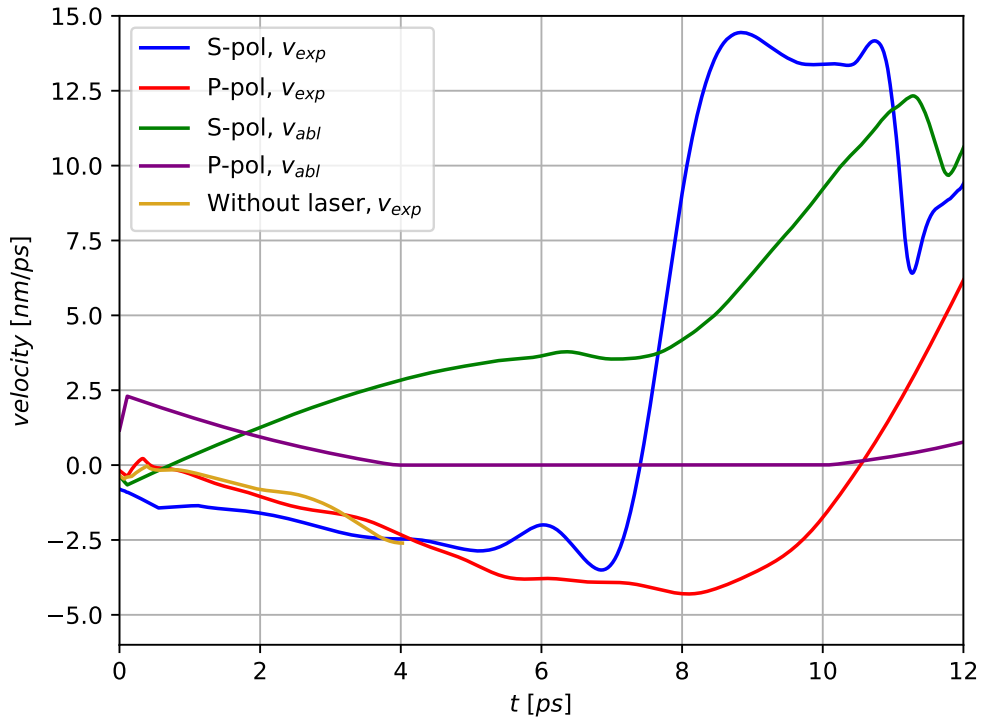


Figure 4.8: Temporal evolution of the ablation (green, purple) and expansion (blue, red) velocities in the case of S (blue, green) and P (red, purple) polarization. Golden curve represents expansion velocity for the case of pure (thermal) expansion without laser for the first 4 ps.

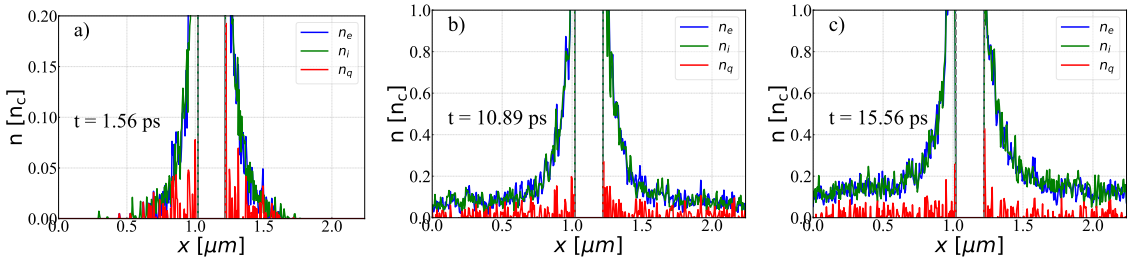


Figure 4.9: Cut of the electron density (blue), ion density (green) and absolute value of charge density (red) ablated plasma outside the cylinder along the $x$ axis at $y = 1.35$ at time 1.6 ps (a), 10.9 ps (b) and 15.6 ps (c), in the case of S-polarization. Simulation parameters are given in the text. Dashed gray lines mark the initial position of a cylinder.

Ablation of the cylinder is responsible for generating the ambient plasma within the pore. Figure 4.9 illustrates the plasma density distribution resulting from ablation at three different time intervals of 1.6, 10.9, and 15.6 ps for S-polarization. As time progresses, the plasma rapidly fills the pore outside the cylinder, leading to an increase in plasma density. The charge separation zone is localized near the cylinder, and it arises due to the electrostatic field that accelerates the ablated plasma.

The process of cylinder ablation is quasi-neutral, as evidenced by the negligible and

predominantly negative charge density $n_q = Zn_i - n_e$ (red line) shown in Figure 4.9 except at the boundary of the cylinder. The underlying mechanism of ion acceleration is associated with the electrostatic ablation [142], where the laser energy is transferred to electrons in the resonance layer at which the laser frequency matches the plasma frequency, as depicted in Figure 3.5. Due to the resonance enhancement of the incident laser field at this layer, electrons acquire a substantial amount of energy on the order of $\sim 0.5$ keV, see Figure 4.6a, and escape from the cylinder. The ions are then accelerated by the sheath electric field in a similar manner to the target normal sheath acceleration process [143], [144], which typically occurs at higher laser intensities.

The magnitude of the radial electrostatic field at the surface of the cylinder can be estimated based on the ion acceleration time and energy. According to Figure 4.5b, the ions gain an energy of $\varepsilon_i \sim 20$ keV in less than 0.5 ps while traveling a distance of $l_{\text{acc}} \sim 0.3, \mu$m from the cylinder. Hence, the velocity of these ions can be approximated to be $v_i \sim 0.7$ $\mu$m/ps, which corresponds to an energy of $\frac{1}{2}m_i v_i^2 \sim 20$ keV. The ion acceleration rate is $g = v_i/t_{\text{acc}} \sim 2 \times 10^{18}$ m/s$^2$, and this corresponds to an electrostatic field of $E_s = m_i g/Ze \simeq 40$ kV/$\mu$m, which is comparable to the laser electric field. This value is supported by another estimate based on the ion energy and acceleration length, which gives $E_s \simeq \varepsilon_i/Zel_{\text{acc}} \simeq 20$ kV/$\mu$m.

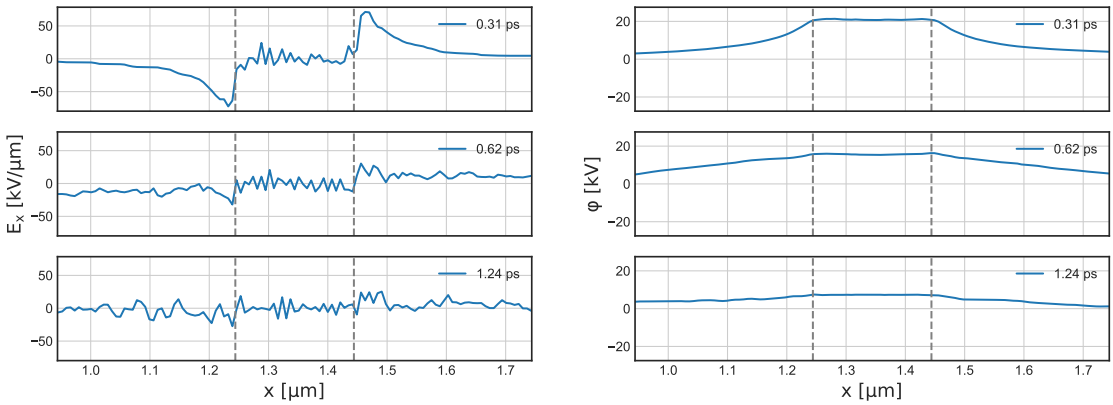


Figure 4.10: Cut of the electrostatic field $E_x$ (left) and corresponding potential $\varphi$ along the $x$ axis through the center of the cylinder $y = 1.35$ $\mu$m (right) at time $t = 0.31$ ps (top), $t = 0.62$ ps (middle) and $t = 1.24$ ps (bottom). Simulation parameters are given in the text.

The estimates presented above are consistent with the electrostatic field measured directly in the simulation, which is illustrated in Figure 4.10. The maximum value of the electric field is around 60 kV/$\mu$m and is confined to a region of 0.2 $\mu$m. The potential of the cylinder $\varphi$ reaches approximately $\simeq 10$ kV, which, for an ion charge of $Z = 4.5$, corresponds to an ion energy of $\varepsilon_i \simeq 40$ keV.

The electrostatic field responsible for ion acceleration is generated by electrons accel-

erated by the laser, which create a space charge. The thickness of the sheath layer is determined by the density profile of the cylinder, as illustrated in Figure 4.4, where the density scale length $L_\varrho = \varrho/|\varrho'| \simeq 15$ nm at $t \sim 1$ ps. To maintain this field, a characteristic electron energy is required, which can be obtained from the force balance equation, $eE_s + \varepsilon_e \partial_r \varrho/\varrho \simeq 0$. This equation yields an electron energy of $\varepsilon_e \sim eE_s L_\varrho \simeq 600$ eV. This energy range is consistent with the electron energy in the ablated plasma, as shown in Figures 4.5a and 4.6a. At the critical density, this electron temperature corresponds to the Debye length $\lambda_{\mathrm{De}}$ of a few nm, which is 10 times smaller than the density scale length. This estimate confirms that ion acceleration proceeds in the quasi-neutral regime, where $\lambda_{\mathrm{De}} \ll L_\varrho$. At later times, the cylinder density scale length increases faster than the electron temperature, resulting in a smaller energy for the accelerated ions.

## 4.5 Energy balance in the pore

Figure 4.11 shows the instantaneous distribution of the $x$-component of Poynting vector, $\mathbf{S} = (c/4\pi)\,\mathbf{E} \times \mathbf{H}$, in the simulation box for the case of S-polarization. The Poynting vector is modulated with a period of a half laser wavelength. The incident laser field before the cylinder is weakly perturbed, indicating a weak backscattering. Transmitted light shows modulations in the cone with opening angle of $\sim 30°$, which provides the characteristic angle of propagation of the scattered light. This angle is in qualitative agreement with the scattering diagram shown in Figure 3.4. The field is enhanced near the cylinder due to the interference of incident and scattered waves.

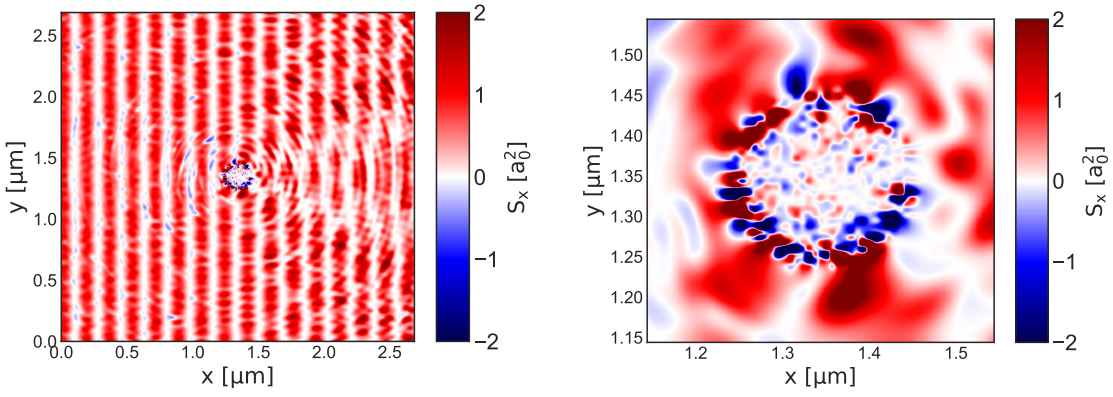


Figure 4.11: Top: distribution of the $x$-component of Poynting vector in the simulation box at time 0.02 ps. Case of S-polarization. Laser comes from the left. Bottom: zoomed part near the cylinder showing the interference of the incident and scattered light.

The energy balance in the simulation box is evaluated by measuring the laser reflection

$R$ and transmission $T$, which are defined as

$$R = 1 - \int dy \bar{S}_x(0, y)/I_0 l_p \quad \text{and} \quad T = \int dy \bar{S}_x(l_p, y)/I_0 l_p,$$

where $\bar{S}_x$ is the $x$-component of the Poynting vector averaged over the laser period and integral is taken over the transverse coordinate $y$. The time-averaged values of reflection and transmission are shown in Table 4.2.

| Pol. | Reflection | Transm. | Abs. | $Q_{\text{abs}}$ | $f_{\text{back}} Q_{\text{sca}}$ |
|---|---|---|---|---|---|
| S | 6% | 82% | 12% | 1.32 | 0.66 |
| P | 10% | 88% | 2% | 0.22 | 1.1 |

Table 4.2: Energy balance in the simulation averaged over a time interval of $7 - 15$ ps. Simulation parameters are given in the text.

These quantities can be related to the laser absorption and scattering cross sections on the cylinder. Laser absorption in the ablated plasma is small in the simulation and has been neglected in these estimates. A small level of reflection and a high level of transmission is explained by the fact that the geometrical cross section of the cylinder $2a$ is small in comparison to the box size $l_p$.

According to the theory presented in Section 3.2.1, the reflected light is due to laser scattering in the rear demi-sphere, $R = f_{\text{back}} Q_{\text{sca}} 2a/l_p$, where $f_{\text{back}}$ is the fraction of the total scattered light propagating at angles $\theta > \pi/2$, $2a$ is the geometrical cross section and $Q_{\text{sca}}$ is the scattering efficiency factor. The transmitted light is different from the incident due to absorption and backward scattering $T = 1 - (Q_{\text{abs}} + f_{\text{back}} Q_{\text{sca}}) 2a/l_p$. The factors $Q_{\text{abs}}$, $Q_{\text{sca}}$, $f_{\text{back}}$ and cylinder radius $a$ are calculated theoretically and compared with the simulation results for $R$ and $T$.

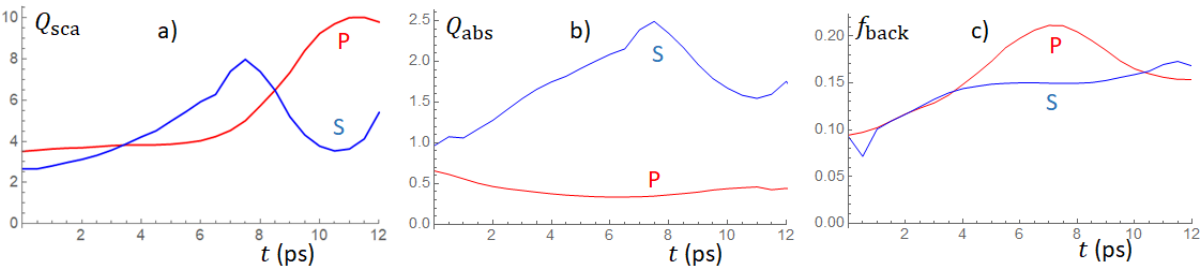


Figure 4.12: Temporal evolution of scattering (a), absorption (b) factors and the fraction of backscattered light (c) for the case of S (blue) and P (red) polarization calculated from the theory presented in Section 3.2.1 for the simulation parameters shown in Figure 4.4.

Furthermore, by using the model described in Section 4.2.1 and the interpolation of the cylinder density profile with the function (3.41), we calculate the actual time-dependent scattering and absorption efficiency factors along with the fraction of total backscattered

light $f_{\text{back}}$. As shown in Figure 4.12a,b, the scattering and absorption factors for the P-polarization case remain constant during the first 8 ps of the simulation time, indicating a slow temporal evolution and small absorption. In the case of S-polarization, both absorption and scattering factors are increasing with time during the first 8 ps. The increase of these factors is connected to the increase of effective surface where the absorption and scattering processes take place as the density profile becomes less steep.

The absorption coefficient $A = 1 - R - T = 12\%$ calculated in a homogenization stage for the case of S-polarization by using the parameters of the cylinder found in the simulation is in good agreement with the energy balance found in the numerical simulation.

## 4.6 Role of the ion-ion collisions

In this section, we discuss the importance of ion-ion collisions in foam plasmas and their role in understanding the homogenization process. As noted in Section 4.3, the simulation time of $10 - 15$ ps is shorter than the ion relaxation time. We expect the ion distribution function to converge to a Maxwellian function within the next $10 - 20$ ps due to ion-ion collisions and a flow-driven turbulence.

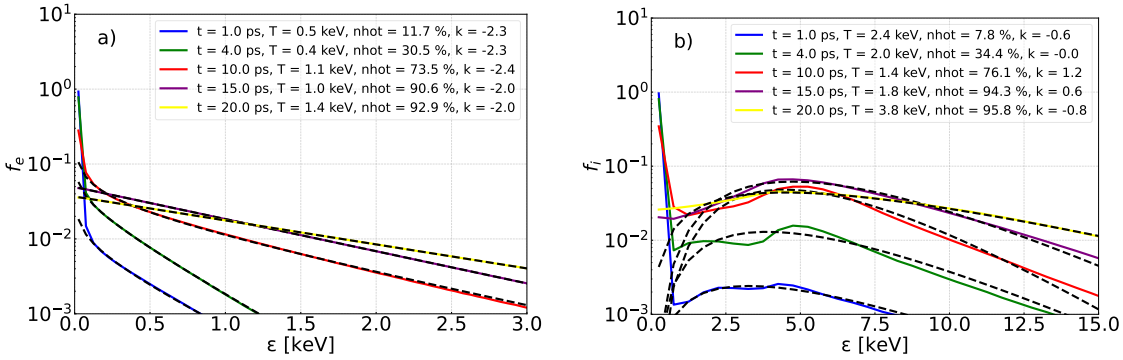


Figure 4.13: Distribution function of electrons (a) and ions (b) at a time $t = 1.0$ ps (blue), $t = 4.0$ ps (green) and $t = 10.0$ ps (red) for the case of S-polarization with ion-ion collisions included.

In foam plasmas, ions have a much higher temperature than electrons, resulting in a significant difference in the ion and electron mean free paths and delaying the energy relaxation. The ion mean free path is much shorter than the electron mean free path, emphasizing the crucial role of ion-ion collisions in such plasmas. These collisions lead to the thermalization of the ion energy distribution function, as shown in Figure 4.13, resulting in a more homogeneous ion population. The ion temperature, calculated by using the Maxwell two-temperature fit (4.1) described in Section 4.3, is estimated to be about 4 keV at $t = 20$ ps. Additionally, the collisional transfer momentum between ions leads to a more uniform ion velocity distribution. Thus, ion-ion collisions are essential

for the homogenization process in low-density porous plasmas. At a time $t = 15$ ps more than 90% of plasma was ablated and the average plasma density in the pore become sub-critical.

A comparison of Figures 4.7 and 4.13 shows that the initial conditions for the hot electrons and ions are similar, with comparable temperatures and populations during the first 10 ps. The ion temperature at $t = 10$ ps is 1.4 keV, similar to the value of 1.3 keV in Figure 4.7, and the ion population is 76%, slightly higher than the 75% in Figure 4.7. The electron temperature at $t = 10$ ps is 1.1 keV, which is similar to Figure 4.7, and the electron population remains the same. However, at later times, some differences are observed in the ion distribution function, indicating the importance of ion-ion collisions in modifying the distribution over time. The temperatures of hot electrons and ions at $t = 20$ ps are estimated to be 1.4 and 3.8 keV, respectively. The hot electron and ion populations at the same time of 20 ps are estimated to be $93 - 96\%$.

These observations suggest that ion-ion collisions can play a significant role in modifying the distribution function of ions over time, and highlight the importance of understanding collisional processes in foam plasmas.

We estimate the homogenization time for electrons to be approximately $t_h \simeq 14$ ps and for ions to be approximately $t_h \simeq 15$ ps. This estimate can be obtained from Figure 4.14, which shows the time dependence of electron and ion energies averaged over the cylinder (red) and outside the cylinder (blue) in the ablated plasma under S-polarization. The time evolution of electron and ion energies is similar to the one shown in Figure 4.6, where ion-ion collisions are absent. The average energy of the ablated plasma at $t = 15$ ps is approximately $\sim 0.8$ keV for electrons and $\sim 5$ keV for ions, but there is a significant difference in the core energies. At a time of $t \simeq 14$ ps, the electron core energy is as high as the ablated plasma energy. This fact is due to more efficient collisional heat transport.

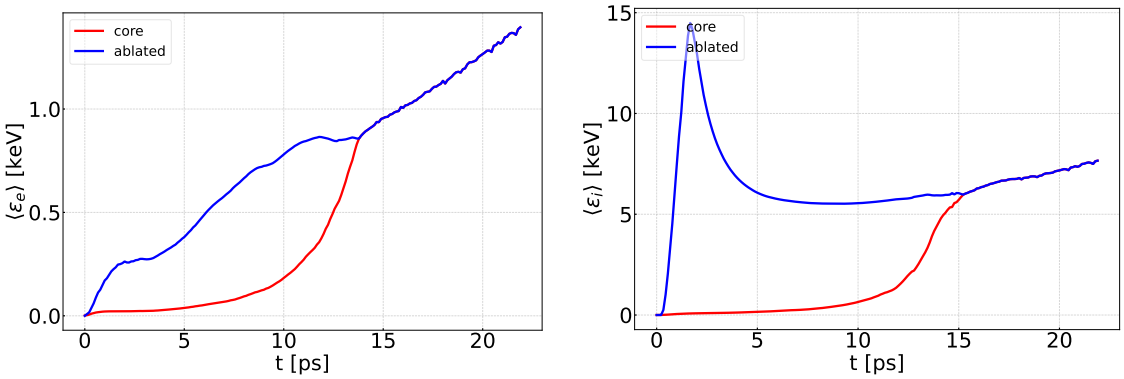


Figure 4.14: Time dependence of electron (a) and ion (b) energy averaged over the volume inside cylinder (red) and outside cylinder (blue) for the case of S-polarization.

The difference in homogenization times for electrons and ions is due to the longer elec-

tron mean free path, which slows the homogenization of the electron energy distribution function, compared to ions. In contrast, the shorter ion mean free path results in more frequent ion-ion collisions, leading to faster homogenization of the ion energy distribution function. We estimate the ion-ion collisional rate as $\nu_{ii'} = 0.05$ ps$^{-1}$. This corresponds to a relaxation time $\tau_{ii'} = 20$ ps, which is in good agreement with Figure 4.13.

PIC simulations show that ion-ion collisions play an important role in the homogenization process in low-density porous plasmas, leading to a significant reduction in homogenization time. This reduction is due to energy and momentum transfer between ions during collisions, resulting in a more homogeneous ion population.

## 4.7 Implementation of the reduced laser-foam interaction model in a hydrodynamic code

The two-scale model aims to capture the dynamics of a foam on both spatial and temporal scales. At the macro-scale, the foam is treated as a homogeneous medium with average properties, without resolving the internal dynamics of individual pores. This scale is computed using standard plasma hydrodynamics methods, represented by partial differential equations, and provides a connection between fully homogenized pores. The micro-scale, on the other hand, models the laser interaction with individual solid elements, providing information about the subdivision of mass and energy inside the pore. The micro-scale computation is isolated to individual elements and relies on the macro-scale to estimate the state of adjacent pores. This is crucial for accurately estimating the incident laser intensity and energy transferred by heat conductivity. The micro-scale model is formulated using ordinary differential equations, allowing for efficient and high temporal resolution computation without affecting the performance of the hydrodynamic code used for the macro-scale computation.

### 4.7.1 Macro-scale hydrodynamic model

The macro-scale hydrodynamic model for plasma density $\varrho$, flow velocity $\mathbf{U}$, and internal energies of ions and electrons, $\varepsilon_i$ and $\varepsilon_e$, is described by the two-temperature Euler equations in Lagrangian coordinates:

$$\frac{1}{\varrho}\frac{d\varrho}{dt} = -\nabla \mathbf{U}, \tag{4.7}$$

$$\varrho\frac{d\mathbf{U}}{dt} = -\nabla(p_e + p_i), \tag{4.8}$$

$$\varrho\frac{\mathrm{d}\varepsilon_i}{\mathrm{d}t} = -p_i\nabla\mathbf{U} + G_{ei}(T_e - T_i) + \nabla(\kappa_i\,\nabla T_i), \tag{4.9}$$

$$\varrho\frac{\mathrm{d}\varepsilon_e}{\mathrm{d}t} = -p_e\nabla\mathbf{U} + G_{ie}(T_i - T_e) + \nabla(\kappa_e\,\nabla T_e) - \nabla\mathbf{I}_{\mathrm{las}}. \tag{4.10}$$

These equations include terms specific to plasma, such as ion and electron heat conductivity, laser energy deposition, and electron-ion temperature relaxation. The first terms on the right-hand side of Eqs. (4.7) - (4.10) describe pure hydrodynamics, while the second terms on Eqs. (4.9) and (4.10) represent electron-ion temperature relaxation. The third and fourth terms on Eq. (4.10) describe heat conductivity and laser source, respectively. The electron/ion pressures $p_{e,i}$ and temperatures $T_{e,i}$ are related to primary conservative variables using the ideal gas equation of state.

The hydrodynamic equations (4.7) - (4.10) are implemented in a two-dimensional cylindrical $r, z$ geometry in the code PALE (Prague Arbitrary Lagrangian Eulerian code)[119] in Lagrangian form and in the code FLASH [120] in Eulerian form.

The computational cells used in the model can exist in one of three states: cold, intermediate, or fully homogenized plasma. These states are determined by the homogenization of the solid foam elements within the cells, which are modeled at the micro-scale level. Initially, all cells are in the cold state, where the solid elements are at room temperature and are surrounded by vacuum or a low-density gas. When a laser or heat wave reaches a cold cell, it transits to the intermediate state, as determined by the micro-scale model. In these cells, both micro-scale and macro-scale models run in parallel, with certain aspects of the foam internal dynamics (such as laser deposition and electron-ion energy redistribution) handled by the micro-model to avoid duplicating calculations. During the homogenization process, we assume that the macro-scale cells remain stationary with constant mass and zero flow velocity. Thus, when the micro-scale model is active, only the equations for laser and heat transport need to be solved in the macro-scale cell. Homogenization terminates when the foam element density drops below the average foam density or when it equals the density of the surrounding plasma, causing the corresponding macro-scale cell to transition to the plasma state, for which we solve the complete hydrodynamic system (4.7) – (4.10).

To model laser energy transport and absorption, we use the ray tracing method. The laser beam is split into independent rays, and their trajectories are governed by the ray equation of geometric optics. The power of each ray is attenuated along its path, with

the absorption rate depending on the cell state. For cells in the plasma state, we use the standard inverse Bremsstrahlung absorption coefficient, while for cells in the intermediate state, we employ a microscopic absorption coefficient that combines absorption in the solid foam element and ambient plasma.

### 4.7.2 Micro-scale hybrid ablation-expansion model

Each macro-scale computation cell corresponds to a micro-scale cell that has the shape of a parallelepiped, as shown in Figure 3.1. To ensure that each macroscopic cell has exactly one solid element and thus corresponds to one foam pore, the initial dimensions of the macro-scale cell in the radial and axial directions are set to be equal to the pore size $l_p$, i.e., $\Delta r = \Delta z = l_p$. The micro-cell has the same mass and volume $V_{\text{pore}} = l_p^2 l_c$ as its parent macro-scale cell. In the 2D axially symmetric geometry, the volume of the macro-cell (obtained by rotating the cell $\Delta r \times \Delta z$ around the $z$ axis by 1 radian) depends on its distance from the $z$ axis, and thus the length $l_c$ is equal to the radius of the center of the macro-scale cell (foam elements are longer further away from the symmetry axis).

In the center of each pore lies a solid foam element, which is modeled as a cylinder with length $l_c$ and radius $a$. The rest of the pore is filled with low-density background plasma, which we refer to as the ambient plasma. Initially, the cylinder contains a solid material with density $\varrho_s$, and its radius is determined by the average foam density $\bar{\varrho}$ as $a_0 = l_p\sqrt{\bar{\varrho}/(\pi\varrho_s)}$. The total mass of the micro-scale cell $m_0$ is divided into the mass of the cylinder $m_{\text{cyl}}$ and the mass of the plasma $m_{\text{pl}}$, which sum up to the cell mass $M_{\text{cell}} = V_{\text{pore}}\bar{\varrho}$, where $V_{\text{pore}} = l_p^2 l_c$. The initial mass of the cylinder is 0.97 $m_0$, with the remaining 0.03 $m_0$ placed in the ambient plasma to avoid nonphysical divergences. The micro-scale cell volume $V_{\text{pore}}$ is divided into the cylinder volume $V_{\text{cyl}} = \pi a^2 l_c$ and the plasma volume $V_{\text{pl}} = V_{\text{pore}} - V_{\text{cyl}} = l_p^2 l_c - \pi a^2 l_c$. The cylinder radius $a(t)$, mass $m_{\text{cyl}}(t)$, density $\varrho_{\text{cyl}}(t) = m_{\text{cyl}}/(\pi a^2 l_c)$, and temperature $T_{\text{cyl}}(t)$ are constant in space. The fluid velocity $v_{\text{cyl}}$ inside the cylinder is a linear function of radius and approaches the expansion velocity at the cylinder edge $r = a$.

The parameters of the cylinder evolve over time according to a set of ordinary differential equations. Mass and energy exchange between the cylinder and the ambient plasma are modeled at the micro-scale. The ambient plasma is characterized by its density $\varrho_{\text{pl}}$, electron temperature $T_{\text{pe}}$, ion temperature $T_{\text{pi}}$, and zero flow velocity. Although assuming zero velocity of the ambient plasma is a simplification, we assume that any relaxation process due to ion-ion collisions or turbulence is faster than the foam homogenization time. This hypothesis may not hold for foams with large pores or when ablated plasma collides with flows from neighboring cells.

As ablation proceeds, the ambient plasma mass increases, leading to an increase in

plasma density given by $\varrho_{\rm pl}(t) = (m_0 - m_{\rm cyl})/V_{\rm pl}$. The motion of the cylinder boundary is controlled by radial expansion and mass ablation. Surface energy deposition from laser absorption and thermal heat flux from the ambient plasma drive the ablation process, accelerating the ablated mass and converting absorbed energy into kinetic energy of accelerated particles such as electrons and ions. Due to collisions with the background plasma, the kinetic energy of the ablated vapors is eventually converted into a plasma thermal energy, resulting in a continuous conversion of ablated mass and energy flux into a homogeneous ambient plasma with increasing mass and internal energy of ions and electrons. This assumption of continuous energy and mass exchange between two phases is physically justifiable since the ambient plasma is hot and the ablation flow is subsonic.

The micro-model operation regime is determined by a set of free parameters. Some of these parameters are obtained from the results of PIC simulations described in Section 4. The appropriate value of the absorption factor $Q_{\rm abs}$, averaged over S and P-polarizations, is in the range of $0.5-1.5$ according to the Mie theory. However, kinetic simulations have narrowed down the value to $Q_{\rm abs} = 0.75$, which is the value we have used. The ion-electron energy partition in the ablated plasma is characterized by a dimensionless parameter $\zeta_i$, which is set to 0.6 based on the kinetic simulations of a single pore of the foam. Finally, the value of the ablation velocity is characterized by a dimensionless parameter, which is set to $\xi_a = 0.5$, by comparing the ablation velocity measured in Section 4.4 with the theory of planar ablation [141].

This hybrid ablation-expansion micro-macro model has been implemented in the code PALE and in the code FLASH, which is described in details in Ref. [122].

## 4.8 Conclusion for Chapter 4

By using the Mie theory and numerical simulations, we investigated the interaction between intense laser radiation and an elementary cell in a foam. The foam solid element is represented by a cylinder with a sub-wavelength radius. The laser absorption efficiency in solid element strongly depends on its structure, shape and orientation with respect to the laser polarization. The theory indicates that S-polarization leads to enhanced laser absorption due to plasma resonance. As a result of bulk heating and surface ablation, solid element turns into plasma. Remarkably, the ablation rate is qualitatively consistent with the theory of stationary laser ablation.

For P-polarization, absorption occurs due to electron collisions, and the conversion of solid element to plasma occurs due to its heating and expansion. For both polarizations, absorption occurs at the surface of solid elements, and energy transport inside the element is suppressed due to the high level of collisionnality, resulting in a much lower plasma

temperature in the core compared to the ablated plasma. The latter is characterized by a large difference between kinetic energies of electrons and ions. In the simulation, approximately 60% of absorbed laser energy is transferred to ions, resulting in an ion temperature ratio of $T_i/ZT_e \simeq 1.5$ after ion thermalization. This ion overheating makes the plasma generated from foam different from that produced from homogeneous materials where electron heating is the dominant process and electron temperature is higher than the ion temperature.

Following the Mie theory, laser scattering and absorption is described using dimensionless efficiency factors. However, unlike a homogeneous cylinder, the absorption efficiency factor is notably higher for S-polarization and does not depend on electron collisionality. Additionally, both absorption and scattering efficiency factors increase over time due to cylinder expansion.

The evolution of the cylinder density over time can be described by a bell-shaped function with three parameters that vary with time: central density, radius, and steepness. This is expressed in Eq. (3.41). The evolution of cylinder occurs in two distinct phases. In the first phase, the cylinder radius decreases as the rarefaction wave converges towards the center. The second phase corresponds to the expansion of the cylinder.

These results can be compared to microscopic models proposed by Gus'kov et al. [41], [131] and Belyaev et al. [36], [133]. None of these two models provides a description of the laser absorption mechanism, instead proposing the use of a constant *ad hoc* absorption efficiency factor for opaque solid elements. Gus'kov et al. suggest using an absorption factor of $1/2\pi \simeq 0.16$ for cylindrical solid elements, while Belyaev et al. [36], as discussed in Section 3.3.1, approximate the cylinder density profile with a Gaussian function (3.41) with $p = 2$ and assume that all optical rays incident on the cylinder with an impact factor smaller than the critical density radius $r_{\mathrm{cr}}$ are absorbed. This corresponds to an absorption efficiency factor equal to the ratio of $r_{\mathrm{cr}}$ to the cylinder radius, $r_{\mathrm{cr}}/a = (\ln(\varrho_s/\varrho_{\mathrm{cr}})/\ln 2)^{1/2}$, which falls within the range of $1.9 - 2.3$ for the parameters used in our simulations.

Upon comparing the values of $Q_{\mathrm{abs}}$ with the absorption factors depicted in Figures 3.5(b) and 4.12(b), it is evident that the model proposed by Belyaev et al. [36], [133] overestimates the absorption, while the model by Gus'kov et al. [41], [131] significantly underestimates it. Additionally, both models assume a homogeneous temperature distribution within the pore, resulting in a shorter homogenization time in the model by Gus'kov et al. and a higher expansion velocity in the model by Belyaev et al. In contrast, our model, which accounts for resonance laser absorption and the temperature difference between the solid element and ambient plasma, is more realistic and versatile in various applications.

We conducted numerical simulations of laser irradiation on an underdense foam with

open pores, using a laser intensity of $10^{14}$ W/cm$^2$. The electron and ion temperatures obtained from the simulations are consistent with experimental data [38], [145]. Due to the relatively small size of the solid element compared to the pore size, the laser absorption in a single pore is small. Therefore, we infer that laser heating and foam homogenization involve many pores, resulting in a homogenization layer thickness that is $l_p/a$ times larger than the pore size. Our findings are relevant for the development of a multi-scale model for foam heating by laser radiation, which is presented in Ref. [122], along with a comparison to experimental data. Our analysis can also be extended to foams with different shapes of solid elements and to over-dense foams, where the process of solid element heating and expansion is controlled by the electron heat flux.

# Chapter 5

# Conclusion

This work is dedicated to the theoretical and numerical studies of nonlinear, high intensity laser interaction with plasmas in the context of shock ignition approach to inertial confinement fusion for energy production. Two subjects of prime importance are considered: i) the control of nonlinear laser absorption in plasma mitigation of laser backscattering due to the competition between stimulated Brillouin and Raman scattering; ii) the interaction of laser radiation with low density porous materials and their transformation in a hot homogeneous plasma.

The studies of nonlinear laser plasma interaction are presented in Chapters 1 and 2. They demonstrate the necessity of mitigating SBS to achieve efficient laser absorption under shock ignition conditions. Several methods of SBS suppression have been tested and evaluated, including the use of multiple ion species, plasma expansion, and laser bandwidth. By adding hydrogen to the ablator, one can dramatically increase the damping of ion acoustic waves, thereby suppressing the convective SBS gain and the SBS reflectivity. Similar effects can be achieved by using laser pulses with bandwidth larger than a few THz or with steep profiles of plasma flow velocity.

The suppression of SBS opens the way for more efficient laser energy absorption due to the excitation of SRS. Under the parameters relevant to the shock ignition scheme, SRS is excited as an absolute instability near the quarter critical density. This enhances laser absorption through the trapping and absorption of the daughter scattered wave in the density cavities and electron acceleration by the daughter plasma waves. The theoretical analysis of trapped modes in plasma cavities in Section 1.5 is confirmed in the numerical simulations, showing efficient absorption of laser energy exceeding 30% and ion acceleration in the expanding cavities, as described in Section 2.6. Trapping of electrons in plasma waves and wave breaking results in transferring up to 10% of laser energy to hot electrons with an effective temperature of 35 keV. According to shock ignition target designs [18], such hot electrons may improve the shock ignition performance and do not

present a danger for fuel preheat.

The studies of SBS and SRS competition are performed in a 1D geometry, with the plasma profiles obtained from hydrodynamic simulations relevant to shock ignition conditions. The results of the 1D simulations are compared with several 2D simulations having similar plasma density and temperature profiles. The 2D simulation results confirm the dominance of SBS/SRS competition and electron acceleration near the quarter critical density. This comparison shows the relevance of our results to realistic experimental conditions, providing important insights for future studies of shock ignition. Overall, our work advances the understanding of the physics underlying these instabilities, providing a foundation for further exploration and optimization of ICF systems.

The theoretical and numerical analysis of laser interaction with porous materials in Chapters 3 and 4 sheds new light on the physics of high intensity laser interaction with structured low density materials and provides valuable input for constructing a sub-grid model describing foam heating and homogenization. We address the following three aspects: First, we demonstrate that the absorption cross section strongly depends on the density profile of the solid element and the laser polarization. We have shown that assuming the absorption cross section is equal to the geometrical cross section leads to a severe overestimation of the absorption rate. Applying Mie theory to the expanding subwavelength cylinder, we determine the scattering and absorption cross section. Cylinders with radially inhomogeneous density show a larger absorption due to the contribution of collisionless resonance absorption. Second, we investigate the process of transformation of a solid structural element into hot plasma due to laser absorption and heat flux from the ambient plasma. We compare two processes: bulk heating and expansion and surface absorption and ablation. It is shown that the latter process dominates due to the suppression of heat flux inside the cylinder for the cylinder radius of $0.1\,\mu$m or larger. The ablation rate is found to be in agreement with the theory of laser ablation of bulk materials. Third, we evaluate the energy partition between electrons and ions in the ablated plasma. In contrast to homogeneous materials, laser ablation of structural elements in underdense foams results in strong ion overheating with 60% of the absorbed energy transferred to ions. This efficient ion heating is explained by ion acceleration in the sheath electric field near the absorption zone and ion-ion collisional relaxation in the ambient plasma. Our findings provide important insights for designing and optimizing laser-plasma interaction experiments and simulations involving underdense structural materials.

The results obtained in this work open further perspectives in the laser plasma interaction studies in application to the shock ignition and to the laser-driven inertial fusion in general. To achieve efficient laser absorption under shock ignition conditions, the mitigation of SBS is of utmost importance. The methods of SBS suppression, including the use

of multiple ion species, plasma expansion, and laser bandwidth, have been shown to be effective in our 1D simulations. However, these methods should be considered together, rather than separately, in full 2D simulations, where the effects of sidescattered SRS, TPD, or enhanced cavitation can be fully examined. The investigation of SBS mitigation methods in 2D geometry is essential for developing a comprehensive understanding of the laser-plasma interaction dynamics.

Further investigation of foam targets is necessary to fully understand the nonlinear interaction between high intensity lasers and structured materials. One important aspect that needs to be considered is the pore size of the foam, as it can significantly affect the absorption and scattering cross sections. Additionally, the overall nonlinearity of absorption in such circumstances, including collisionless resonance absorption, needs to be explored in more detail, in particular for structured elements of different forms and sizes. Moreover, the process of homogenization of the foam due to laser heating and ion-ion collisions is a crucial factor that should be further investigated in simulations.

# Personal publications and conference presentations

**Conferences and workshops:**

1. **November 2022**, Joint ELI User Meeting 2022 (foam target workshop), Prague, Czech Republic
   Oral talk: "Kinetic modelling of laser absorption in foams"

2. **September 2022**, European Conference on Laser Interaction with Matter (ECLIM), Frascati, Italy
   Oral talk: "Kinetic modelling of laser absorption in foams"

3. **May 2022**, Direct Drive and Fast Ignition Workshop (DDFIW), Madrid, Spain
   Oral talk: "Kinetic modelling of laser absorption in foams"

4. **April 2019**, IOP Plasma Physics Conference, Loughborough, UK
   Oral talk: "Collective absorption of laser radiation in plasma at sub-relativistic intensities."

5. **October 2015**, Moscow, The International School on Ultra-Intense Lasers
   I have experience as an organizer for this school.

6. **January 2015**, Scientific Session MEPHI, Moscow
   Oral talk: "Modelling of smoothing intensity laser pulses by a random phase plate"

7. **January 2014**, Scientific Session MEPHI, Moscow
   Oral talk: "Search for the optimal configuration of the dynamic phase plate"

**List of personal publications**

S. Shekhanov, A. Gintrand, L. Hudec, R. Liska, J. Limpouch, S. Weber, and V. Tikhonchuk, "Kinetic modeling of laser absorption in foams", Phys. Plasmas 30, 012708 (2023), DOI: 10.1063/5.0131786. This article has been chosen to be promoted as an Editor's Pick. (Ref. [37])

L. Hudec, A. Gintrand, J. Limpouch, R. Liska, S. Shekhanov, V.T. Tikhonchuk and S. Weber (2023). Model for foam ionization and heating. Accepted for publication in Phys. Plasmas. (Ref. [122])

S. A. Shekhanov and V. T. Tikhonchuk, SRS-SBS competition and nonlinear laser energy absorption in a high temperature plasma. Plasma Phys. Control. Fusion 63, 115016

(2021), DOI: 10.1088/1361-6587/ac2614 (Ref. [67])

Y. Gu, O. Klimo, Ph. Nicolaï, S. Shekhanov, S. Weber, and V. Tikhonchuk, Collective absorption of laser radiation in plasma at sub-relativistic intensities. High Power Laser Sci. Eng. 7, E39 (2019), DOI: 10.1017/hpl.2019.25 (Ref. [65])

# Bibliography


[1] J. D. Lawson, "Lasers and accelerators", *IEEE Trans. Nucl. Sci.*, vol. NS-26, p. 4217, 1979.

[2] S. Atzeni and J. Meyer-ter Vehn, *The Physics of Inertial Fusion*. Clarendon Press, 2004. DOI: 10.1093/acprof:oso.

[3] W. Seka, D. H. Edgell, J. F. Myatt, *et al.*, "Two-plasmon-decay instability in direct-drive inertial confinement fusion experiments", *Phys. Plasmas*, vol. 16, no. 5, p. 052 701, 2009. DOI: 10.1063/1.3125242.

[4] D. Turnbull, A. V. Maximov, D. H. Edgell, *et al.*, "Anomalous absorption by the two-plasmon decay instability", *Phys. Rev. Lett.*, vol. 124, p. 185 001, 2020. DOI: 10.1103/PhysRevLett.124.185001.

[5] R. K. Follett, J. G. Shaw, J. F. Myatt, H. Wen, D. H. Froula, and J. P. Palastro, "Thresholds of absolute two-plasmon-decay and stimulated Raman scattering instabilities driven by multiple broadband lasers", *Phys. Plasmas*, vol. 28, p. 032 103, 2021. DOI: 10.1063/5.0037869.

[6] E. M. Epperlein, "Kinetic theory of laser filamentation in plasmas", *Phys. Rev. Lett.*, vol. 65, pp. 2145–2148, 1990. DOI: 10.1103/PhysRevLett.65.2145.

[7] Epperlein,E. M., "Kinetic simulations of laser filamentation in plasmas", *Phys. Fluids B*, vol. 3, pp. 3082–3086, 1991. DOI: 10.1063/1.859788.

[8] P. E. Young, "Experimental study of filamentation in laser–plasma interactions", *Phys. Fluids B*, vol. 3, no. 8, pp. 2331–2336, 1991. DOI: 10.1063/1.859600.

[9] P. Michel, L. Divol, E. A. Williams, *et al.*, "Tuning the implosion symmetry of icf targets via controlled crossed-beam energy transfer", *Phys. Rev. Lett.*, vol. 102, p. 025 004, 2 Jan. 2009. DOI: 10.1103/PhysRevLett.102.025004.

[10] E. A. Williams, B. I. Cohen, L. Divol, *et al.*, "Effects of ion trapping on crossed-laser-beam stimulated Brillouin scattering", *Phys. Plasmas*, vol. 11, p. 231, 2004. DOI: 10.1063/1.1630573.

[11] E. Campbell, V. Goncharov, T. Sangster, *et al.*, "Laser-direct-drive program: Promise, challenge, and path forward", *Matter Radiation Extremes*, vol. 2, pp. 37–54, 2017. DOI: 10.1016/j.mre.2017.03.001.

[12] W. Kruer, *The Physics of Laser Plasma Interactions*. Redwood, CA: Addison-Wesley - CRC Press, 1988, ISBN: 978-0367314187.

[13] H. A. Bethe, "Energy production in stars", *Phys. Rev.*, vol. 55, pp. 434–456, 1939.

[14] F. Hoyle, "The synthesis of the elements from hydrogen", *Monthly Notices of the Royal Astronomical Society*, vol. 106, pp. 343–383, 1946.

[15] *Ivy mike — Wikipedia, the free encyclopedia*, [Online; accessed 29-September-2012], 2022. [Online]. Available: https://en.wikipedia.org/wiki/Ivy_Mike.

[16] J. Nuckolls, L. L. Wood, and A. F. Barker, "Laser compression of matter to super-high densities", *Nature*, vol. 239, no. 5371, pp. 139–142, 1972.

[17] R. S. Craxton, K. S. Anderson, T. R. Boehly, *et al.*, "Direct-drive inertial confinement fusion: A review", *Phys. Plasmas*, vol. 22, p. 110 501, 2015. DOI: 10.1063/1.4934714.

[18] D. Batani, S. Baton, A. Casner, *et al.*, "Physics issues for shock ignition", *Nucl. Fusion*, vol. 54, p. 054 009, 2014. DOI: 10.1088/0029-5515/54/5/054009.

[19] B Canaud and M Temporal, "High-gain shock ignition of direct-drive icf targets for the laser mégajoule", *New J. Phys.*, vol. 12, p. 043 037, 2010. DOI: 10.1088/1367-2630/12/4/043037.

[20] J.-L. Miquel and E. Prene, "LMJ & PETAL status and program overview", *Nuclear Fusion*, vol. 59, p. 032 005, Mar. 2019. DOI: 10.1088/1741-4326/aac343.

[21] G. Pérez-Callejo, C. Vlachos, C. Walsh, *et al.*, "Cylindrical implosion platform for the study of highly magnetized plasmas at Laser MegaJoule", *Phys. Rev. E*, vol. 106, p. 035 206, Sep. 2022. DOI: 10.1103/PhysRevE.106.035206.

[22] J. D. Lindl, P. Amendt, R. L. Berger, *et al.*, "The physics basis for ignition using indirect-drive targets on the National Ignition Facility", *Phys. Plasmas*, vol. 11, no. 2, pp. 339–491, 2004. DOI: 10.1063/1.1578638.

[23] L. Perkins, R. Betti, K. LaFortune, and W. Williams, "Shock Ignition: A New Approach to High Gain Inertial Confinement Fusion on the National Ignition Facility", *Phys. Rev. Lett.*, vol. 103, p. 045 004, 2009. DOI: 10.1103/PHYSREVLETT.103.045004.

[24] A. B. Zylstra, A. L. Kritcher, O. A. Hurricane, *et al.*, "Experimental achievement and signatures of ignition at the national ignition facility", *Phys. Rev. E*, vol. 106, p. 025 202, 2 Aug. 2022. DOI: 10.1103/PhysRevE.106.025202.

[25] R. Betti, C. D. Zhou, K. S. Anderson, L. J. Perkins, W. Theobald, and A. A. Solodov, "Shock ignition of thermonuclear fuel with high areal density", *Phys. Rev. Lett.*, vol. 98, p. 155 001, 2007. DOI: 10.1103/PhysRevLett.98.155001.

[26] X Ribeyre, G Schurtz, M Lafon, S Galera, and S Weber, "Shock ignition: An alternative scheme for hiper", *Plasma Phys. Control. Fusion*, vol. 51, no. 1, p. 015 013, 2008. DOI: 10.1088/0741-3335/51/1/015013.

[27] W. Theobald, K. S. Anderson, R. Betti, *et al.*, "Advanced-ignition-concept exploration on OMEGA", *Plasma Phys. Control. Fusion*, vol. 51, p. 124 052, 2009. DOI: 10.1088/0741-3335/51/12/124052.

[28] C. Labaune, S. Depierreux, D. Michel, *et al.*, "Smoothing of laser beam intensity fluctuations in low density foam plasmas with the LIL laser", *35th EPS Conference on Plasma Physics 2008, EPS 2008 - Europhysics Conference Abstracts*, vol. 32, Jan. 2008.

[29] S. Depierreux, C. Labaune, D. Michel, *et al.*, "Laser smoothing and imprint reduction with a foam layer in the multikilojoule regime", *Phys. Rev. Lett.*, vol. 102, p. 195 005, 2009. DOI: 10.1103/PHYSREVLETT.102.195005.

[30] S. Hu, W. Theobald, P. B. Radha, *et al.*, "Mitigating laser-imprint effects in direct-drive inertial confinement fusion implosions with an above-critical-density foam layer", *Phys. Plasmas*, vol. 25, p. 082 710, 2018. DOI: 10.1063/1.5044609.

[31] B. Delorme, M. Olazabal-Loumé, A. Casner, *et al.*, "Experimental demonstration of laser imprint reduction using underdense foams", *Phys. Plasmas*, vol. 23, p. 042 701, 2016. DOI: 10.1063/1.4945619.

[32] V. T. Tikhonchuk, T. Gong, N. Jourdain, *et al.*, "Studies of laser-plasma interaction physics with low-density targets for direct-drive inertial confinement fusion on the shenguang iii prototype", *Matter and Radiation at Extremes*, vol. 6, no. 2, p. 025 902, 2021. DOI: 10.1063/5.0023006.

[33] Y. Wu, X. Wang, T. Ray, and A. Hassanein, "Experimental study of dynamics and soft x-ray emission of laser produced plasma from low-density foam Ti targets", *Vacuum*, vol. 207, p. 111 604, Oct. 2022. DOI: 10.1016/j.vacuum.2022.111604.

[34] S. S. Bulanov, V. Y. Bychenkov, V. Chvykov, *et al.*, "Generation of GeV protons from 1 PW laser interaction with near critical density targets", *Phys. Plasmas*, vol. 17, p. 043 105, 2010. DOI: 10.1063/1.3372840.

[35] E. Yazdani, R. Sadighi-Bonabi, H. Afarideh, J. Yazdanpanah, and H. Hora, "Enhanced laser ion acceleration with a multi-layer foam target assembly", *Laser Part. Beams*, vol. 32, pp. 509–515, 2014. DOI: 10.1017/S0263034614000342.

[36] M. A. Belyaev, R. L. Berger, O. S. Jones, S. H. Langer, and D. A. Mariscal, "Laser propagation in a subcritical foam: Ion and electron heating", *Phys. Plasmas*, vol. 25, p. 3059, 2018. DOI: 10.1063/1.5050531.

[37] S. Shekhanov, A. Gintrand, L. Hudec, *et al.*, "Kinetic modelling of laser absorption in foams", *Phys. Plasmas*, vol. 30, p. 012 708, 2023. DOI: 10.1063/5.0131786.

[38] P. Nicolaï, M. Olazabal-Loumé, S. Fujioka, *et al.*, "Experimental evidence of foam homogenization", *Phys. Plasmas*, vol. 19, no. 11, p. 113 105, 2012. DOI: 10.1063/1.4766470.

[39] S. Y. Gus'kov, J. Limpouch, P. Nicolaï, and V. T. Tikhonchuk, "Laser-supported ionization wave in under-dense gases and foams", *Phys. Plasmas*, vol. 18, p. 103 114, 2011.

[40] M. Cipriani, S. Y. Gus'kov, R. De Angelis, *et al.*, "Laser-driven hydrothermal wave speed in low-Z foam of overcritical density", *Phys. Plasmas*, vol. 25, p. 092 704, 2018. DOI: 10.1063/1.5041511.

[41] M. Cipriani, S. Y. Gus'kov, R. De Angelis, *et al.*, "Laser-supported hydrothermal wave in low-dense porous substance", *Laser Part. Beams*, vol. 36, p. 121, 2018. DOI: 10.1017/S0263034618000022.

[42] J. Thomson, W. Kruer, S. Bodner, and J. DeGroot, "Parametric instability thresholds and their control", *Phys. Fluids*, vol. 17, p. 849, Apr. 1974. DOI: 10.1063/1.1694799.

[43] D. Pesme, R. L. Berger, E. A. Williams, A. Bourdier, and A. Bortuzzo-Lesne, "A statistical description of parametric instabilities with an incoherent pump", *arXiv:0710:2195*, 2007.

[44] Y. Zhao, L.-L. Yu, J. Zheng, *et al.*, "Effects of large laser bandwidth on stimulated raman scattering instability in underdense plasma", *Phys. Plasmas*, vol. 22, p. 052 119, 2015. DOI: 10.1063/1.4921659.

[45] Y. Zhao, S. Weng, M. Chen, *et al.*, "Effective suppression of parametric instabilities with decoupled broadband lasers in plasma", *Phys. Plasmas*, vol. 24, no. 11, p. 112 102, 2017. DOI: 10.1063/1.5003420.

[46] R. K. Follett, J. G. Shaw, J. F. Myatt, C. Dorrer, D. H. Froula, and J. P. Palastro, "Thresholds of absolute instabilities driven by a broadband laser", *Phys. Plasmas*, vol. 26, p. 062 111, 2019. DOI: 10.1063/1.5098479.

[47] H. Y. Zhou, C. Z. Xiao, D. B. Zou, *et al.*, "Numerical study of bandwidth effect on stimulated Raman backscattering in nonlinear regime", *Phys. Plasmas*, vol. 25, no. 6, p. 062 703, 2018. DOI: 10.1063/1.5030153.

[48] C. Benedetti, C. B. Schroeder, E. Esarey, and W. P. Leemans, "Plasma wakefields driven by an incoherent combination of laser pulses: A path towards high-average power laser-plasma accelerators", *Phys. Plasmas*, vol. 21, p. 056 706, 2014. DOI: 10.1063/1.4878620.

[49] L. Brillouin, "Diffusion de la lumière et des rayons x par un corps transparent homogène: Influence de l'agitation thermique", *Ann. Phys. (France)*, vol. 17, p. 88, 1922.

[50] N. M. Kroll, "Excitation of hypersonic vibrations by means of photoelastic coupling of high-intensity light waves to elastic waves", *J. Appl. Phys.*, vol. 36, pp. 34–43, 1965. DOI: 10.1063/1.1713918.

[51] C. S. Liu, M. N. Rosenbluth, and R. B. White, "Raman and Brillouin scattering of electromagnetic waves in inhomogeneous plasmas", *Phys. Fluids*, vol. 17, p. 1211, 1974.

[52] D. W. Forslund, J. M. Kindel, and E. L. Lindman, "Theory of stimulated scattering processes in laser-irradiated plasmas", *Phys. Fluids*, vol. 18, pp. 1002–1016, 1975. DOI: 10.1063/1.861248.

[53] D. W. Forslund and J. M. Kindel and E. L. Lindman, "Nonlinear behavior of stimulated Brillouin and Raman scattering in laser-irradiated plasmas", *Phys. Rev. Lett.*, vol. 30, pp. 739–743, 1973. DOI: 10.1103/PhysRevLett.30.739.

[54] D. W. Forslund and J. M. Kindel and E. L. Lindman, "Plasma simulation studies of stimulated scattering processes in laser-irradiated plasmas", *Phys. Fluids*, vol. 18, pp. 1017–1030, 1975. DOI: 10.1063/1.861249.

[55] W. Kruer, K. Estabook, and K. Sinz, "Instability-generated laser reflection in plasmas", *Nucl. Fusion*, vol. 13, p. 952, 1973. DOI: 10.1088/0029-5515/13/6/024.

[56] A. A. Galeev, G. Laval, T. M. O'Neil, M. N. Rosenbluth, and R. Z. Sagdeev, "Parametric back scattering of a linear electromagnetic wave in a plasma", *JETP Lett.*, vol. 17, p. 35, 1973.

[57] C. Neuville, V. Tassin, D. Pesme, *et al.*, "Experimental evidence of the collective Brillouin scattering of multiple laser beams sharing acoustic waves", *Phys. Rev. Lett.*, vol. 116, p. 235 002, 2016. DOI: 10.1103/PhysRevLett.116.235002.

[58] J. Thomson, "Finite-bandwidth effects on the parametric instability in an inhomogeneous plasma", *Phys. Fluids*, vol. 15, p. 237, 1975.

[59] G. Laval, R. Pellat, D. Pesme, A. Ramani, M. N. Rosenbluth, and E. A. Williams, "Parametric instabilities in the presence of space-time random fluctuations", *Phys. Fluids*, vol. 20, p. 2049, 1977.

[60] V. Bychenkov, W. Rozmus, and V. Tikhonchuk, "Ion acoustic waves in plasmas with light and heavy ions", *Phys. Rev. E*, vol. 51, p. 1400, 1995. DOI: 10.1103/PhysRevE.51.1400.

[61] E. A. Williams, R. L. Berger, R. P. Drake, *et al.*, "The frequency and damping of ion acoustic waves in hydrocarbon (CH) and two-ion-species plasmas", *Phys. Plasmas*, vol. 2, p. 129, 1995. DOI: 10.1063/1.871101.

[62] Q. S. Feng, C. Y. Zheng, Z. J. Liu, *et al.*, "Stimulated Brillouin scattering behaviors in multi-ion species plasmas in high-temperature and high-density region", *Phys. Plasmas*, vol. 26, p. 052 101, 2019. DOI: 10.1063/1.5088372.

[63] B. Fried and S. D. Conte, *The Plasma Dispersion Function: The Hilbert transform of the Gaussian focuses on the reactions, transformations, and calculations involved in plasma dispersion function*. New York: Academic Press, Elsevier Inc., 1961. DOI: 10.1016/C2013-0-12176-9.

[64] W. Theobald, A. Bose, R. Yan, *et al.*, "Enhanced hot-electron production and strong-shock generation in hydrogen-rich ablators for shock ignition", *Phys. Plasmas*, vol. 24, p. 120 702, 2017. DOI: 10.1063/1.4986797.

[65] Y. J. Gu, O. Klimo, P. Nicolaï, S. Shekhanov, S. Weber, and V. T. Tikhonchuk, "Collective absorption of laser radiation in plasma at sub-relativistic intensities", *High Power Laser Sci. Eng.*, vol. 7, e39, 2019. DOI: 10.1017/hpl.2019.25.

[66] A. G. Seaton and T. D. Arber, "Laser-plasma instabilities in long scale-length plasmas relevant to shock-ignition", *Phys. Plasmas*, vol. 27, no. 8, p. 082 704, 2020. DOI: 10.1063/5.0010920.

[67] S. A. Shekhanov and V. T. Tikhonchuk, "SRS-SBS competition and nonlinear laser energy absorption in a high temperature plasma", *Plasma Phys. Control. Fusion*, vol. 63, p. 115 016, 2021. DOI: 10.1088/1361-6587/ac2614.

[68] M. D. Tracy, E. A. Williams, K. E. Estabrook, J. S. D. Groot, and S. M. Cameron, "Eigenvalue solution for ion-collisional effect in ion acoustic and entropy waves", *Phys. Fluids B*, vol. 5, p. 1430, 1993.

[69] V. Bychenkov, J. Myatt, W. Rozmus, and V. Tikhonchuk, "Quasihydrodynamic description of ion acoustic waves in a collisional plasma", *Phys. Plasmas*, vol. 1, p. 2419, 1994. DOI: 10.1063/1.870570.

[70] J. Breil, S. Galera, and P.-H. Maire, "Multi-material ALE computation in inertial confinement fusion code CHIC", *Computers & Fluids*, vol. 46, p. 161, 2011. DOI: 10.1016/j.compfluid.2010.06.017.

[71] D. E. Hinkel, D. A. Callahan, A. B. Langdon, S. H. Langer, C. H. Still, and E. A. Williams, "Analyses of laser-plasma interactions in National Ignition Facility ignition targets", *Phys. Plasmas*, vol. 15, p. 056 314, 2008. DOI: 10.1063/1.2901127.

[72] A. Smekal, "Zur quantentheorie der dispersion", *Naturwissenschaften*, vol. 11, no. 43, pp. 873–875, 1923. DOI: 10.1007/BF01576902.

[73] C. V. Raman, "A new radiation", *Indian J. Phys.*, vol. 2, p. 387, 1928.

[74] G Landsberg and L. Mandelstam, "Eine neue erscheinung bei der licht- zerstreuung in krystallen", *Naturwissenschaften*, vol. 16, p. 557, 1928.

[75] R. W. Hellwarth, "Theory of stimulated Raman scattering", *Phys. Rev.*, vol. 130, pp. 1850–1852, 1963. DOI: 10.1103/PhysRev.130.1850.

[76] L. Landau, "On the vibrations of the electronic plasma", *J. Phys.*, vol. 10, pp. 25–34, 1946.

[77] G. G. Comisar, "Theory of the stimulated Raman effect in plasmas", *Phys. Rev.*, vol. 141, pp. 200–203, 1966. DOI: 10.1103/PhysRev.141.200.

[78] M. V. Goldman and D. F. DuBois, "Stimulated incoherent scattering of light from plasmas", *Phys. Fluids*, vol. 8, pp. 1404–1405, 1965. DOI: 10.1063/1.1761424.

[79] N. Bloembergen and Y. R. Shen, "Optical nonlinearities of a plasma", *Phys. Rev.*, vol. 141, pp. 298–305, 1966. DOI: 10.1103/PhysRev.141.298.

[80] S. P. Obenschain, N. C. Luhmann, and P. T. Greiling, "Effects of finite-bandwidth driver pumps on the parametric-decay instability", *Phys. Rev. Lett.*, vol. 36, pp. 1309–1312, 22 May 1976. DOI: 10.1103/PhysRevLett.36.1309.

[81] P. N. Guzdar, C. S. Liu, and R. H. Lehmberg, "The effect of bandwidth on the convective Raman instability in inhomogeneous plasmas", *Phys. Fluids B*, vol. 3, pp. 2882–2888, 1991. DOI: 10.1063/1.859921.

[82] E. S. Dodd and D. Umstadter, "Coherent control of stimulated Raman scattering using chirped laser pulses", *Phys. Plasmas*, vol. 8, pp. 3531–3534, 2001. DOI: 10.1063/1.1382820.

[83] J. P. Palastro, J. G. Shaw, R. K. Follett, *et al.*, "Resonance absorption of a broad-band laser pulse", *Phys. Plasmas*, vol. 25, no. 12, p. 123 104, 2018. DOI: 10.1063/1.5063589.

[84] R. D. Milroy, C. E. Capjack, and C. R. James, "Plasma laser pulse amplifier using induced Raman or Brillouin processes", *The Physics of Fluids*, vol. 22, no. 10, pp. 1922–1931, 1979. DOI: 10.1063/1.862481.

[85] A. A. Andreev, C. Riconda, V. T. Tikhonchuk, and S. Weber, "Short light pulse amplification and compression by stimulated Brillouin scattering in plasmas in the strong coupling regime", *Phys. Plasmas*, vol. 13, p. 053 110, 2006. DOI: 10.1063/1.2201896.

[86] S. Weber, C. Riconda, L. Lancia, J.-R. Marquès, G. A. Mourou, and J. Fuchs, "Amplification of ultrashort laser pulses by Brillouin backscattering in plasmas", *Phys. Rev. Lett.*, vol. 111, p. 055 004, 5 2013. DOI: 10.1103/PhysRevLett.111.055004.

[87] B. B. Afeyan and E. A. Williams, "Stimulated Raman sidescattering with the effects of oblique incidence", *Phys. Fluids*, vol. 28, p. 3397, 1985. DOI: 10.1063/1.865340.

[88] O. Klimo, S. Weber, V. T. Tikhonchuk, and J. Limpouch, "Particle-in-cell simulations of laser–plasma interaction for the shock ignition scenario", *Plasma Phys. Control. Fusion*, vol. 52, p. 055 013, 2010. DOI: 10.1088/0741-3335/52/5/055013.

[89] J. Xiang, Z. Liu, and C. Zheng, "Effects of electron-ion collisions on stimulated Raman backward scattering under different electron densities", *Plasma Sci. Technology*, vol. 13, p. 40, 2011. DOI: 10.1088/1009-0630/13/1/09.

[90] W. Rozmus and V. T. Tikhonchuk, "Skin effect and interaction of short laser pulses with dense plasmas", *Phys. Rev. A*, vol. 42, p. 7401, 1990.

[91] T.-Y. B. Yang, W. L. Kruer, R. M. More, and A. B. Langdon, "Absorption of laser light in overdence plasmas by sheath inverse bremsstrahlung", *Phys. Plasmas*, vol. 2, p. 3146, 1995.

[92] G. B. Whitham, *Linear and Nonlinear Waves*. New York: Wiley, 1974.

[93] M. V. Goldman, "Parametric plasmon-photon interactions: Part II. Analysis of plasmon propagator and correlation functions", *Ann. Phys.*, vol. 38, pp. 117–169, 1966. DOI: 10.1016/0003-4916(66)90253-3.

[94] E. A. Jackson, "Parametric effects of radiation on a plasma", *Phys. Rev.*, vol. 153, pp. 235–244, 1967. DOI: 10.1103/PhysRev.153.235.

[95] A. A. Galeev, V. N. Oraevskii, and R. Z. Sagdeev, "Anomalous absorption of electromagnetic radiation at double the plasma frequency", *JETP Lett.*, vol. 16, p. 136, 1972.

[96] M. N. Rosenbluth, "Parametric instabilities in inhomogeneous media", *Phys. Rev. Lett.*, vol. 29, pp. 565–567, 1972. DOI: 10.1103/PhysRevLett.29.565.

[97] S. P. Regan, N. B. Meezan, L. J. Suter, *et al.*, "Suprathermal electrons generated by the two-plasmon-decay instability in gas-filled hohlraums", *Phys. Plasmas*, vol. 17, p. 020 703, 2010. DOI: 10.1063/1.3309481.

[98] C. S. Liu and M. N. Rosenbluth, "Parametric decay of electromagnetic waves into two plasmons and its consequences", *Phys. Fluids*, vol. 19, no. 7, pp. 967–971, 1976. DOI: 10.1063/1.861591.

[99] S. Weber, C. Riconda, O. Klimo, A. Héron, and V. T. Tikhonchuk, "Fast saturation of the two-plasmon-decay instability for shock-ignition conditions", *Phys. Rev. E*, vol. 85, p. 016 403, 2012. DOI: 10.1103/PhysRevE.85.016403.

[100] N. A. Ebrahim, H. A. Baldis, C. Joshi, and R. Benesch, "Hot electron generation by the two-plasmon decay instability in the laser-plasma interaction at 10.6 $\mu$m", *Phys. Rev. Lett.*, vol. 45, pp. 1179–1182, 1980. DOI: 10.1103/PhysRevLett.45.1179.

[101] R. L. Keck, L. M. Goldman, M. C. Richardson, W. Seka, and K. Tanaka, "Observations of high-energy electron distributions in laser plasmas", *Phys. Fluids*, vol. 27, pp. 2762–2766, 1984. DOI: 10.1063/1.864581.

[102] W. C. Mead, E. M. Campbell, W. L. Kruer, *et al.*, "Characteristics of lateral and axial transport in laser irradiations of layered-disk targets at 1.06 and 0.35 $\mu$m wavelengths", *Phys. Fluids*, vol. 27, pp. 1301–1326, 1984. DOI: 10.1063/1.864746.

[103] J. A. Delettrez, T. J. B. Collins, and C. Ye, "Determining acceptable limits of fast-electron preheat in direct-drive-ignition–scale target designs", *Phys. Plasmas*, vol. 26, p. 062 705, 2019. DOI: 10.1063/1.5089890.

[104] B. Yaakobi, A. A. Solodov, J. F. Myatt, J. A. Delettrez, C. Stoeckl, and D. H. Froula, "Measurements of the divergence of fast electrons in laser-irradiated spherical targets", *Phys. Plasmas*, vol. 20, p. 092 706, 2013. DOI: 10.1063/1.4824008.

[105] O. Klimo, J. Pšikal, V. T. Tikhonchuk, and S. Weber, "Two-dimensional simulations of laser–plasma interaction and hot electron generation in the context of shock-ignition research", *Plasma Phys. Control. Fusion*, vol. 52, p. 055 010, 2014. DOI: 10.1088/0741-3335/56/5/055010.

[106] E. Llor Aisa, X. Ribeyre, G. Duchateau, *et al.*, "The role of hot electrons in the dynamics of a laser-driven strong converging shock", *Phys. Plasmas*, vol. 24, p. 112 711, 2017. DOI: 10.1063/1.5003814.

[107] J. Dawson, "On Landau damping", *Phys. Fluids*, vol. 4, pp. 869–874, 1961. DOI: 10.1063/1.1706419.

[108] D. J. Strozzi, E. A. Williams, H. A. Rose, D. E. Hinkel, A. B. Langdon, and J. W. Banks, "Threshold for electron trapping nonlinearity in Langmuir waves", *Phys. Plasmas*, vol. 19, no. 11, p. 112 306, 2012. DOI: 10.1063/1.4767644.

[109] D. Benisti, "Envelope equation for the linear and nonlinear propagation of an electron plasma wave, including the effects of Landau damping, trapping, plasma inhomogeneity, and the change in the state of wave", *Phys. Plasmas*, vol. 23, p. 102 105, 2016. DOI: 10.1063/1.4963854.

[110] J. M. Dawson, "Nonlinear electron oscillations in a cold plasma", *Phys. Rev.*, vol. 113, pp. 383–387, 1959. DOI: 10.1103/PhysRev.113.383.

[111] T. P. Coffey, "Breaking of large amplitude plasma oscillations", *Phys. Fluids*, vol. 14, pp. 1402–1406, 1971. DOI: 10.1063/1.1693620.

[112] C. B. Schroeder, E. Esarey, and B. A. Shadwick, "Warm wave breaking of nonlinear plasma waves with arbitrary phase velocities", *Phys. Rev. E*, vol. 72, p. 055 401, 2005. DOI: 10.1103/PhysRevE.72.055401.

[113] O. Klimo and V. T. Tikhonchuk, "Laser-plasma interaction studies in the context of shock ignition: The regime dominated by parametric instabilities", *Plasma Phys. Control. Fusion*, vol. 55, p. 095 002, 2013. DOI: 10.1088/0741-3335/55/9/095002.

[114] F. Harlow, "A machine calculation for hydrodynamic problems", Los Alamos Scientific Laboratory, Tech. Rep. LAMS-1956, 1956.

[115] C. Birsall and A. Langdon, *Plasma Physics Via Computer Simulation*. New York: McGraw-Hill, 1985.

[116] J. Derouillat, A. Beck, F. Pérez, *et al.*, "SMILEI: A collaborative, open-source, multi-purpose particle-in-cell code for plasma simulation", *Computer Phys. Comm.*, vol. 222, p. 351, 2018. DOI: 10.17632/gsn4x6mbrg.1.

[117] K. Nanbu, "Theory of cumulative small-angle collisions in plasmas", *Phys. Rev. E*, vol. 55, 1997. DOI: 10.1103/PhysRevE.55.4642.

[118] F. Pérez, L. Gremillet, A. Decoster, M. Drouin, and E. Lefebvre, "Improved modeling of relativistic collisions and collisional ionization in particle-in-cell codes", *Phys. Plasmas*, vol. 19, no. 8, p. 083 104, 2012. DOI: 10.1063/1.4742167.

[119] R. Liska, M. Kuchařik, J. Limpouch, *et al.*, "ALE method for simulations of laser-produced plasmas", *Finite Volumes for Complex Applications VI – Problems & Perspectives*, vol. 4, p. 857, 2011.

[120] B. Fryxell, K. Olson, P. Ricker, *et al.*, "FLASH: An adaptive mesh hydrodynamics code for modeling astrophysical thermonuclear flashes", *Astrophys. J. Suppl. Ser.*, vol. 131, p. 273, 2000. DOI: 10.1086/317361.

[121] P. Tzeferacos, M. Fatenejad, N. Flocke, *et al.*, "FLASH magnetohydrodynamic simulations of shock-generated magnetic field experiments", *High Energy Density Phys.*, vol. 8, p. 322, 2012. DOI: 10.1016/j.hedp.2012.08.001.

[122] L. Hudec, A. Gintrand, J. Limpouch, *et al.*, "A hybrid ablation-expansion model for low-density foams: Numerical aspects", *Phys. Plasmas*, vol. 30, 2023.

[123] J. C. Fernández, J. A. Cobble, B. H. Failor, *et al.*, "Observed dependence of stimulated Raman scattering on ion-acoustic damping in hohlraum plasmas", *Phys. Rev. Lett.*, vol. 77, p. 2702, 1996.

[124] R. K. Kirkwood, B. J. MacGowan, D. S. Montgomery, *et al.*, "Effect of ion-wave damping on stimulated Raman scattering in high-Z laser-produced plasmas", *Phys. Rev. Lett.*, vol. 77, p. 2706, 1996.

[125] H. F. Robey, L. B. Hopkins, J. L. Milovich, and N. B. Meezan, "The I-Raum: A new shaped hohlraum for improved inner beam propagation in indirectly-driven ICF implosions on the National Ignition Facility", *Phys. Plasmas*, vol. 25, p. 012 711, 2018. DOI: 10.1063/1.5010922.

[126] M. Olazabal-Loumé, P. Nicolaï, G. Riazuelo, *et al.*, "Simulations on laser imprint reduction using underdense foams and its consequences on the hydrodynamic instability growth", *New J. Phys.*, vol. 15, p. 085 033, 2013.

[127] F. Pérez, J. D. Colvin, M. J. May, *et al.*, "High-power laser interaction with low-density C–Cu foams", *Phys. Plasmas*, vol. 22, p. 113 112, 2015. DOI: 10.1063/1.4935911.

[128] O. N. Rosmej, N. E. Andreev, S. Zaehter, *et al.*, "Interaction of relativistically intense laser pulses with long-scale near critical plasmas for optimization of laser based sources of MeV electrons and gamma-rays", *New J. Phys.*, vol. 21, p. 043 044, 2019. DOI: 10.1088/1367-2630/ab1047.

[129] R. J. Mason, R. A. Kopp, H. X. Vu, *et al.*, "Computational study of laser imprint mitigation in foam-buffered inertial confinement fusion targets", *Phys. Plasmas*, vol. 5, pp. 211–221, 1998. DOI: 10.1063/1.872690.

[130] T. Kapin, M. Kucharik, J. Limpouch, and R. Liska, "Hydrodynamic simulations of laser interactions with low-density foams", *Czech. J. Phys.*, vol. 56, B4593, 2006.

[131] S. Y. Gus'kov, M. Cipriani, R. De Angelis, *et al.*, "Absorption coefficient for nanosecond laser pulse in porous material", *Plasma Phys. Control. Fusion*, vol. 57, p. 125 004, 2015.

[132] J. Velechovsky, J. Limpouch, R. Liska, and V. T. Tikhonchuk, "Hydrodynamic modeling of laser interaction with micro-structured targets", *Plasma Phys. Control. Fusion*, vol. 58, p. 095 004, 2016. DOI: 10.1088/0741-3335/58/9/095004.

[133] M. A. Belyaev, R. L. Berger, O. S. Jones, *et al.*, "Laser propagation in a subcritical foam: Subgrid model", *Phys. Plasmas*, vol. 27, p. 112 710, 2020. DOI: 10.1063/5.0022952.

[134] N. G. Borisenko, I. V. Akimova, A. I. Gromov, *et al.*, "Regular 3-D networks with clusters for controlled eneergy transport studies in laser plasma near critical density", *Fusion Sci. Technology*, vol. 49, p. 676, 2006.

[135] A. M. Khalenkov, N. G. Borisenko, V. N. Kondrashov, Y. A. Merkuliev, J. Limpouch, and V. G. Pimenov, "Experience of micro-heterogeneous target fabrication to study energy transport in plasma near critical density", *Laser Part. Beams*, vol. 24, p. 283, 2006. DOI: 10.1017/S0263034606060435.

[136] G. Duchateau, S. X. Hu, A. Pineau, *et al.*, "Modeling the solid-to-plasma transition for laser imprinting in direct-drive inertial confinement fusion", *Phys. Rev. E*, vol. 100, p. 033 201, 2019. DOI: 10.1103/PhysRevE.100.033201.

[137] H. C. van der Hulst, *Light scattering by small particles*. Dover Publ., 1957.

[138] I. Gurwich, N. Shiloah, and K. Kleiman, "The recursive algorithm for electromagnetic scattering by tilted infinite circular multilayered cylinder", *J. Quant. Spect. Rad. Transfer*, vol. 63, p. 217, 1999.

[139] Wolfram Mathematica. [Online]. Available: https://www.wolfram.com/mathematica.

[140] J. Limpouch, O. Renner, N. Borisenko, *et al.*, "Applications of low-density foams for X-ray source studies and laser beam smoothing", *J. Phys.: Conf. Ser.*, vol. 112, p. 042 056, 2008. DOI: 10.1088/1742-6596/112/4/042056.

[141] R. Fabbro, C. Max, and E. Fabre, "Planar laser-driven ablation: Effect of inhibited electron thermal conduction", *Phys. Fluids*, vol. 28, p. 1463, 1985. DOI: 10.1063/1.864982.

[142] E. G. Gamaly, A. V. Rode, B. Luther-Davies, and V. T. Tikhonchuk, "Ablation of solids by femtosecond lasers: Ablation mechanism and ablation thresholds for metals and dielectrics", *Phys. Plasmas*, vol. 9, p. 949, 2002. DOI: 10.1063/1.1447555.

[143] S. C. Wilks, W. L. Kruer, M. Tabak, and A. B. Langdon, "Absorption of ultra-intense laser pulses", *Phys. Rev. Lett.*, vol. 69, p. 1383, 1992. DOI: 10.1103/PhysRevLett.69.1383.

[144] P. Mora, "Plasma expansion into a vacuum", *Phys. Rev. Lett.*, vol. 90, p. 185 002, 2003. DOI: 10.1103/PhysRevLett.90.185002.

[145] O. S. Jones, G. E. Kemp, S. H. Langer, *et al.*, "Experimental and calculational investigation of laser-heated additive manufactured foams", *Phys. Plasmas*, vol. 28, p. 022 709, 2021. DOI: 10.1063/5.0032023.